Preparation of Nanoparticle/Gelatin Composite Porous Materials for Photothermal Cancer Therapy

Preparation of Nanoparticle/Gelatin Composite Porous Materials for Photothermal Cancer Therapy

Jing Zhang

Doctoral Program in Materials Science and Engineering

Submitted to the Graduate School of
Pure and Applied Sciences
in Partial Fulfillment of the Requirements
for the Degree of Doctor of Philosophy in
Engineering

at the
University of Tsukuba

Content

List of abbreviations

WHO	World Health Organization
DNA	Deoxyribonucleic acid
PDT	Photodynamic therapy
HIFU	High intensity focused ultrasound
RFA	Radiofrequency ablation
PTT	Photothermal therapy
NIR	Near infrared
MRI	Magnetic resonance imaging
LSPR	Localized surface plasmon resonance
CT	Computed tomography
CTAB	Cetyltrimethylammonium bromide
CNT	Carbon nanotube
SWNT	Single-walled carbon nanotube
MWNT	Multi-walled carbon nanotube
FDA	US Food and Drug Administration
TAM	Tumor associated macrophage
PGA	Poly(glycolic acid)
PLA	Poly(lactic acid)
PLGA	Poly(lactic-co-glycolic acid)
RGD	Arginylglycylaspartic acid
HA	Hydroxyapatite
β-TCP	Beta-tricalcium phosphate
3D	Three-dimensional
Gel	Gelatin
FA	Folic acid
EMEM	Eagle’s Minimun Essential Medium
MES	2-(Nmorpholino) ethanesulfonic acid
EDC	1-ethyl-3-(3-dimethylaminopropyl) carbodiimide
NHS	N-hydroxysuccinimide
FBS	Fetal bovine serum
SEM	Scanning electron microscope
TEM	Transmission electron microscopy
DLS	Dynamic light scattering
XRD	X-ray powder diffraction
UV	Ultraviolet
TGA	Thermogravimetric analysis
HeLa	Human cervical carcinoma cell
PLL	Poly-L-lysine
DMSO	Dimethyl sulfoxide
PBS	Phosphate buffer saline

AuNP	Gold nanoparticle
AuNR	Gold nanorod
AuNS	Gold nanostar
AA	Ascorbic acid
SD	Standard deviation

Chapter 1

General introduction

1.1 Cancer therapy

Cancer is a group of diseases involving abnormal cell growth with the potential to invade or spread to other parts of the human body. It contains benign tumor and malignant tumor.[1] Not all tumors could threat human life. Benign tumors have a slower growth rate than malignant tumors and the cells usually have normal features. Benign tumors are typically surrounded by a fibrous sheath or remain with the epithelium.[2] Although this kind of tumor lacks of the ability to invade or spread to neighboring tissue, but it still may cause some negative effects on human health and many types of benign tumors have the potential to become cancerous (malignant) through a process known as tumor progression.[3] Malignant tumor has become one of the biggest threats to human life. According to the "World Cancer Report 2014" of World Health Organization (WHO), in 2012, there are about 14.1 million new cancer cases and 8.2 million cancer related deaths all over the world. And it is expected that the number of new cases will rise from 14 million in 2012 to 22 million within the next two decades. Therefore, the huge amount of new cases and high mortality rate of malignant tumor make it essential and urgent to explore effective ways for cancer therapy application.

1.1.1 Current therapies for cancer treatment and their limitations

Over the past few decades, some methods have been developed for cancer treatment. Surgical resection is one of the mainly used methods in the clinical field. Tumor site could be totally removed by clinical surgery to prolong the patient lifetime. However, this method is only effective to the early-stage or middle-stage tumor, which cancer cells have not metastasized to other organs. On the other hand, the blurry boundary between tumor and normal tissue makes it difficult to remove the whole tumor tissue precisely. Because of the malignant and aggressive nature of tumor, the remained tumor cells or tumor tissue will cause the cancer recurrence.[4, 5]

From 1950s, chemotherapy has been widely used as a novel way for cancer treatment. Chemotherapy is a strategy that using one or more kinds of anti-cancer drugs to stop or slow the growth of cancer cells. Up to now, there are many different types of anti-cancer drugs have been explored including alkylating agents (mechlorethamine, carmustine dacarbazine and so on),[6] antimetabolites (cytarabine, gemcitabine, decitabine and so on),[7] anti-microtubule agents (vinca alkaloids, taxanes and podophyllotoxin),[8, 9] topoisomerase

inhibitors (etoposide, mitoxantrone, novobiocin, merbarone and so on) and cytotoxic antibiotics (doxorubicin, daunorobicin, dactinomycin and so on).[10] However, all of these anti-cancer drugs lack of specificity to cancer cells. After injection these drugs, both tumor cells and normal cells are killed by the drugs, which could cause many side effects such as hair loss, immunosuppression, myelosuppression, organ damage and so on. What's more, after multiple chemotherapies, the cancer cells will be resistant to anti-cancer drugs, which could lead to the failure of the treatment.[7]

Radiotherapy is utilizing ionizing radiation to damage the DNA of cells to control or kill malignant tissue. Radiotherapy contains three main divisions: external beam radiation therapy, brachytherapy and systemic radioisotope therapy. However, like the chemotherapy, the main limitation of radiotherapy is lack of the specificity to tumor tissue. The normal tissue is also damaged during radiation, which also causes severe side effects.[11]

In brief, surgical ablation, chemotherapy and radiotherapy are the most commonly used methods in the clinical field for cancer therapy application. Although they could kill the cancer cells and prolong the patient lifetime efficiently, these three methods still have many limitations such as cancer recurrence and severe side effects. Therefore, novel methods with high killing efficiency and specificity are highly needed.

1.1.2 New strategies for cancer therapy application

As mentioned, because of the limitations of current therapies, many researchers try to explore more effective strategies and drugs to treat malignant tumor. Up to now, some approaches have been developed.

1.1.2.1 Cancer immunotherapy

Cancer immunotherapy was firstly introduced by Steven Rosenberg and colleagues in the late 1980s. They reported patients with metastatic cancer possessed a low tumor regression rate (2.6–3.3%) after underwent active specific immunotherapy. Since then, cancer immunotherapy has drawn world-wide concern. Cancer immunotherapy is the use of the immune system to treat cancer (Fig. 1.1a). This approach utilized the fact that cancer cells often have some specific molecules on their surface, which could be detected by the immune system, known as tumor-associated antigens. Tumor-associated antigens are usually proteins or other macromolecules (e.g. carbohydrates).[12] Cancer immunotherapy can be simply divided into active, passive or hybrid (active and passive) immunotherapy. Active immunotherapy is that the immune system directly attacked tumor cells by targeting tumor-associated antigens. Dendritic cell therapy is one kind of active immunotherapy. The process of provoking anti-tumor responses is that the dendritic cells present tumor-associated antigens to lymphocytes, which could activate lymphocytes and then the activated lymphocytes kill the other cancer cells that possessed the same kind of antigen.[13] Passive immunotherapy enhances existing anti-tumor responses and includes the use of monoclonal antibodies, lymphocytes and cytokines. Antibody therapy and cytokines therapy are two kinds of passive immunotherapy. Antibody therapy is that monoclonal antibodies bind to target cell surfaces and form a binding region and this binding region can be recognized by immune system. The natural killer cells existing in the immune system could release some cytotoxic protein or serine protease to kill the cancer cells.[14] Cytokines are proteins produced by many types of cells including tumor cells. The tumor often employs cytokines to allow it to grow and reduce the immune response. These immune-modulating effects let them have the potential to be used as drugs to raise an immune response. Interferons and interleukins are the two commonly used cytokines for cytokine therapy application. Nowadays, because of its low cytotoxicity, low rejection reaction and high specificity, more and more researchers focus on using immunotherapy for cancer therapy application.[15]

1.1.2.2 Gene therapy

Gene therapy is the delivery of a specific gene as a therapeutic drug into targeted cells to treat diseases. There are several approaches of gene therapy (Fig. 1.1b). First, the copy of the health gene could replace the mutated gene, which causes disease. Second, the delivered gene inactivates the mutated gene and mutated gene could not function properly. Third, a new gene is introduced into the human body and aid to fight with the disease.[16] Actually, a gene which is directly inserted into the targeted cells could not work very well. Therefore, a suitable carrier called a vector is genetically engineered to deliver the gene. The vectors could be divided into viruses and non-viral vectors (cationic polymer, liposome, polypeptide and nanoparticle). Virus vectors usually have better gene transfection effect than non-viral vectors, but their strong immunogenicity often lead the body to produce a serious rejection reaction, which resulted in the failure of treatment.[17] Although the non-viral vectors do not cause strong immune rejection, low gene transfection efficiency, strong cytotoxicity, and poor specific targeting capacity of non-viral vectors cannot meet the requirements of gene delivery in the clinical field.[18]

1.1.2.3 Photodynamic therapy

Photodynamic therapy (PDT) is a kind of phototherapy involving a particular type of light and a photosensitizing agent. When the photosensitizing agents are exposed to a specific wavelength of light, they produce the molecular oxygen to destroy the cell membrane and kill nearby cells (Fig. 1.1c).[19] PDT has been proven ability to kill microbial cells and some efficacy in anti-viral treatments.[20] Clinically, PDT is widely used in treating severe acne[21] and has been applied to treat a wide range of medical conditions, including atherosclerosis and psoriasis.[22] Now many researchers explore the PDT to treat malignant tumors such as head, neck, lung, bladder and particular skin tumor.[19] The advantage of PDT is lessening the need for delicate surgery, minimally invasive and minimally toxic to the human body. However, the activation wavelength of many kinds of photosensitizing agents is located in the ultraviolet or visible region and the penetration depth of ultraviolet or visible light is very limited, usually no more than one centimeter. For this reason, PDT is usually used to treat the tumor with small volume, skin tumor or tumor just under the skin. Because the light cannot pass through deeply in the tumor, PDT is less effective in treating large tumors and it is also a local treatment and cannot be used to treat metastasized cancer. In addition, during light irradiation, PDT can also cause some side effects to nearby healthy tissue such as burns, swelling, pain, and scar in the normal tissue.[23] Therefore, it is highly needed to develop some new photosensitizing agents that are more powerful, more specific to targeted cells and long-wavelength excitation that can penetrate and treat deep or large tumors.

1.1.2.4 Hyperthermia therapy

Based on the fact that cancer cells are more sensitive to high temperatures than normal cells, hyperthermia therapy has been developed as a new approach to induce cancer cell apoptosis or directly kill cancer cells by increasing the temperature of the body, particularly temperature in tumor site (Fig. 1.1d). Many researchers have shown that an appropriate temperature (41 ~ 47 ^{o}C) can damage and kill cancer cells and has minimal injury to normal cells and normal tissues. The tumor volume could be decreased by hyperthermia treatment because the high temperature could kill cancer cells and damage proteins and structures within cancer cells. Depending on the treated area, the hyperthermia therapy can be defined as local hyperthermia, regional hyperthermia and whole-body hyperthermia.[24] Due to the difficulties of precise control the temperature in the tumor site, tumor hyperthermia did not have a good therapeutic efficacy, previously. In recent years, with the development of various technologies, a variety of new heating methods have been developed. It has progressively realized the exact controlling the temperature in tumor site and the malignant tumor can be treated efficiently. At present, the commonly studied hyperthermia methods include high intensity focused ultrasound (HIFU),[25, 26] radiofrequency ablation (RFA),[27, 28] magnetic therapy,[29, 30]

photothermal therapy (PTT)[31, 32] and so on.

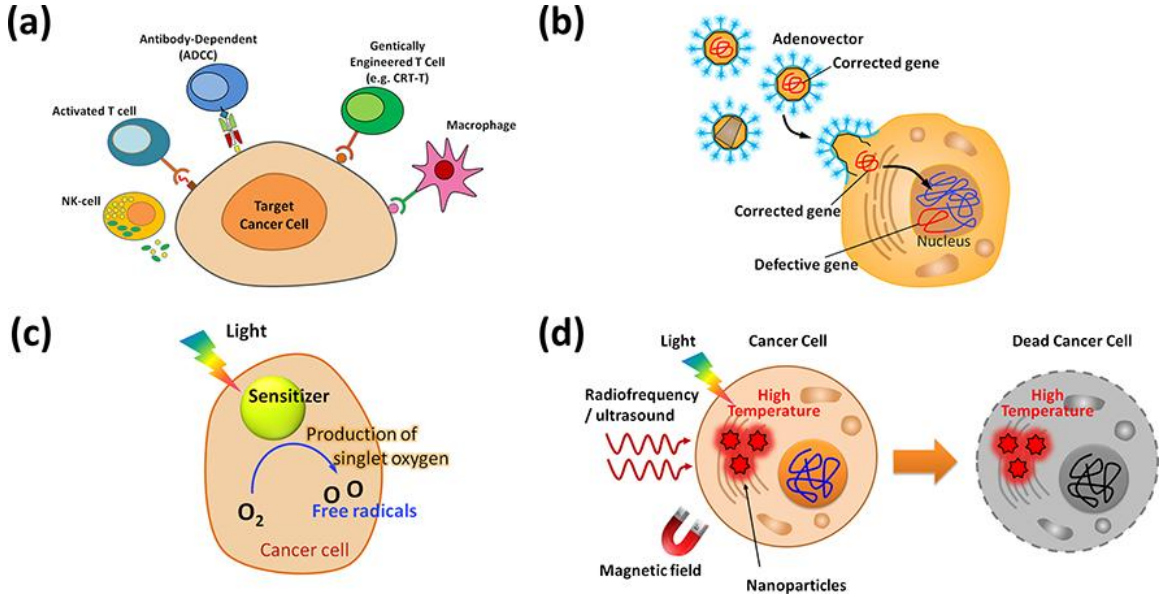

Fig. 1.1. New strategies for cancer therapy (a) cancer immunotherapy, (b) gene therapy, (c) photodynamic therapy and (d) hyperthermia therapy.

1.2 Photothermal therapy (PTT)

Due to the lack of specificity to the killing of cancer cells and serious side effects on normal cells and normal tissues, traditional cancer treatment methods cannot achieve satisfactory cancer treatment effect. With the increase of the number of cancer new cases each year, the development of new high-performance and low toxicity of cancer treatment methods is highly needed. In recent years, photothermal therapy (PTT) has received extensive attention, because of its excellent therapeutic effect. Photothermal therapy is defined as using the photothermal conversion agents to absorb near infrared (NIR) region light and convert it to heat, thereby leading to the destruction of cancer cells (Fig. 1.2). The accumulation of photothermal conversion agents in the tumor site and selective laser irradiation of tumor tissue, photothermal therapy can effectively kill the cancer cells and reduce negative effect on normal tissue.[32, 33] Therefore, it can be seen that a suitable photothermal conversion agent is one of the key factors of PTT. An ideal photothermal conversion agent should high photothermal conversion efficiency, good tumor-enriching ability and good biocompatibility. Up to now, many kinds of nanomaterials have been investigated as photothermal conversion agents.

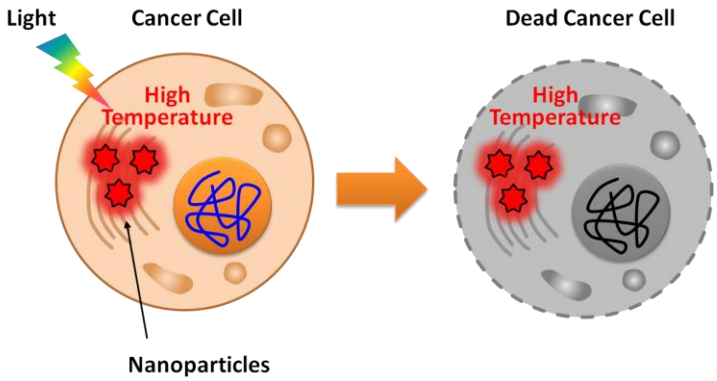

Fig. 1.2. Illustration of photothermal therapy (PTT).

1.2.1 Photothermal conversion agent

Photothermal conversion agent is one of the key factors of PTT. Because of the enhanced permeability and retention effect, nano-scaled materials (especially 20 ~ 300 nm) have aroused much attention as photothermal conversion agents for PTT (Fig. 1.3).[34]

1.2.1.1 Iron oxide nanoparticle

Iron oxide particles with diameters in the range of 1 and 100 nm are called iron oxide nanoparticles. There are two main forms of iron oxide nanoparticles, magnetite (Fe_3O_4) and its oxidized form maghemite (γ-Fe_2O_3).[35] Among these two kinds of iron oxide nanoparticles, Fe_3O_4 nanoparticle has attracted much attention. Due to its superparamagnetic property, easy biodegradation, non-cytotoxicity and good biocompatibility, Fe_3O_4 nanoparticle has been extensively studied in the biomedical field and it has many biomedical applications.[36-38] First, the Fe_3O_4 nanoparticle can be used in medical diagnosis. Fe_3O_4 nanoparticle is a good contrast enhancement agent, which can be used for magnetic resonance imaging (MRI) to obtain high-quality anatomical images for diagnosis.[39-41] Fe_3O_4 nanoparticle can be also used to deliver therapeutic agents to the targeted cells. Because of the high magnetic susceptibility of Fe_3O_4 nanoparticles, the targeting effect of Fe_3O_4 nanoparticle could be improved not only by surface modification but also by external magnetic field that could non-invasive manipulate Fe_3O_4 nanoparticles in living body.[42-44] Moreover, the Fe_3O_4 nanoparticles can be also used for magnetic hyperthermia.[30, 45-47] When the injected Fe_3O_4 nanoparticles exposed to the magnetic field, the local temperature could be raised up quickly to kill the cancer cells. Furthermore, using Fe_3O_4 nanoparticles as photothermal conversion agents for PTT is another important biomedical application. Fe_3O_4 nanoparticles have strong NIR absorption and high photothermal conversion efficiency and the local temperature could be elevated quickly during NIR laser irradiation. Therefore, Fe_3O_4 nanoparticle is also a promising candidate for PTT application.[48-52] Coprecipitation,[53-55] microemulsions[56-58] and high-temperature decomposition of organic precursors[59, 60] are three main methods for preparation of Fe_3O_4 nanoparticles. The reaction of coprecipitation method is carried out in an aqueous solution and this reaction can be easily operated and have short reaction time. The disadvantage of the Fe_3O_4 nanoparticles prepared by the coprecipitation method is that the nanoparticles usually have a wide size distribution and the Fe_3O_4 nanoparticles easily aggregated with each other. The Fe_3O_4 nanoparticles prepared by microemulsions and high-temperature decomposition of organic precursors have a narrow size distribution and regular spherical shape. But both microemulsions and high-temperature decomposition of organic precursors method involve organic solvent in the reaction.

1.2.1.2 Gold-based nanoparticles

Gold-based nanoparticles have become one of the most promising candidates used for PTT. The advantages of gold-based nanoparticles are their facile preparation, easy modification, and good photothermal conversion properties. Moreover, the localized surface plasmon resonance (LSPR) peaks of gold nanoparticles is tunable by changing the size and shape gold nanoparticles. In addition, gold-based nanoparticles can be also used for CT imaging and therapeutic agent delivery.[61] However, the photothermal conversion efficiency of gold nanoparticles with spherical shape is not very high, because the localized surface plasmon resonance (LSPR) peaks of spherical gold nanoparticles with different sizes are mainly located in the range of 520 to 580 nm. *In vivo*, the penetration depth of light with these wavelengths is limited. Because skin and tissues have a transmission window from 650 to 900 nm and the transmission peak at approximately 800 nm, which is known as the "near-infrared tissue transparent window".[62, 63]Therefore, due to the limitation of spherical gold nanoparticles in PTT application, gold nanoparticles with different

shape and size have been developed for PTT, such as gold nanorods,[64-66] gold nanostars,[67-69] gold nanoshells,[70-72] gold nanocages[73-75] and hollow gold nanospheres.[76-78]

I. Gold nanorod

Rod-shaped gold nanoparticle has been synthesized as one solution for the disparity between the wavelengths required to excite spherical gold nanoparticles and the in vivo transmission window. Gold nanorod has two LSPR peaks: stronger one in the long-wavelength region caused by its longitudinal direction of gold nanorod and the other one in the visible region caused by the transverse direction of gold nanorod. By altering their aspect ratio, the stronger LSPR peaks of gold nanorods can be tuned from 550 nm up to 1 μm, which could meet the requirements of PTT application. God nanorods are usually synthesized by a seed-mediated growth method. A typical preparation process involves two steps. First, the Au seed solution was prepared by a chemical reduction of $HAuCl_4$ with citrate as a stabilizer. And then Au seed solution is added to the bulk $HAuCl_4$ growth solution, which contains $HAuCl_4$, ascorbic acid, cetyltrimethylammonium bromide (CTAB) and silver ions. The stability and biocompatibility of nanoparticles are also very important. Many molecules and polymers have been coated on the surfaces of nanoparticles to increase their stability such as PEG, BSA and so on. Now many researchers investigate using gold nanrod for PTT application and the results showed that the heat generated gold nanorods could kill the cancer cells efficiently during NIR laser irradiation.[64]

II. Gold nanostar

Recently, star-shaped gold nanoparticle used for PTT has been extensively studied. Gold nanostars were also prepared by a seed-mediated growth method. The prepared Au seed solution was dipped into growth solution including $HAuCl_4$, ascorbic acid and silver ions. The sizes of gold nanostars could be varied by usage of different volumes of Au seed solution. Because of their multiple branches with sharp tips, gold nanostars have some unique properties. For example, the LSPR peaks of gold nanostars locate in the NIR region and more importantly, gold nanostars have a wide absorption peak in NIR region, which means gold nanostars could absorb different wavelengths of NIR light and convert it into heat to raise the local temperature.[79] In addition, gold nanostars have a large surface area, which also make them a good candidate for drug delivery.[80]

III Gold nanoshell

Gold nanoshell is one kind of localized surface plasmon resonant (LSPR) nanoparticles, which consists a nanoscaled silica core which is covered by an ultra-thin gold shell. The absorption and scattering properties of gold nanoshells can be changed by altering the ratio of the core diameter and the shell thickness. The LSPR peaks of gold nanoshell could be shifted to the NIR region, if increase the size of silica core and decrease the thickness of the gold shell. It has been reported that after the modification, gold nanoshell has good photothermal efficacy on treatment of head, neck and prostate cancer.[81]

IV Gold nanocage

Gold nanocage is a novel class of gold nanostructures possessing hollow interiors and porous walls and it was reported in 2002 for the first time. The size of gold nanocage can vary from 10 to over 150 nm. The LSPR peak of gold nanocage is in the NIR region, which indicates the potential use as photothermal conversion agent for PTT.[73, 74] Additionally, gold nanocage is also a promising contrast agent for optical imaging.[82, 83]

V. Hollow gold nanosphere

As mentioned above, the spherical gold nanoparticles do not have obvious photothermal effect during NIR laser irradiation, so they cannot be applied in PTT application. Hollow gold nanosphere (HGN) as a novel gold nanostructure has been recently appeared. This new class of gold nanostructure has spherical shape, hollow interior, uniform gold shell, and strong and tunable LSPR peak in the NIR region. The average diameter of HGNs is usually 30 ~ 50 nm. Because of the hollow interior, the thickness of the outer shell is about 3 ~ 6 nm. It has been reported that the hollow gold nanosphere had be successfully used for photothermal ablation of cancer cells both *in vitro* and *in vivo*.[76, 78]

1.2.1.3 Carbon-based nanomaterials

I. Carbon nanotube (CNT)

Carbon nanotube (CNT) is a typical one-dimensional nanomaterial. CNT was discovered by Iijima *et al*. in 1991. CNTs are made of one or more layers of graphite sheet and have a hollow tubular structure. Based on the number of layers, CNTs are normally classified into single-walled carbon nanotube (SWNT) and multi-walled carbon nanotube (MWNT). CNTs have many unique properties such as high electrical conductivity, good mechanical property and high thermal conductivity. More importantly, SWNTs show non-cytotoxicity, good biocompatibility and in the near-infrared region often referred as the "biological window", show low light scattering, strong absorption and autofluorescence. Due to all of these properties, carbon nanotubes have been widely used in many fields, especially the biomedical field. The carbon nanotubes can be used in near-infrared fluorescence imaging[84-86] and photoacoustic imaging.[87-89] After the surface modification, the carbon nanotube is also a good drug carrier to deliver therapeutic drug into target site.[90-92] Moreover, because of its high photothermal conversion efficiency in the NIR region, carbon nanotube could be also used as photothermal conversion agent for PTT application. A variety of researchers has proved that after intravenous injection, modified carbon nanotubes could accumulate in the tumor site and the cancer cells could be efficiently killed during NIR laser irradiation.[93-95]

II. Graphene and graphene oxide

Graphene is discovered by Geim *et al.* in 2004 and this finding was awarded Nobel Prize in 2010. As a new class of carbon-based nanomaterials, graphene possessed unique structures and properties. Graphene is made of a single, tightly packed layer of carbon atoms that bonded together in a hexagonal lattice and graphene is also a typical two-dimensional material. Graphene has many outstanding features comparing with other kinds of materials. Graphene is known as the thinnest, lightest and strongest material up to now. It is flexible and nearly transparent. Graphene also has a large surface area, excellent thermal and electronic conductivity. Based on all of these features, graphene has widely applications such as energy storage and optoelectronics. Moreover, graphene could also be used in biomedical applications. Some recent studies have reported that graphene was used for nerves and cardiac tissue engineering. Moreover, graphene can be used in gene transfection,[96, 97] drug delivery,[98, 99] biosensor,[100, 101] biological imaging[102] and PTT applications.[102, 103]

Graphene oxide is composed of not only carbon atom but also oxygen and hydrogen in variable ratios and it is usually obtained by treating graphite with strong oxidizing agents. Because the existence of carboxyl groups and hydroxyl groups on the surfaces of graphene oxide, it is quite easy to modify their surfaces by covalent or non-covalent bonding. Therefore, graphene oxide also has been widely investigated for biological applications.[104] Graphene oxide is also a promising candidate for PTT application, because it possessed quite high photothermal conversion efficiency in NIR region.[105, 106]

1.2.1.4 Copper-based nanomaterials

Copper-based nanomaterials are another very important class of photothermal conversion agents such as

copper sulfide (Cu_xS_y)[107] nanoparticle and copper selenide ($Cu_{2-x}Se$) nanoparticle.[108] Different from gold-based nanomaterials, the absorption peaks of copper-based nanomaterials are mainly located near 980 nm. Researchers have reported the modified copper sulfide nanoparticles showed no obvious cytotoxicity, high photothermal conversion efficiency and tumor cells could be killed efficiently during laser irradiation.[109, 110]

1.2.1.5 Other photothermal conversion agents

Besides the photothermal conversion agents mentioned above, there are some other kinds of nanomaterials that can be used in PTT application. Transition metal sulfide nanoparticles including molybdenum disulfide (MoS_2) and tungsten disulfide (WS_2) have strong absorption in NIR region. Therefore, after surface modification, transition metal sulfide nanoparticles could be applied in PTT and results have indicated that these nanoparticles have good therapeutic efficacy of photothermal ablation of cancer cells.[111-114]

Organic polymer nanoparticels have been also studied for PTT application. For example, indocyanine green as organic dye molecules light has a strong light absorption capacity in the NIR region, so they can be act as photothermal conversion agents for PTT. Moreover, indocyanine green is a safety contrast imaging agent, which has been approved by the US Food and Drug Administration (FDA). Some studies have proved that indocyanine green is a safe and efficient agent for PTT application.[115, 116] Polypyrrole nanoparticle is another kind of organic polymer nanoparticle. Polypyrrole nanoparticle has strong absorption in NIR region.[117, 118] Some *in vitro* results have shown that polypyrrole stabilized by polyvinyl alcohol could kill almost all of the cancer cells by 808 nm laser irradiation for 5 min.[117]

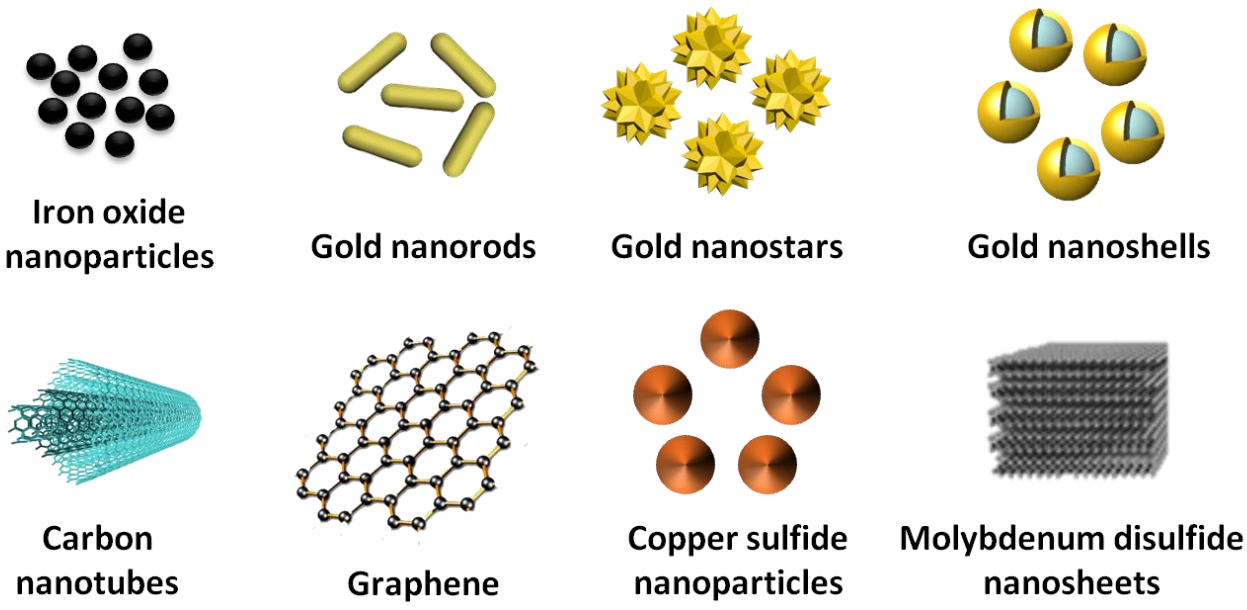

Fig. 1.3. Different kinds of nanomaterials used as photothermal conversion agents.

1.2.2 Limitations of current PTT

PTT has emerged as a novel way to treating malignant tumors. Since many kinds of photothermal conversion agents have been explored, this method has been proved having good therapeutic efficacy by numerous experiments both *in vitro* and *in vivo*, which made PTT become a promising strategy for cancer

therapy application. Up to now, most of studies focus on using different kinds of free nanoparticles as photothermal conversion agents for PTT application. However, there are still some limitations of current PTT, which restrict the application of this method in clinical field. First, the specificity of current strategies for PTT is not so high. It is well known that one of main limitations of traditional methods is lack of specificity. An ideal treatment method should be just specific to tumor site, which indicates that the tumor site could be totally damaged and surrounded or other parts of cells and tissue are not affected by the treatment. Usually, free nanoparticles used as photothermal conversion agents are entered into the body by intravenous injection and reach the tumor site through the blood circulation. But after the injection, most of free nanoparticles are rapidly cleared by mononuclear phagocyte system and the remained nanoparticles preferentially accumulate in some normal tissues such as kidney, lung, liver and spleen rather than the tumor site, which may cause some side effects on the normal tissue. In order to solve this problem, researchers have prepared nanoparticles with targeting ability. The surfaces of nanoparticles are modified with some specific antibodies or targeting ligands to target tumor tissues. For the Fe_3O_4 nanoparticles, they can be also manipulated by external magnetic field to enhance their targeting ability. Although so many strategies have been explored for improving the targeting ability of nanoparticles, the amount of nanoparticles accumulated in tumor sites is still limited. Second, the killing efficiency *in vivo* cannot satisfy the clinical requirements. Because of limited amount of nanoparticles in tumor site, the cancer cells cannot be efficiently killed during NIR laser irradiation. Due to the aggressive and resistant nature of cancer, the remained cancer cells or tumor tissue could cause the tumor recurrence. If the injected amount of nanoparticles increasing, more nanoparticles will accumulate in healthy tissues and it will cause cytotoxicity to the normal cells and tissues.[119] What's more, repeated heating efficiency of free nanoparticles is not so high. In the clinic, because of high growth rate of cancer cells, repeated treatments are very necessary for preventing cancer recurrence. However, traditional nanoparticle-injection-based photothermal technology is hardly to achieve this goal because the small sizes of nanoparticles make them easily leak from tumor sites, which could affect their killing efficiency of cancer cells. It might be need more than one time injection to obtain good therapeutic efficacy and multiple injections not only make patients painful but also have negative effect on patients' health.[120] Therefore, the free nanoparticles need some carriers to deliver photothermal conversion agents, improve their specificity to tumor site and repeat heating efficiency.

1.2.3 Carriers for photothermal conversion agent

Due to poor specificity, limited killing efficiency and low repeat heating efficiency of current photothermal conversion agents, an appropriate carrier need to be explored to deliver photothermal conversion agents to tumor site. Some researchers have paid attention to this field. There are two mainly kinds of carriers of photothermal conversion agents: cell carriers and scaffold carriers.

1.2.3.1 Cell carrier

After entered into circulation system, most of nanoparticles are cleared by the mononuclear phagocyte system, which is a part of immune system. Therefore, in order to minimal the immune response and improve the specificity, some researchers explored encapsulating nanoparticles into cells to deliver nanoparticles to tumor site. There are some kinds of cells including macrophages[121, 122] and stem cells[123, 124] have been investigated as carriers of nanoparticles for PTT application.

I. Macrophage

Macrophage is a kind of white blood cell and an important cell type of immune system. Macrophage

could recognize, engulf and digest foreign substances, abnormal cells and anything else that does not have healthy cell specific proteins on their surfaces. This process is called phagocytosis. Macrophages recently received much attention in cancer therapy application. Because numerous peripheral blood monocytes were recruited into tumor site during tumor development and once these monocytes crossed the endothelial basement membrane, they differentiated into tumor associated macrophages (TAMs). And these TAMs could promote tumor progression and it has been reported that TAMs can constitute up to 70% of tumor mass. Therefore, researchers hypothesized that using these tumor natural recruited monocytes for the delivery of nanoparticles. Since monocytes have innate phagocytosis ability, they can be easily loaded with nanoparticles and the differentiated macrophages can serve as delivery vectors for therapeutic nanoparticles getting into those inaccessible tumor regions. Some studies have demonstrated that both *in vitro* and *in vivo*, the gold nanoshell laden macrophages could migrate efficiently into malignant tumor and could achieve good therapeutic effect by NIR laser irradiation.[125]

II. Stem cell

It is well known that stem cell is a group of undifferentiated biological cells that can generate highly differentiated descendant with specific function. Stem cells have three main features: self-renewal, proliferation, and multi-potentiality. Since 2000, a number of *in vitro* and *in vivo* studies have discovered the unique migratory capacity of stem cells throughout the tumor site, which is called tumor-tropic property of stem cells. The precise mechanism of the tumor-tropic property of stem cell is still unknown. One of possible reason is that some chemokines and pro-angiogenic growth factors produced in the tumor microenvironment may function as attractants to induce stem cells into tumor site. Another possible mechanism is that the stem cells are recruited to the tumor site to repair damaged tissues. Based on the tumor-tropic property of stem cells, many researchers initiated to study stem cell-based delivery of anticancer agents into the tumor sites. This kind of stem cell-based system has minimal immunogenicity property and these modified stem cells could easily avoid the surveillance of immune system and cross the biological barriers to get into some deep areas of tumor such as tumor stroma and hypoxic tumor cores. Up to now, mesenchymal stem cells and neural stem cells are most commonly used for stem cell-based deliver system. Nanoparticles could be also loaded into stem cells to be transported into tumor site for PTT application. Some studies loaded pH-sensitive gold nanoparticles into mesenchymal stem cells for photothermal ablation of cancer cells. These pH-sensitive gold nanoparticles could aggregate under mild acidic conditions, which indicated that these gold nanoparticles could form large-sized aggregates in cells' endosomes, after uptake by the mesenchymal stem cells. Because of the large size of nanoparticle aggregates, they could prevent cell exocytosis. It could contribute to increasing the loading amount of gold nanoparticles in mesenchymal stem cells and retaining nanoparticles in tumor site for longer time. Both *in vitro* and *in vivo* results showed that it possessed high targeted efficiency, increased photothermal efficiency and therapeutic efficacy during NIR laser irradiation by using mesenchymal stem cells-delivered pH-sensitive gold nanoparticles.[123]

In brief, cell-mediated photothermal conversion agent delivery is a specific target and effective therapeutic system for PTT application. However, the specificity to tumor site of this system still needs to be improved and the safety of this method needs to be evaluated. This innovative therapeutic strategy may carry a substantial risk of secondary malignancy of the transformation of the implanted cells. Therefore, these engineered cells need to be extensively characterized before they can be considered as an appropriate method for clinical cancer treatment.

1.2.3.2 Scaffold carrier

Besides the cell carriers as mentioned above, scaffold-based photothermal conversion agent delivery has

been considered as an attractive way for PTT application. In this strategy, the photothermal conversion agents usually nanoparticles are immobilized on the surfaces of scaffold or embedded into scaffold matrix to prepare a composite scaffold with photothermal ability (Fig. 1.4). This kind of scaffold can be called photothermal scaffold. The photothermal scaffold can not only kill the cancer cells during NIR laser irradiation but also help the tissue recover and regeneration after tumor ablation.

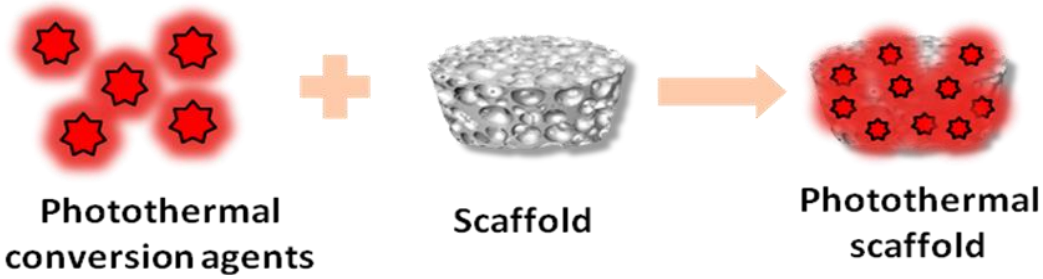

Fig. 1.4. Illustration of scaffold-based carrier for PTT.

1.3 Photothermal scaffold

It is well known that scaffold is one of the key factors of tissue engineering. During tissue regeneration, scaffolds act as temporary template to support cell adhesion, proliferation, and differentiation and scaffolds also play an important role in regulation cell behavior, cell function and tissue formation. Recently, some researchers combined biocompatible scaffold with photothermal conversion agent usually nanoparticles to prepare a composite scaffold. The composite scaffold possessed photothermal ability, which meant that the composite scaffold could elevate local temperature during NIR laser irradiation. There are some advantages of using photothermal scaffolds for PTT comparing to free nanoparticles. One of main advantage of photothermal scaffolds is that they can be directly implanted into the tumor site. Therefore, these immobilized photothermal conversion agents could be specially delivered and localized to the tumor site, which may contribute to achieving high heating efficiency.[111, 126] More importantly, because these photothermal conversion agents are immobilized on the surfaces of scaffold or embedded into scaffold matrix, they could be easily retained at the tumor site for relatively longer time without easy leakage than free nanoparticles and thus realize repeated local heating without losing photothermal efficiency for cancer cell ablation and this feature is particularly essential for enhancing therapeutic efficacy and preventing common recurrence of malignant cancer.[127] What' more, after tumor ablation, the subsequent tissue recovery and regeneration are also very important and the porous scaffolds are also support the penetration of healthy cells and regeneration of normal tissue.[128, 129]

1.3.1 Requirements of scaffold

Scaffold is a kind of three-dimensional material, which could support cell adhesion, proliferation and differentiation. Therefore, scaffolds should meet some requirements listed as below:[130-132]

I. Biocompatibility

Scaffolds should have noncytotoxicity and good biocompatibility to the cells and the surrounding tissues. And scaffolds should support cell adhesion, proliferation and differentiation. The scaffold materials

and their degradation by-products should be no toxicity and no negative effect on the other cells and tissues. Additionally, the implantation of scaffolds should not cause the immune response and inflammation. For the photothermal scaffolds, without NIR laser irradiation, the cells should well attach and proliferate on these scaffolds.

II. Porous structure

As mentioned above, one of advantages of using photothermal scaffold for PTT is that photothermal scaffold could not only efficiently kill cancer cells, but also support healthy cell penetration and normal tissue regeneration. Therefore, good pore structure of scaffolds is also very important. A scaffold with ideal porous structure should not only have high porosity but also many interconnected pores. The interconnected pore structure is beneficial to cell penetration into scaffold and homogenous distribution throughout the scaffolds. Moreover, the interconnected pores also contribute to adequate nutrients diffusion and waste transportation of cells.

III. Biodegradability

Scaffolds should be biodegradable *in vivo* environment and degradation rate should match the rate of new tissue formation. Finally, the implanted scaffold should be replaced by the new formed tissue.

IV. Mechanical property

The appropriate mechanical property of scaffolds is needed because scaffolds should be strong enough to resist surgical handling and withstand the contraction force of cells. What's more, the mechanical property of scaffolds should be also matched the implanted site.

1.3.2 Biomaterials for scaffold fabrication

Choosing an ideal biomaterial for scaffold fabrication is very important for biomedical applications. Large amounts of materials have been developed for scaffold preparation. Typically, there are three main kinds of biomaterials used for the fabrication of scaffolds, synthetic polymers, natural polymers and ceramics. Each kind of these biomaterials has their own advantages in tissue repair and regeneration.

1.3.2.1 Synthetic polymers

Biodegradable synthetic polymers used for scaffold fabrication have many advantages over other materials. One of key advantages is that the mechanical properties and degradation rate can be tailored to suit different applications. Moreover, it is easy for synthetic polymers to be processed into different shapes and modified with designed functional groups on the polymer chains. Many kinds of synthetic polymers have been developed for biomedical application, such as polyesters, polyanhydrides, polyurethanes and so on. Among all of these synthetic polymers, the most commonly investigated biodegradable synthetic polymers are polyesters and polyanhydrides.

Poly(glycolic acid) (PGA), poly(lactic acid) (PLA) and their copolymers poly(lactic acid-co-glycolic acid) (PLGA) are the most commonly used biodegradable polyesters in the biomedical fields.[133, 134] PGA is biodegradable, thermoplastic polyester with the simple linear structure. PGA could be easily hydrolysis due to the existence of ester linkage in its backbone. Therefore, the degradation time of PGA is quite short and PGA could be totally degraded after 4 weeks implantation. PLA is biodegradable and bioactive polyester derived from many renewable resources, such as starch and sugarcane. Because of the hydrophobicity of PLA, the degradation time of PLA is much longer than PGA. Usually, PLA takes more than two years for

complete absorption by human body *in vivo* environment. Therefore, their copolymer PLGA was developed to meet different application requirements. The degradation time could be easily changed by varying the monomer ratio GA and LA. When the monomer ratio of GA and LA is 50:50, the copolymer PLGA has fastest degradation rate and it takes about two months for complete degradation. Due to the advantages of these biodegradable polymers, PGA, PLA and PLGA has been investigated for biomedical applications such as tissue engineering, drug delivery and nanomedicine. Moreover, PLA has been used in clinical field to make screws and darts for meniscal repair, which is named Clearfix Mensical Dart/Screw. However, using these biodegradable polymers for biomedical applications still faces some challenges. For example, PGA, PLA or PLGA may cause some local inflammatory response and rejection, which is contributed to their massive release of acidic degradation by-products.

Polyanhydrides are a class of biodegradable polymers, which contain repeat anhydride bonds linked with polymer backbone chain. Because the degradation product of polyanhydrides is diacid monomers, which is non-toxic, biocompatible and could be metabolized and eliminated from the body, the main application of polyanhydrides is in the biomedical fields, such as drug delivery, medical products, pharmaceutical industry.[135, 136] Gliadel is a biomedical product made of polyanhydrides, which has been used in clinical field to treat brain cancer. The degradation time of polyanhydrides can be varied from days to years depending on the different composition. Due to their acidic degradation by-products, polyanhydrides could still cause some undesirable side effects after implantation.

1.3.2.2 Natural polymers

Natural polymers are another important class, which could be used for the fabrication of porous scaffolds. Natural polymers for biomedical applications have many advantages comparing with synthetic polymers. One of the major advantages of natural polymers is that they possessed some biochemical cues (arginine-glycine-aspartic (RGD)), which are beneficial to cell attachment and proliferation. And natural polymers are also biodegradable and the degradation products usually do not cause some toxic side effects. Many kinds of natural polymers have been developed for porous scaffolds fabrication such as collagen, gelatin, chitosan, silk fibroin and so on.

I. Collagen

Collagen is a natural protein, which is one of the main components of extracellular matrix (ECM) in normal tissues and collagen is the most abundant protein in human body, making up about 30% in the whole protein content. Up to now, there are about 28 types of collagen has been explored. But in human body, the content of type I collagen is over 90%. The basic structural unit of collagen is three amino acids glycine, proline, and hydroxyproline with a triple helix structure stabilized by hydrogen bonds. These collagen molecules pack together to form collagen fibrils, and then further assemble with each other to form collagen fibers to support cells and tissues. Collagen used as scaffold materials has been intensively studied. The results showed the collagen-based porous scaffold possessed good biocompatibility and biodegradability. However, because collagen is derived from different sources, it may cause some antigenic and immunogenic response after implantation *in vivo*.[137]

II. Gelatin

Gelatin is derived from collagen through hydrolyzing treatment of collagen. Using gelatin for preparation of porous scaffold has many advantages. First, because the same amino acid sequences as collagen, gelatin also has excellent biocompatibility, biodegradability and cell recognized RGD sequence, which could significantly improve infiltration, adhesion, spreading, and proliferation of cells in resulting scaffolds. Moreover, gelatin is a denatured product of collagen so it has much less antigenicity and

immunogenicity than collagen. In addition, gelatin is low-cost and easily available, which could be obtained from various sources such as porcine, bovine and fish. Gelatin can be categorized into type A gelatin and type B gelatin. Type A gelatin is obtained by using acid hydrolysis of collagen and its isoelectric point is at pH 7 ~ 9. Type B gelatin is obtained by using alkaline hydrolysis of collagen and its isoelectric point is at pH 4 ~ 5. A low temperature can lead the gelation of gelatin usually at 0 ~ 25 ℃, the exact gelation temperature of gelatin solution is dependent on the gelatin sources and concentration of gelatin solution. The higher the concentration of gelatin solution leads more quickly gelation at the same temperature. Porous gelatin scaffolds have been fabricated for different tissue regeneration such as skin,[138, 139] bone[140, 141] and cartilage.[142, 143] And the results confirmed porous gelatin scaffold could support and improve the cell attachment, proliferation and differentiation, which made it an ideal material for tissue recover and regeneration.

III. Chitosan

Chitosan is a kind of polysaccharide, which is derived from chitin, containing repeating units of D-glucosamine and N-acetyl-D-glucosamine. When the ratio of D-glucosamine number in chitin is over 50%, chitin becomes soluble in aqueous acid solution, which is called chitosan. Chitosan has been widely used in different fields, especially in biomedical fields. Recently, chitosan has been approved in the United States and Europe for use as bandages and hemostatic agents because its ability to quickly stop bleeding. Moreover, Chitosan is also a good drug carrier. Chitosan could become positive charge in acid solution because of the protonation of its amine groups and this positive charge could be maintained in neutral pH. Therefore, using chitosan for drug delivery could enhance the adsorption of drugs.[144] What' more, the chitosan-based porous scaffolds have been developed. Porous chitosan sponges are prepared for tissue engineering. The results showed chitosan-based porous scaffolds possessed good biocompatibility and could promote cell attach, proliferation and osteogenic differentiation of MSC cells.[145]

IV. Silk fibroin

Silk fibroin is a natural polymer obtained from various sources such as silkworms, spiders, and flies. Silk fibers could be obtained from diverse sources such as spiders, silkworms, scorpions, mites and flies. The structural units of silk fibroin are repeating amino acid sequences $(Gly\text{-}Ser\text{-}Gly\text{-}Ala\text{-}Gly\text{-}Ala)_n$. Among all of these silk fibroins, silk of silkworms is a promising scaffold material, which possesses good biocompatibility, suitable mechanical properties. *In vivo,* it takes about a few weeks for silk fibroin-based porous scaffolds disintegrating and after one year, the silk fibroin-based porous scaffolds could be completely degraded and absorbed.[146] Moreover, massive functional groups in the side chains of silk fibroin could be easily modified with some bioactive molecules and growth factors. It has been reported that RGD modified silk fibroin could promote the attachment, spreading, proliferation and differentiation of MSCs.[147] However, fibroin cannot dissolve in water and can be only dissolved in salt-containing aqueous solution and organic solvents.

1.3.2.3 Ceramics

Ceramic is an inorganic, nonmetallic solid material. In the biomedical field, the most commonly used ceramics are hydroxyapatite (HA) and beta-tricalcium phosphate (β-TCP). These bioceramics has been extensively studied for tissue regeneration, especially in bone tissue engineering, because they are similar to the inorganic component of and possessed excellent mechanical properties. It has been demonstrated that bioceramic porous scaffolds had not only good biocompatibility but also osteoconductive and osteoinductive properties on cell proliferation and differentiation.[148]

1.3.3 Preparation methods for porous scaffolds

As mentioned above, an ideal porous scaffold should not only have high porosity but also many interconnected pores. Most commonly used preparation methods for porous scaffolds can be categorized into fiber-related techniques, solid freeform methods and porogen-based methods.

I. Fiber-related techniques

Electrospinning is the most used fiber-related technique to prepare three-dimensional porous fiber mesh. Electrospinning is using electric force to produce charged fibers of polymer solutions with diameters ranging from several nanometers to micrometers. The electrospinning device contains a high voltage supplier, a syringe pump and a metal collector. Many kinds of polymer including natural polymer (collagen, cellulose, silk fibroin and so on) and synthetic polymer (PLGA, PLA, polyurethanes and so on) can be used this technique to prepare polymer fiber scaffolds. The advantages of this technique are that the prepared fiber scaffolds possessed high surface-to-volume ratio, tunable porosity, variable sizes and shapes and easy control the fiber composition to achieve desired properties and functionality. However, it still has some limitations. The pore size of electrospinning fiber mesh is too small Therefore, it is difficult for cells to penetrate or migrate into scaffold, resulting in the non-uniform cell distribution throughout the scaffolds. Moreover, the thickness of scaffold prepared by electrospinning is limited usually hundreds micrometers, which is not the truly three-dimensional structure. Additionally, the residue of organic solvent may have some toxicity to the cells.[149]

II. Solid freeform methods

Solid freeform methods can fabricate the scaffolds that have the complex structure. Usually, solid free-form methods usually contain two types of systems. One type is laser-based system such as selective laser sintering and stereolithography. The other type is printing-based system such as 3D printing. Now, using 3D printing to construct porous scaffolds has attracted growing interest. The pore structure including pore size, shape and porosity can be easily controlled by using 3D printing. Moreover, the printed pores are well interconnected, which is critical for cell distribution, penetration and tissue regeneration. What's more, 3D printing method can fabricate the porous scaffolds with different thickness and shape to meet the different application requirements. However, the limitations of 3D printing are that this technique requires expensive equipment, high printing temperature and limited kinds of material that can be printed by this technique.[150]

III. Porogen-based methods

In this method, porogens were thoroughly mixed with material solution and many kinds of porogen have been explored such as carbon dioxide (CO_2) gas, water, sodium chloride particles, paraffin microspheres and ice particulates.[151] After complete removal of the porogen in the mixture, a porous scaffold can be obtained. Most commonly used strategies of this method are gas foaming, particulate leaching and freeze-drying.

The typical preparation process of porous scaffold prepared by gas foaming is that first the polymer disks such as PLA, PGA or PLGA can be prepared by using heating and compression, or by drying a polymer solution. Then the polymer disk is put in a chamber filled with high pressure CO_2 and equilibrated for more than 72 h at room temperature. Finally the CO_2 in the chamber releases within 15 seconds to attain the atmospheric pressure and the CO_2 gas in the polymer disk nucleate and form bubbles resulting in a highly porous scaffold. By using this method, porosity of polymer scaffolds can be as high as 93%. However, there

are still some limitations of this method. Although high porosity can be achieved, the pores created by this method are usually closed and lack of good interconnectivity.[152]

Particle leaching method can make the porous scaffolds with controlled porosity and pore size by adjusting the ratio and size of porogen. Typically, polymer solution is homogenously mixed with porogen then the mixture is put in a designed mold. After removal of porogen, the porous polymer scaffolds can be formed. Many kinds of materials can be acted as porogen such as the inorganic particles such as sodium chloride particles and organic particles such as paraffin, alginate or gelatin microspheres. The removal of these porogen can be achieved by dissolving porogen in an approperiate solvent such as water for sodium chloride particles or aliphalic solvent for paraffin microspheres. This method has been widely used to prepare porous scaffolds with controlled pore structure.[153] However, the thickness of porous scaffolds prepared by this method is limited because of the need of complete removal of porogen in polymer matrix. Moreover, the independent porogen cannot connect with each other indicating the poor interconnectivity of porous scaffolds. What's more, In addition, the incomplete removal of porogen and solvent residue may lead cytotoxicity to cells or decrease the efficacy of bioactive molecules.

Freeze-drying is one of the most commonly used methods for porous scaffolds preparation. This method usually comprises two stages. First, the polymer solution freezes at low temperature and ice crystals are formed in the freezing process. And then the surrounding pressure reduces and the frozen water in the material directly sublimate directly from the solid phase to the gas phase to form the pores in the scaffolds.[154] However, the main problem of this method is the random pore structure formed in the polymer matrix.

Recently, ice particulate have emerged as an ideal porogen material which combines the particle leaching and freeze-drying strategies to prepare porous polymer scaffolds (Fig. 1.5). Because the ice particulates are made of water, there is no toxicity to the cells or bioactive molecules. Moreover, the size of ice particulates can be easily controlled by the purchased sieves. By varying the adding amount of ice particulates, the porosity can be also changed. More importantly, during freezing process, many small ice crystals were in-situ formed around the added large ice particulates and they could also serve as porogen. After freeze-drying, many small pores are formed and connect the spherical large pores with each other, which could significantly improve the interconnectivity of porous scaffolds. Previous studies have proved that the cells can be homogenous distributed not only on the surfaces but also inside the porous scaffolds by using ice particulates as porogen and the homogenous cell distribution could beneficial to the subsequent tissue regeneration.[155, 156]

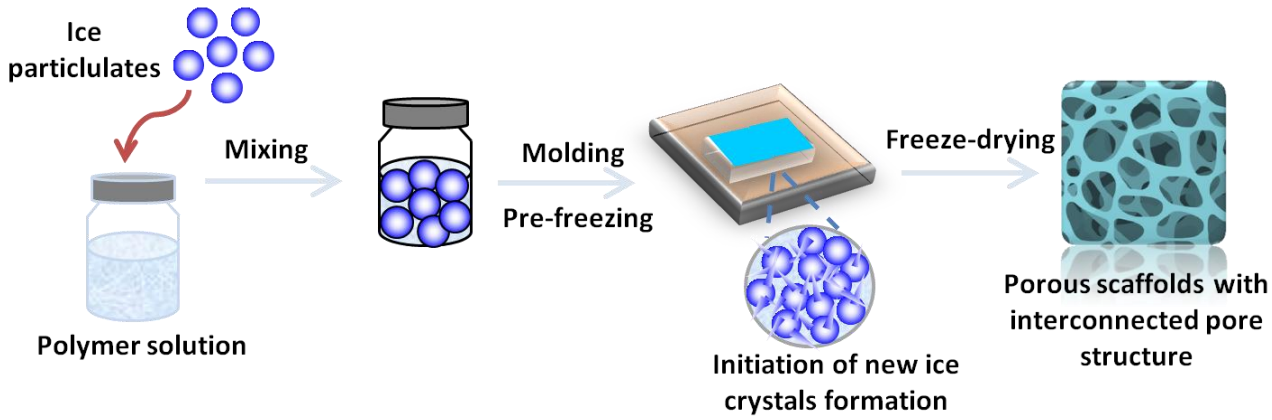

Fig. 1.5. Ice particulates as porogen for preparation of porous scaffolds.

1.4 Motivation, objectives and outline

1.4.1 Motivation and objectives

Comparing with the traditional methods for cancer treatment, PTT is a new strategy for cancer treatment with non-invasive and excellent therapeutic efficacy. However, low specificity and easy diffusion of nanoparticles which are the mainly used as photothermal converision agents restrict the current PTT for clinical applications. Recently, photothermal scaffolds have emerged as carriers to deliver photothermal conversion agents for efficient PTT. Using photothermal scaffolds for PTT have some advantages comparing with free nanoparticles such as the high specificity and excellent repeating heating efficiency. What's more, the photothermal scaffolds can also help the tissue recover and regeneration after tumor ablation. Up to now, there are some studies reported using nanoparticle-immobilized scaffolds for PTT application. However, most of the studies are using electrospinning scaffolds or injectable hydrogel for PTT and these kinds of scaffolds are lack of interconnected porous structure for cells penetration and regeneration after cancer cell ablation. Moreover, after the tumor ablation, there may be still some cancer cells remained, which could lead cancer recurrence. Therefore, a multifunctional photothermal scaffold with cancer cell capture ability is highly needed. Inspired by all of these issues, the objective of my study is to prepare porous photothermal scaffolds with high photothermal efficiency and cancer cell killing efficiency for PTT applications. Moreover, the specifically capture and kill cancer cells by the implanted photothermal scaffolds were also studied. Because the properties of immobilized photothermal conversion agents could affect the heating efficiency, the influence of nanoparticles properties on therapeutic efficacy of photothermal scaffolds was compared and discussed.

1.4.2 Outlines

In this study, porous gelatin (Gel) scaffolds were prepared as a carrier to deliver photothermal nanoparticles. The porous Gel scaffolds were prepared by a facile ice particulate templating method. Different kinds of photothermal conversion agents including iron oxide nanoparticles (Fe_3O_4) and gold nanoparticles were incorporated into porous Gel scaffolds for photothermal ablation of cancer cells.

In chapter 2, porous gelatin/iron oxide (Gel/Fe_3O_4) composite scaffolds were prepared by using ice particulates as porogen. The killing efficiency and repeated therapeutic efficiency of Gel/Fe_3O_4 composite scaffolds for cancer cells were studied by NIR laser irradiation.

In chapter 3, folic acid (FA), which could be used as a cancer cell targeting ligand, were introduced into porous Gel/Fe_3O_4 composite scaffolds to enhance the cancer cell capture ability of scaffolds. The capture efficiency and killing efficiency of Gel/Fe_3O_4-FA scaffolds with different FA grafting density were investigated

In chapter 4, porous composite scaffolds of Gel and gold nanoparticles with tunable particle size and shape were prepared for PTT application. The heating efficiency and killing efficiency of composite scaffolds with different gold nanoparticles size and shape were compared and discussed.

Chapter 5 gives the general conclusions and future perspective of this thesis.

1.5 References

1. Slooten, H. V.; Schaberg, A.; Smeenk, D.; Moolenaar, A. J., Morphologic characteristics of benign and malignant adrenocortical tumors. *Cancer* **1985,** 55, (4), 766-773.

2. Cifone, M. A., In vitro growth characteristics associated with benign and metastatic variants of tumor

cells. *Cancer Metastasis Rev.* **1982,** 1, (4), 335-347.
3. Jiao, L. R.; Frampton, A. E.; Jacob, J.; Pellegrino, L.; Krell, J.; Giamas, G.; Tsim, N.; Vlavianos, P.; Cohen, P.; Ahmad, R., MicroRNAs targeting oncogenes are down-regulated in pancreatic malignant transformation from benign tumors. *PLoS One* **2012,** 7, (2), e32068.
4. Quirke, P.; Dixon, M.; Durdey, P.; Williams, N., Local recurrence of rectal adenocarcinoma due to inadequate surgical resection: histopathological study of lateral tumour spread and surgical excision. *The Lancet* **1986,** 328, (8514), 996-999.
5. Bird, J. E., Advances in the surgical management of bone tumors. *Curr Oncol Rep* **2014,** 16, (7), 1-6.
6. Byfield, J. E.; Calabro-Jones, P. M., Carrier-dependent and carrier-independent transport of anti-cancer alkylating agents. *Nature* **1981,** 294, 281-283.
7. Parker, W. B., Enzymology of purine and pyrimidine antimetabolites used in the treatment of cancer. *Chem. Rev.* **2009,** 109, (7), 2880-2893.
8. Zhao J.S., J.; Reed, E.; LI, Q. Q., Molecular mechanism of antitumor activity of taxanes in lung cancer. *Int. J. Oncol.* **2005,** 27, 247-256.
9. Davis, A.; Jiang, J.-D.; Middleton, K. M.; Wang, Y.; Weisz, I.; Ling, Y.-H.; Bekesi, J. G., Novel suicide ligands of tubulin arrest cancer cells in S-phase. *Neoplasia* **1999,** 1, (6), 498-507.
10. Drake, F. H.; Hofmann, G. A.; Mong, S.-M.; Bartu, J. O. L.; Hertzberg, R. P.; Johnson, R. K.; Mattern, M. R.; Mirabelli, C. K., In vitro and intracellular inhibition of topoisomerase II by the antitumor agent merbarone. *Cancer Res* **1989,** 49, (10), 2578-2583.
11. Baskar, R.; Lee, K. A.; Yeo, R.; Yeoh, K.-W., Cancer and radiation therapy: current advances and future directions. *Int J Med Sci* **2012,** 9, (3), 193-199.
12. Rosenberg, S. A.; Yang, J. C.; Restifo, N. P., Cancer immunotherapy: moving beyond current vaccines. *Nat. Med.* **2004,** 10, (9), 909-915.
13. Figdor, C. G.; de Vries, I. J. M.; Lesterhuis, W. J.; Melief, C. J., Dendritic cell immunotherapy: mapping the way. *Nat. Med.* **2004,** 10, (5), 475-480.
14. Adams, G. P.; Weiner, L. M., Monoclonal antibody therapy of cancer. *Nat. Biotechnol.* **2005,** 23, (9), 1147-1157.
15. Couzin-Frankel, J., Cancer immunotherapy. *Science* **2013,** 342, (6165), 1432-1433.
16. Edelstein, M. L.; Abedi, M. R.; Wixon, J., Gene therapy clinical trials worldwide to 2007—an update. *J. Gene Med.* **2007,** 9, (10), 833-842.
17. Thomas, C. E.; Ehrhardt, A.; Kay, M. A., Progress and problems with the use of viral vectors for gene therapy. *Nat. Rev. Genet.* **2003,** 4, (5), 346-358.
18. Li, S.-d.; Huang, L.-y., Nonviral gene therapy: promises and challenges. *Gene Ther.* **2000,** 7, (1), 31-34.
19. Dolmans, D. E.; Fukumura, D.; Jain, R. K., Photodynamic therapy for cancer. *Nat. Rev. Cancer* **2003,** 3, (5), 380-387.
20. Jori, G.; Fabris, C.; Soncin, M.; Ferro, S.; Coppellotti, O.; Dei, D.; Fantetti, L.; Chiti, G.; Roncucci, G., Photodynamic therapy in the treatment of microbial infections: basic principles and perspective applications. *Lasers Surg. Med.* **2006,** 38, (5), 468-481.
21. Hongcharu, W.; Taylor, C. R.; Aghassi, D.; Suthamjariya, K.; Anderson, R. R.; Chang, Y., Topical ALA-photodynamic therapy for the treatment of acne vulgaris. *J. Invest. Dermatol.* **2000,** 115, (2), 183-192.
22. Levy, J. G. Photosensitizers in photodynamic therapy, *Semin. Oncol.* 1994; 1994; pp 4-10.
23. Brown, S. B.; Brown, E. A.; Walker, I., The present and future role of photodynamic therapy in cancer treatment. *The lancet oncology* **2004,** 5, (8), 497-508.
24. Strohbehn, J. W.; Douple, E. B., Hyperthermia and cancer therapy: a review of biomedical engineering

contributions and challenges. *IEEE Trans. Biomed. Eng.* **1984**, (12), 779-787.
25. Kennedy, J. E., High-intensity focused ultrasound in the treatment of solid tumours. *Nat. Rev. Cancer* **2005,** 5, (4), 321-327.
26. Madersbacher, S.; Pedevilla, M.; Vingers, L.; Susani, M.; Marberger, M., Effect of high-intensity focused ultrasound on human prostate cancer in vivo. *Cancer Res* **1995,** 55, (15), 3346-3351.
27. Tateishi, R.; Shiina, S.; Teratani, T.; Obi, S.; Sato, S.; Koike, Y.; Fujishima, T.; Yoshida, H.; Kawabe, T.; Omata, M., Percutaneous radiofrequency ablation for hepatocellular carcinoma. *Cancer* **2005,** 103, (6), 1201-1209.
28. Goldberg, S. N.; Gazelle, G. S.; Compton, C. C.; Mueller, P. R.; Tanabe, K. K., Treatment of intrahepatic malignancy with radiofrequency ablation. *Cancer* **2000,** 88, (11), 2452-2463.
29. Jordan, A.; Scholz, R.; Wust, P.; Fähling, H.; Felix, R., Magnetic fluid hyperthermia (MFH): Cancer treatment with AC magnetic field induced excitation of biocompatible superparamagnetic nanoparticles. *J. Magn. Magn. Mater.* **1999,** 201, (1), 413-419.
30. Hergt, R.; Dutz, S.; Müller, R.; Zeisberger, M., Magnetic particle hyperthermia: nanoparticle magnetism and materials development for cancer therapy. *J. Phys. Condens. Matter* **2006,** 18, (38), S2919.
31. O'Neal, D. P.; Hirsch, L. R.; Halas, N. J.; Payne, J. D.; West, J. L., Photo-thermal tumor ablation in mice using near infrared-absorbing nanoparticles. *Cancer Lett.* **2004,** 209, (2), 171-176.
32. El-Sayed, I. H.; Huang, X.; El-Sayed, M. A., Selective laser photo-thermal therapy of epithelial carcinoma using anti-EGFR antibody conjugated gold nanoparticles. *Cancer Lett.* **2006,** 239, (1), 129-135.
33. Huang, X.; Jain, P. K.; El-Sayed, I. H.; El-Sayed, M. A., Plasmonic photothermal therapy (PPTT) using gold nanoparticles. *Lasers Med. Sci.* **2008,** 23, (3), 217-228.
34. Chen, Q.; Wang, C.; Zhan, Z.; He, W.; Cheng, Z.; Li, Y.; Liu, Z., Near-infrared dye bound albumin with separated imaging and therapy wavelength channels for imaging-guided photothermal therapy. *Biomaterials* **2014,** 35, (28), 8206-8214.
35. Jiao, F.; Jumas, J.-C.; Womes, M.; Chadwick, A. V.; Harrison, A.; Bruce, P. G., Synthesis of ordered mesoporous Fe3O4 and γ-Fe2O3 with crystalline walls using post-template reduction/oxidation. *J. Am. Chem. Soc.* **2006,** 128, (39), 12905-12909.
36. Gao, J.; Gu, H.; Xu, B., Multifunctional magnetic nanoparticles: design, synthesis, and biomedical applications. *Acc. Chem. Res.* **2009,** 42, (8), 1097-1107.
37. Hao, R.; Xing, R.; Xu, Z.; Hou, Y.; Gao, S.; Sun, S., Synthesis, functionalization, and biomedical applications of multifunctional magnetic nanoparticles. *Adv. Mater.* **2010,** 22, (25), 2729-2742.
38. Jun, Y.-w.; Seo, J.-w.; Cheon, J., Nanoscaling laws of magnetic nanoparticles and their applicabilities in biomedical sciences. *Acc. Chem. Res.* **2008,** 41, (2), 179-189.
39. Zhang, Y.; Liu, J.-Y.; Ma, S.; Zhang, Y.-J.; Zhao, X.; Zhang, X.-D.; Zhang, Z.-D., Synthesis of PVP-coated ultra-small Fe_3O_4 nanoparticles as a MRI contrast agent. *J. Mate. Sci. Mater. Med.* **2010,** 21, (4), 1205-1210.
40. Xu, B.; Dou, H.; Tao, K.; Sun, K.; Ding, J.; Shi, W.; Guo, X.; Li, J.; Zhang, D.; Sun, K., "Two-in-One" fabrication of Fe_3O_4/MePEG-PLA composite nanocapsules as a potential ultrasonic/MRI dual contrast agent. *Langmuir* **2011,** 27, (19), 12134-12142.
41. Zeng, J.; Jing, L.; Hou, Y.; Jiao, M.; Qiao, R.; Jia, Q.; Liu, C.; Fang, F.; Lei, H.; Gao, M., Anchoring group effects of surface ligands on magnetic properties of Fe3O4 nanoparticles: towards high performance MRI contrast agents. *Adv. Mater.* **2014,** 26, (17), 2694-2698.
42. Cao, S.-W.; Zhu, Y.-J.; Ma, M.-Y.; Li, L.; Zhang, L., Hierarchically nanostructured magnetic hollow spheres of Fe3O4 and γ-Fe2O3: preparation and potential application in drug delivery. *J. Phys. Chem. C*

2008, 112, (6), 1851-1856.
43. Kim, J.; Lee, J. E.; Lee, S. H.; Yu, J. H.; Lee, J. H.; Park, T. G.; Hyeon, T., Designed fabrication of a multifunctional polymer nanomedical platform for simultaneous cancer-targeted imaging and magnetically guided drug delivery. *Adv. Mater.* **2008,** 20, (3), 478-483.
44. Li, L.; Chen, D.; Zhang, Y.; Deng, Z.; Ren, X.; Meng, X.; Tang, F.; Ren, J.; Zhang, L., Magnetic and fluorescent multifunctional chitosan nanoparticles as a smart drug delivery system. *Nanotechnology* **2007,** 18, (40), 405102.
45. Fortin, J.-P.; Wilhelm, C.; Servais, J.; Ménager, C.; Bacri, J.-C.; Gazeau, F., Size-sorted anionic iron oxide nanomagnets as colloidal mediators for magnetic hyperthermia. *J. Am. Chem. Soc.* **2007,** 129, (9), 2628-2635.
46. Sonvico, F.; Mornet, S.; Vasseur, S.; Dubernet, C.; Jaillard, D.; Degrouard, J.; Hoebeke, J.; Duguet, E.; Colombo, P.; Couvreur, P., Folate-conjugated iron oxide nanoparticles for solid tumor targeting as potential specific magnetic hyperthermia mediators: synthesis, physicochemical characterization, and in vitro experiments. *Bioconjugate Chem.* **2005,** 16, (5), 1181-1188.
47. Thomas, L. A.; Dekker, L.; Kallumadil, M.; Southern, P.; Wilson, M.; Nair, S. P.; Pankhurst, Q. A.; Parkin, I. P., Carboxylic acid-stabilised iron oxide nanoparticles for use in magnetic hyperthermia. *J. Mater. Chem.* **2009,** 19, (36), 6529-6535.
48. Chu, M.; Shao, Y.; Peng, J.; Dai, X.; Li, H.; Wu, Q.; Shi, D., Near-infrared laser light mediated cancer therapy by photothermal effect of Fe 3 O 4 magnetic nanoparticles. *Biomaterials* **2013,** 34, (16), 4078-4088.
49. Shen, S.; Kong, F.; Guo, X.; Wu, L.; Shen, H.; Xie, M.; Wang, X.; Jin, Y.; Ge, Y., CMCTS stabilized Fe 3 O 4 particles with extremely low toxicity as highly efficient near-infrared photothermal agents for in vivo tumor ablation. *Nanoscale* **2013,** 5, (17), 8056-8066.
50. Chen, H.; Burnett, J.; Zhang, F.; Zhang, J.; Paholak, H.; Sun, D., Highly crystallized iron oxide nanoparticles as effective and biodegradable mediators for photothermal cancer therapy. *J. Mater. Chem. B* **2014,** 2, (7), 757-765.
51. Zhou, Z.; Sun, Y.; Shen, J.; Wei, J.; Yu, C.; Kong, B.; Liu, W.; Yang, H.; Yang, S.; Wang, W., Iron/iron oxide core/shell nanoparticles for magnetic targeting MRI and near-infrared photothermal therapy. *Biomaterials* **2014,** 35, (26), 7470-7478.
52. Song, X.; Gong, H.; Yin, S.; Cheng, L.; Wang, C.; Li, Z.; Li, Y.; Wang, X.; Liu, G.; Liu, Z., Ultra-small iron oxide doped polypyrrole nanoparticles for *in vivo* multimodal imaging guided photothermal therapy. *Adv. Funct. Mater.* **2014,** 24, (9), 1194-1201.
53. Hariani, P. L.; Faizal, M.; Setiabudidaya, D., Synthesis and properties of Fe_3O_4 nanoparticles by co-precipitation method to removal procion dye. *Inter. J. Environ. Sci. Dev.***2013,** 4, (3), 336.
54. Wu, K.; Kuo, P.; Yao, Y.; Tsai, E., Magnetic and optical properties of Fe 3 O 4 nanoparticle ferrofluids prepared by coprecipitation technique. *IEEE Trans. Magn.* **2001,** 37, (4), 2651-2653.
55. Xu, C.; Ouyang, C.; Jia, R.; Li, Y.; Wang, X., Magnetic and optical properties of poly (vinylidene difluoride)/Fe3O4 nanocomposite prepared by coprecipitation approach. *J. Appl. Polym. Sci.* **2009,** 111, (4), 1763-1768.
56. Liz, L.; Quintela, M. L.; Mira, J.; Rivas, J., Preparation of colloidal Fe3O4 ultrafine particles in microemulsions. *J. Mater. Sci.* **1994,** 29, (14), 3797-3801.
57. Liu, Z.; Wang, X.; Yao, K.; Du, G.; Lu, Q.; Ding, Z.; Tao, J.; Ning, Q.; Luo, X.; Tian, D., Synthesis of magnetite nanoparticles in W/O microemulsion. *J. Mater. Sci.* **2004,** 39, (7), 2633-2636.
58. Santra, S.; Tapec, R.; Theodoropoulou, N.; Dobson, J.; Hebard, A.; Tan, W., Synthesis and characterization of silica-coated iron oxide nanoparticles in microemulsion: the effect of nonionic surfactants.

Langmuir **2001,** 17, (10), 2900-2906.
59. Roca, A.; Morales, M.; O'Grady, K.; Serna, C., Structural and magnetic properties of uniform magnetite nanoparticles prepared by high temperature decomposition of organic precursors. *Nanotechnology* **2006,** 17, (11), 2783.
60. Sun, J.; Zhou, S.; Hou, P.; Yang, Y.; Weng, J.; Li, X.; Li, M., Synthesis and characterization of biocompatible Fe_3O_4 nanoparticles. *J. Biomed. Mater. Res. A* **2007,** 80, (2), 333-341.
61. Mieszawska, A. J.; Mulder, W. J.; Fayad, Z. A.; Cormode, D. P., Multifunctional gold nanoparticles for diagnosis and therapy of disease. *Mol. Pharmaceutics* **2013,** 10, (3), 831-847.
62. Naczynski, D.; Tan, M.; Zevon, M.; Wall, B.; Kohl, J.; Kulesa, A.; Chen, S.; Roth, C.; Riman, R.; Moghe, P., Rare-earth-doped biological composites as *in vivo* shortwave infrared reporters. *Nat. Commun.* **2013,** 4.
63. Banerjee, S. S.; Chen, D.-H., A multifunctional magnetic nanocarrier bearing fluorescent dye for targeted drug delivery by enhanced two-photon triggered release. *Nanotechnology* **2009,** 20, (18), 185103.
64. Huang, X.; El-Sayed, I. H.; Qian, W.; El-Sayed, M. A., Cancer cell imaging and photothermal therapy in the near-infrared region by using gold nanorods. *J. Am. Chem. Soc.* **2006,** 128, (6), 2115-2120.
65. Jang, B.; Park, J.-Y.; Tung, C.-H.; Kim, I.-H.; Choi, Y., Gold nanorod− photosensitizer complex for near-infrared fluorescence imaging and photodynamic/photothermal therapy in vivo. *ACS Nano* **2011,** 5, (2), 1086-1094.
66. Niidome, T.; Yamagata, M.; Okamoto, Y.; Akiyama, Y.; Takahashi, H.; Kawano, T.; Katayama, Y.; Niidome, Y., PEG-modified gold nanorods with a stealth character for in vivo applications. *J. Controlled Release* **2006,** 114, (3), 343-347.
67. Wang, S.; Huang, P.; Nie, L.; Xing, R.; Liu, D.; Wang, Z.; Lin, J.; Chen, S.; Niu, G.; Lu, G., Single continuous wave laser induced photodynamic/plasmonic photothermal therapy using photosensitizer-functionalized gold nanostars. *Adv. Mater.* **2013,** 25, (22), 3055-3061.
68. Yuan, H.; Fales, A. M.; Vo-Dinh, T., TAT peptide-functionalized gold nanostars: enhanced intracellular delivery and efficient NIR photothermal therapy using ultralow irradiance. *J. Am. Chem. Soc.* **2012,** 134, (28), 11358-11361.
69. Nergiz, S. Z.; Gandra, N.; Tadepalli, S.; Singamaneni, S., Multifunctional hybrid nanopatches of graphene oxide and gold nanostars for ultraefficient photothermal cancer therapy. *ACS Appl. Mater. Interfaces* **2014,** 6, (18), 16395-16402.
70. Ma, Y.; Liang, X.; Tong, S.; Bao, G.; Ren, Q.; Dai, Z., Gold nanoshell nanomicelles for potential magnetic resonance imaging, light-triggered drug release, and photothermal therapy. *Adv. Funct. Mater.* **2013,** 23, (7), 815-822.
71. Liu, H.; Chen, D.; Li, L.; Liu, T.; Tan, L.; Wu, X.; Tang, F., Multifunctional gold nanoshells on silica nanorattles: a platform for the combination of photothermal therapy and chemotherapy with low systemic toxicity. *Angew. Chem. Int. Ed. Engl.* **2011,** 123, (4), 921-925.
72. Ji, X.; Shao, R.; Elliott, A. M.; Stafford, R. J.; Esparza-Coss, E.; Bankson, J. A.; Liang, G.; Luo, Z.-P.; Park, K.; Markert, J. T., Bifunctional gold nanoshells with a superparamagnetic iron oxide-silica core suitable for both MR imaging and photothermal therapy. *J. Phys. Chem. C* **2007,** 111, (17), 6245-6251.
73. Chen, J.; Wang, D.; Xi, J.; Au, L.; Siekkinen, A.; Warsen, A.; Li, Z.-Y.; Zhang, H.; Xia, Y.; Li, X., Immuno gold nanocages with tailored optical properties for targeted photothermal destruction of cancer cells. *Nano Lett.* **2007,** 7, (5), 1318-1322.
74. Chen, J.; Glaus, C.; Laforest, R.; Zhang, Q.; Yang, M.; Gidding, M.; Welch, M. J.; Xia, Y., Gold nanocages as photothermal transducers for cancer treatment. *Small* **2010,** 6, (7), 811-817.

75. Skrabalak, S. E.; Chen, J.; Au, L.; Lu, X.; Li, X.; Xia, Y., Gold nanocages for biomedical applications. *Adv. Mater.* **2007,** 19, (20), 3177-3184.
76. Zhang, J. Z., Biomedical applications of shape-controlled plasmonic nanostructures: a case study of hollow gold nanospheres for photothermal ablation therapy of cancer. *J. Phys. Chem. Lett.* **2010,** 1, (4), 686-695.
77. You, J.; Zhang, R.; Zhang, G.; Zhong, M.; Liu, Y.; Van Pelt, C. S.; Liang, D.; Wei, W.; Sood, A. K.; Li, C., Photothermal-chemotherapy with doxorubicin-loaded hollow gold nanospheres: a platform for near-infrared light-trigged drug release. *J. Controlled Release* **2012,** 158, (2), 319-328.
78. Lu, W.; Xiong, C.; Zhang, G.; Huang, Q.; Zhang, R.; Zhang, J. Z.; Li, C., Targeted photothermal ablation of murine melanomas with melanocyte-stimulating hormone analog–conjugated hollow gold nanospheres. *Clin. Cancer Res.* **2009,** 15, (3), 876-886.
79. Li, J.; Cai, R.; Kawazoe, N.; Chen, G., Facile preparation of albumin-stabilized gold nanostars for the targeted photothermal ablation of cancer cells. *J. Mater. Chem. B* **2015,** 3, (28), 5806-5814.
80. Wang, Y.; Polavarapu, L.; Liz-Marzán, L. M., Reduced graphene oxide-supported gold nanostars for improved SERS sensing and drug delivery. *ACS Appl. Mater. Interfaces* **2014,** 6, (24), 21798-21805.
81. Lal, S.; Clare, S. E.; Halas, N. J., Nanoshell-enabled photothermal cancer therapy: impending clinical impact. *Acc. Chem. Res.* **2008,** 41, (12), 1842-1851.
82. Chen, J.; Saeki, F.; Wiley, B. J.; Cang, H.; Cobb, M. J.; Li, Z.-Y.; Au, L.; Zhang, H.; Kimmey, M. B.; Li, X., Gold nanocages: bioconjugation and their potential use as optical imaging contrast agents. *Nano Lett.* **2005,** 5, (3), 473-477.
83. Yang, X.; Skrabalak, S. E.; Li, Z.-Y.; Xia, Y.; Wang, L. V., Photoacoustic tomography of a rat cerebral cortex in vivo with Au nanocages as an optical contrast agent. *Nano Lett.* **2007,** 7, (12), 3798-3802.
84. Cherukuri, P.; Bachilo, S. M.; Litovsky, S. H.; Weisman, R. B., Near-infrared fluorescence microscopy of single-walled carbon nanotubes in phagocytic cells. *J. Am. Chem. Soc.* **2004,** 126, (48), 15638-15639.
85. Welsher, K.; Liu, Z.; Sherlock, S. P.; Robinson, J. T.; Chen, Z.; Daranciang, D.; Dai, H., A route to brightly fluorescent carbon nanotubes for near-infrared imaging in mice. *Nat. Nanotechnol.* **2009,** 4, (11), 773-780.
86. Welsher, K.; Liu, Z.; Daranciang, D.; Dai, H., Selective probing and imaging of cells with single walled carbon nanotubes as near-infrared fluorescent molecules. *Nano Lett.* **2008,** 8, (2), 586-590.
87. De La Zerda, A.; Zavaleta, C.; Keren, S.; Vaithilingam, S.; Bodapati, S.; Liu, Z.; Levi, J.; Smith, B. R.; Ma, T.-J.; Oralkan, O., Carbon nanotubes as photoacoustic molecular imaging agents in living mice. *Nat. Nanotechnol.* **2008,** 3, (9), 557-562.
88. Kim, J.-W.; Galanzha, E. I.; Shashkov, E. V.; Moon, H.-M.; Zharov, V. P., Golden carbon nanotubes as multimodal photoacoustic and photothermal high-contrast molecular agents. *Nat. Nanotechnol.* **2009,** 4, (10), 688-694.
89. Zerda, A. d. l.; Liu, Z.; Bodapati, S.; Teed, R.; Vaithilingam, S.; Khuri-Yakub, B. T.; Chen, X.; Dai, H.; Gambhir, S. S., Ultrahigh sensitivity carbon nanotube agents for photoacoustic molecular imaging in living mice. *Nano Lett.* **2010,** 10, (6), 2168-2172.
90. Bianco, A.; Kostarelos, K.; Prato, M., Applications of carbon nanotubes in drug delivery. *Curr. Opin. Chem. Biol.* **2005,** 9, (6), 674-679.
91. Liu, Z.; Chen, K.; Davis, C.; Sherlock, S.; Cao, Q.; Chen, X.; Dai, H., Drug delivery with carbon nanotubes for in vivo cancer treatment. *Cancer Res* **2008,** 68, (16), 6652-6660.
92. Liu, Z.; Sun, X.; Nakayama-Ratchford, N.; Dai, H., Supramolecular chemistry on water-soluble carbon nanotubes for drug loading and delivery. *ACS Nano* **2007,** 1, (1), 50-56.

93. Moon, H. K.; Lee, S. H.; Choi, H. C., *In vivo* near-infrared mediated tumor destruction by photothermal effect of carbon nanotubes. *ACS Nano* **2009,** 3, (11), 3707-3713.
94. Zhou, F.; Xing, D.; Ou, Z.; Wu, B.; Resasco, D. E.; Chen, W. R., Cancer photothermal therapy in the near-infrared region by using single-walled carbon nanotubes. *J. Biomed. Opt.* **2009,** 14, (2), 021009-021009-7.
95. Wang, X.; Wang, C.; Cheng, L.; Lee, S.-T.; Liu, Z., Noble metal coated single-walled carbon nanotubes for applications in surface enhanced Raman scattering imaging and photothermal therapy. *J. Am. Chem. Soc.* **2012,** 134, (17), 7414-7422.
96. Feng, L.; Zhang, S.; Liu, Z., Graphene based gene transfection. *Nanoscale* **2011,** 3, (3), 1252-1257.
97. Shen, H.; Zhang, L.; Liu, M.; Zhang, Z., Biomedical applications of graphene. *Theranostics* **2012,** 2, (3), 283-294.
98. Goenka, S.; Sant, V.; Sant, S., Graphene-based nanomaterials for drug delivery and tissue engineering. *J. Controlled Release* **2014,** 173, 75-88.
99. Depan, D.; Shah, J.; Misra, R., Controlled release of drug from folate-decorated and graphene mediated drug delivery system: synthesis, loading efficiency, and drug release response. *Mater. Sci. Eng. C* **2011,** 31, (7), 1305-1312.
100. Islam, M.; Kouzani, A. Z.; Dai, X. J.; Michalski, W. P.; Gholamhosseini, H., Design and analysis of a multilayer localized surface plasmon resonance Graphene biosensor. *J. Biomed. Nanotechnol.* **2012,** 8, (3), 380-393.
101. Shao, Y.; Wang, J.; Wu, H.; Liu, J.; Aksay, I. A.; Lin, Y., Graphene based electrochemical sensors and biosensors: a review. *Electroanalysis* **2010,** 22, (10), 1027-1036.
102. Yang, K.; Hu, L.; Ma, X.; Ye, S.; Cheng, L.; Shi, X.; Li, C.; Li, Y.; Liu, Z., Multimodal imaging guided photothermal therapy using functionalized graphene nanosheets anchored with magnetic nanoparticles. *Adv. Mater.* **2012,** 24, (14), 1868-1872.
103. Yang, K.; Zhang, S.; Zhang, G.; Sun, X.; Lee, S.-T.; Liu, Z., Graphene in mice: ultrahigh in vivo tumor uptake and efficient photothermal therapy. *Nano Lett.* **2010,** 10, (9), 3318-3323.
104. Sun, X.; Liu, Z.; Welsher, K.; Robinson, J. T.; Goodwin, A.; Zaric, S.; Dai, H., Nano-graphene oxide for cellular imaging and drug delivery. *Nano Res.* **2008,** 1, (3), 203-212.
105. Robinson, J. T.; Tabakman, S. M.; Liang, Y.; Wang, H.; Sanchez Casalongue, H.; Vinh, D.; Dai, H., Ultrasmall reduced graphene oxide with high near-infrared absorbance for photothermal therapy. *J. Am. Chem. Soc.* **2011,** 133, (17), 6825-6831.
106. Zhang, W.; Guo, Z.; Huang, D.; Liu, Z.; Guo, X.; Zhong, H., Synergistic effect of chemo-photothermal therapy using PEGylated graphene oxide. *Biomaterials* **2011,** 32, (33), 8555-8561.
107. Li, Y.; Lu, W.; Huang, Q.; Li, C.; Chen, W., Copper sulfide nanoparticles for photothermal ablation of tumor cells. *Nanomedicine* **2010,** 5, (8), 1161-1171.
108. Hessel, C. M.; Pattani, V. P.; Rasch, M.; Panthani, M. G.; Koo, B.; Tunnell, J. W.; Korgel, B. A., Copper selenide nanocrystals for photothermal therapy. *Nano Lett.* **2011,** 11, (6), 2560-2566.
109. Guo, L.; Yan, D. D.; Yang, D.; Li, Y.; Wang, X.; Zalewski, O.; Yan, B.; Lu, W., Combinatorial photothermal and immuno cancer therapy using chitosan-coated hollow copper sulfide nanoparticles. *ACS Nano* **2014,** 8, (6), 5670-5681.
110. Zha, Z.; Zhang, S.; Deng, Z.; Li, Y.; Li, C.; Dai, Z., Enzyme-responsive copper sulphide nanoparticles for combined photoacoustic imaging, tumor-selective chemotherapy and photothermal therapy. *Chem. Commun.* **2013,** 49, (33), 3455-3457.
111. Wang, S.; Chen, Y.; Li, X.; Gao, W.; Zhang, L.; Liu, J.; Zheng, Y.; Chen, H.; Shi, J., Injectable 2D

MoS_2-integrated drug delivering implant for highly efficient NIR-triggered synergistic tumor hyperthermia. *Adv. Mater.* **2015,** 27, (44), 7117-7122.
112. Yang, Y.; Fei, H.; Ruan, G.; Xiang, C.; Tour, J. M., Edge-oriented MoS_2 nanoporous films as flexible electrodes for hydrogen evolution reactions and supercapacitor devices. *Adv. Mater.* **2014,** 26, (48), 8163-8168.
113. Cheng, L.; Liu, J.; Gu, X.; Gong, H.; Shi, X.; Liu, T.; Wang, C.; Wang, X.; Liu, G.; Xing, H., PEGylated WS_2 nanosheets as a multifunctional theranostic agent for *in vivo* dual-modal CT/photoacoustic imaging guided photothermal therapy. *Adv. Mater.* **2014,** 26, (12), 1886-1893.
114. Yong, Y.; Cheng, X.; Bao, T.; Zu, M.; Yan, L.; Yin, W.; Ge, C.; Wang, D.; Gu, Z.; Zhao, Y., Tungsten sulfide quantum dots as multifunctional nanotheranostics for *in vivo* dual-modal image-guided photothermal/radiotherapy synergistic therapy. *ACS Nano* **2015,** 9, (12), 12451-12463.
115. Chen, W. R.; Adams, R. L.; Higgins, A. K.; Bartels, K. E.; Nordquist, R. E., Photothermal effects on murine mammary tumors using indocyanine green and an 808-nm diode laser: an *in vivo* efficacy study. *Cancer Lett.* **1996,** 98, (2), 169-173.
116. Zheng, X.; Xing, D.; Zhou, F.; Wu, B.; Chen, W. R., Indocyanine green-containing nanostructure as near infrared dual-functional targeting probes for optical imaging and photothermal therapy. *Mol. Pharmaceutics* **2011,** 8, (2), 447-456.
117. Yang, K.; Xu, H.; Cheng, L.; Sun, C.; Wang, J.; Liu, Z., *In vitro* and *In vivo* near-infrared photothermal therapy of cancer using polypyrrole organic nanoparticles. *Adv. Mater.* **2012,** 24, (41), 5586-5592.
118. Zha, Z.; Yue, X.; Ren, Q.; Dai, Z., Uniform polypyrrole nanoparticles with high photothermal conversion efficiency for photothermal ablation of cancer cells. *Adv. Mater.* **2013,** 25, (5), 777-782.
119. Huang, C.; Soenen, S. J.; Rejman, J.; Trekker, J.; Chengxun, L.; Lagae, L.; Ceelen, W.; Wilhelm, C.; Demeester, J.; De Smedt, S. C., Magnetic electrospun fibers for cancer therapy. *Adv. Funct. Mater.* **2012,** 22, (12), 2479-2486.
120. Blanco, E.; Shen, H.; Ferrari, M., Principles of nanoparticle design for overcoming biological barriers to drug delivery. *Nat. Biotechnol.* **2015,** 33, (9), 941-951.
121. Li, Z.; Huang, H.; Tang, S.; Li, Y.; Yu, X.-F.; Wang, H.; Li, P.; Sun, Z.; Zhang, H.; Liu, C., Small gold nanorods laden macrophages for enhanced tumor coverage in photothermal therapy. *Biomaterials* **2016,** 74, 144-154.
122. Choi, J.; Kim, H.-Y.; Ju, E. J.; Jung, J.; Park, J.; Chung, H.-K.; Lee, J. S.; Lee, J. S.; Park, H. J.; Song, S. Y., Use of macrophages to deliver therapeutic and imaging contrast agents to tumors. *Biomaterials* **2012,** 33, (16), 4195-4203.
123. Kang, S.; Bhang, S. H.; Hwang, S.; Yoon, J.-K.; Song, J.; Jang, H.-K.; Kim, S.; Kim, B.-S., Mesenchymal stem cells aggregate and deliver gold nanoparticles to tumors for photothermal therapy. *ACS Nano* **2015,** 9, (10), 9678-9690.
124. Mooney, R.; Roma, L.; Zhao, D.; Van Haute, D.; Garcia, E.; Kim, S. U.; Annala, A. J.; Aboody, K. S.; Berlin, J. M., Neural stem cell-mediated intratumoral delivery of gold nanorods improves photothermal therapy. *ACS Nano* **2014,** 8, (12), 12450-12460.
125. Choi, M.-R.; Stanton-Maxey, K. J.; Stanley, J. K.; Levin, C. S.; Bardhan, R.; Akin, D.; Badve, S.; Sturgis, J.; Robinson, J. P.; Bashir, R., A cellular Trojan Horse for delivery of therapeutic nanoparticles into tumors. *Nano Lett.* **2007,** 7, (12), 3759-3765.
126. Xing, R.; Liu, K.; Jiao, T.; Zhang, N.; Ma, K.; Zhang, R.; Zou, Q.; Ma, G.; Yan, X., An injectable self-assembling collagen–gold hybrid hydrogel for combinatorial antitumor photothermal/photodynamic therapy. *Adv. Mater.* **2016,** 28, (19), 3669-3676.

127. Hsiao, C.-W.; Chuang, E.-Y.; Chen, H.-L.; Wan, D.; Korupalli, C.; Liao, Z.-X.; Chiu, Y.-L.; Chia, W.-T.; Lin, K.-J.; Sung, H.-W., Photothermal tumor ablation in mice with repeated therapy sessions using NIR-absorbing micellar hydrogels formed in situ. *Biomaterials* **2015,** 56, 26-35.
128. Ma, H.; Jiang, C.; Zhai, D.; Luo, Y.; Chen, Y.; Lv, F.; Yi, Z.; Deng, Y.; Wang, J.; Chang, J., A bifunctional biomaterial with photothermal effect for tumor therapy and bone regeneration. *Adv. Funct. Mater.* **2016,** 26, (8), 1197-1208.
129. Ma, H.; Luo, J.; Sun, Z.; Xia, L.; Shi, M.; Liu, M.; Chang, J.; Wu, C., 3D printing of biomaterials with mussel-inspired nanostructures for tumor therapy and tissue regeneration. *Biomaterials* **2016,** 111, 138-148.
130. Chen, G.; Ushida, T.; Tateishi, T., Scaffold design for tissue engineering. *Macromol. Biosci.* **2002,** 2, (2), 67-77.
131. Hollister, S. J., Porous scaffold design for tissue engineering. *Nat. Mater.* **2005,** 4, (7), 518-524.
132. Butler, D. L.; Goldstein, S. A.; Guilak, F., Functional tissue engineering: the role of biomechanics. *J. Biomech. Eng.* **2000,** 122, (6), 570-575.
133. Ikada, Y.; Tsuji, H., Biodegradable polyesters for medical and ecological applications. *Macromol. Rapid Commun.* **2000,** 21, (3), 117-132.
134. Hsu, S. h.; Chang, S. H.; Yen, H. J.; Whu, S. W.; Tsai, C. L.; Chen, D. C., Evaluation of biodegradable polyesters modified by type II collagen and arg-gly-asp as tissue engineering scaffolding materials for cartilage regeneration. *Artif. Organs* **2006,** 30, (1), 42-55.
135. Agrawal, C.; Ray, R. B., Biodegradable polymeric scaffolds for musculoskeletal tissue engineering. *J. Biomed. Mater. Res.* **2001,** 55, (2), 141-150.
136. Kumar, N.; Langer, R. S.; Domb, A. J., Polyanhydrides: an overview. *Adv. Drug Delivery Rev.* **2002,** 54, (7), 889-910.
137. Eyre, D. R., Collagen: molecular diversity in the body's protein scaffold. *Science* **1980,** 207, (4437), 1315-1322.
138. Mao, J.; Zhao, L.; de Yao, K.; Shang, Q.; Yang, G.; Cao, Y., Study of novel chitosan-gelatin artificial skin in vitro. *J. Biomed. Mater. Res. A* **2003,** 64, (2), 301-308.
139. Chong, E.; Phan, T.; Lim, I.; Zhang, Y.; Bay, B.; Ramakrishna, S.; Lim, C., Evaluation of electrospun PCL/gelatin nanofibrous scaffold for wound healing and layered dermal reconstitution. *Acta Biomater.* **2007,** 3, (3), 321-330.
140. Liu, X.; Smith, L. A.; Hu, J.; Ma, P. X., Biomimetic nanofibrous gelatin/apatite composite scaffolds for bone tissue engineering. *Biomaterials* **2009,** 30, (12), 2252-2258.
141. Woodard, J. R.; Hilldore, A. J.; Lan, S. K.; Park, C.; Morgan, A. W.; Eurell, J. A. C.; Clark, S. G.; Wheeler, M. B.; Jamison, R. D.; Johnson, A. J. W., The mechanical properties and osteoconductivity of hydroxyapatite bone scaffolds with multi-scale porosity. *Biomaterials* **2007,** 28, (1), 45-54.
142. Chen, S.; Zhang, Q.; Nakamoto, T.; Kawazoe, N.; Chen, G., Gelatin Scaffolds with Controlled Pore Structure and Mechanical Property for Cartilage Tissue Engineering. *Tissue Eng Part C Methods* **2016,** 22, (3), 189-198.
143. Lien, S.-M.; Ko, L.-Y.; Huang, T.-J., Effect of pore size on ECM secretion and cell growth in gelatin scaffold for articular cartilage tissue engineering. *Acta Biomater.* **2009,** 5, (2), 670-679.
144. Felt, O.; Buri, P.; Gurny, R., Chitosan: a unique polysaccharide for drug delivery. *Drug Dev. Ind. Pharm.* **1998,** 24, (11), 979-993.
145. Moreau, J. L.; Xu, H. H., Mesenchymal stem cell proliferation and differentiation on an injectable calcium phosphate–chitosan composite scaffold. *Biomaterials* **2009,** 30, (14), 2675-2682.
146. Heim, M.; Römer, L.; Scheibel, T., Hierarchical structures made of proteins. The complex architecture

of spider webs and their constituent silk proteins. *Chem. Soc. Rev.* **2010,** 39, (1), 156-164.
147. Fan, H.; Liu, H.; Toh, S. L.; Goh, J. C., Enhanced differentiation of mesenchymal stem cells co-cultured with ligament fibroblasts on gelatin/silk fibroin hybrid scaffold. *Biomaterials* **2008,** 29, (8), 1017-1027.
148. Sun, H.; Wu, C.; Dai, K.; Chang, J.; Tang, T., Proliferation and osteoblastic differentiation of human bone marrow-derived stromal cells on akermanite-bioactive ceramics. *Biomaterials* **2006,** 27, (33), 5651-5657.
149. Croisier, F.; Jérôme, C., Chitosan-based biomaterials for tissue engineering. *Eur. Polym. J.* **2013,** 49, (4), 780-792.
150. Leong, K.; Cheah, C.; Chua, C., Solid freeform fabrication of three-dimensional scaffolds for engineering replacement tissues and organs. *Biomaterials* **2003,** 24, (13), 2363-2378.
151. Chan, B.; Leong, K., Scaffolding in tissue engineering: general approaches and tissue-specific considerations. *Eur. Spine J.* **2008,** 17, (4), 467-479.
152. Yoon, J. J.; Park, T. G., Degradation behaviors of biodegradable macroporous scaffolds prepared by gas foaming of effervescent salts. *: J Biomed Mater Res* **2001,** 55, (3), 401-408.
153. Kim, U.-J.; Park, J.; Kim, H. J.; Wada, M.; Kaplan, D. L., Three-dimensional aqueous-derived biomaterial scaffolds from silk fibroin. *Biomaterials* **2005,** 26, (15), 2775-2785.
154. Wu, X.; Liu, Y.; Li, X.; Wen, P.; Zhang, Y.; Long, Y.; Wang, X.; Guo, Y.; Xing, F.; Gao, J., Preparation of aligned porous gelatin scaffolds by unidirectional freeze-drying method. *Acta Biomater.* **2010,** 6, (3), 1167-1177.
155. Zhang, Q.; Lu, H.; Kawazoe, N.; Chen, G., Pore size effect of collagen scaffolds on cartilage regeneration. *Acta Biomater.* **2014,** 10, (5), 2005-2013.
156. Zhang, Q.; Lu, H.; Kawazoe, N.; Chen, G., Preparation of collagen porous scaffolds with a gradient pore size structure using ice particulates. *Mater. Lett.* **2013,** 107, 280-283.
151. B. Chan and K. Leong, *Eur. Spine J* 2008, **17**, 467-479.
152. J. J. Yoon and T. G. Park, *J.Biomed.Mater. Res.* 2001, **55**, 401-408.
153. U.-J. Kim, J. Park, H. J. Kim, M. Wada and D. L. Kaplan, *Biomaterials*, 2005, **26**, 2775-2785.
154. X. Wu, Y. Liu, X. Li, P. Wen, Y. Zhang, Y. Long, X. Wang, Y. Guo, F. Xing and J. Gao, *Acta Biomater.*, 2010, **6**, 1167-1177.
155. Q. Zhang, H. Lu, N. Kawazoe and G. Chen, *Acta Biomater.*, 2014, **10**, 2005-2013.
156. Q. Zhang, H. Lu, N. Kawazoe and G. Chen, *Mater. Lett.*, 2013, **107**, 280-283.

Chapter 2

Preparation of gelatin/Fe_3O_4 composite scaffolds for enhanced and repeatable cancer cell ablation

2.1 Summary

Various nanomaterials have been extensively investigated for photothermal ablation of cancer cells because of their high photothermal conversion efficiency. However, the poor targeting specificity and low repeated heating efficiency of nanomaterials restrict their applications in clinic. In this work, porous gelatin/iron oxide (Gel/Fe_3O_4) composite scaffolds were prepared by a facile ice particulates templating method for efficient and repeatable cancer cells ablation. Gel/Fe_3O_4 composite scaffolds showed controlled porous structure consisting of large pores and interconnecting small pores. The strong absorption in the near-infrared (NIR) region enabled the Gel/Fe_3O_4 composite scaffolds to elevate local temperature quickly under NIR laser irradiation. The composite scaffolds allowed cell adhesion and proliferation showing good biocompatibility. Cancer cells entrapped in the scaffolds could be efficiently killed during laser irradiation. Moreover, the therapeutic efficacy of Gel/Fe_3O_4 composite scaffolds could be enhanced by repeated laser irradiation treatment, which is important for clinical application because of the resistant and recurrent nature of cancer. The results indicated the porous Gel/Fe_3O_4 composite scaffold had good biocompatibility and excellent cancer cells ablation efficacy, which may provide an attractive way to use porous scaffolds for cancer therapy application.

2.2 Introduction

Cancer has become one of the biggest threats to human health. According to the World Health Organization (WHO), each year about 8 million people die of cancer all over the world. Up to now, surgical resection, chemotherapy and radiotherapy are the most commonly used methods in the clinical field to treat cancer. However, these methods still face some challenges such as cancer recurrence and side effects.[1-4] In recent years, photothermal therapy (PTT) as a novel treatment for cancer has attracted increasing attention.[5-7] PTT uses the photothermal conversion agents to absorb near infrared (NIR) light and convert it to heat, thereby leading to the destruction of cancer cells.[8-10]

Many nanomaterials can be used as PTT agents, such as iron oxide (Fe_3O_4) nanoparticles,[11-16] carbon

nanotubes,[17-19] graphene[20-22] and gold-based nanomaterials.[23-25] Among all of these PTT agents, Fe_3O_4 nanoparticles have aroused much attention due to their unique properties and good biocompatibility.[26-28] Beneficial from the strong NIR absorption and high photothermal conversion efficiency, Fe_3O_4 nanoparticles can raise up the local temperature quickly to kill cancer cells with exposure to the NIR laser.[11, 13] Moreover, high magnetic susceptibility of Fe_3O_4 nanoparticles enables their non-invasive manipulation in living body by external magnetic fields.[29, 30] However, applications of Fe_3O_4 nanoparticles for cancer diagnosis and therapy still have some challenges. For example, the accumulation of Fe_3O_4 nanoparticles into tumor sites is still limited although many targeting strategies have been applied, such as magnetic targeting and molecular targeting.[12, 31] After the intravenous injection, most of Fe_3O_4 nanoparticles are rapidly cleared by mononuclear phagocyte system and preferentially accumulated in some organs such as kidney, liver and spleen rather than the tumor site.[32] Furthermore, if these nanoparticles are locally injected into tumor site, their small sizes make them easily leaked from the tumor site.[33] All of these issues lower the photothermal efficacy of nanoparticles. Therefore, it is essential to develop a Fe_3O_4-based PTT material with excellent local photothermal efficacy.

Recently, a strategy that immobilizes PTT agents on implanted substrate has emerged for effective photothermal therapy application.[32, 34-39] The advantage of immobilized PTT agents is that they can be efficiently localized to the tumor site.[36, 40-42] More importantly, they can be easily retained at the tumor site for relatively longer time than free nanoparticles and thus realize repeated local heating without losing photothermal efficiency for cancer cells ablation, which is particularly critical for treating the recurrence of cancer.[33]

In this study, composite porous scaffolds of Fe_3O_4 and gelatin (Gel) were prepared by using ice particulates as porogen for localized photothermal ablation of cancer cells. Ice particulates were used to control the pore structure and increased pore interconnectivity, which were important for cancer cells entrapment. The Gel/Fe_3O_4 composite scaffolds showed an obvious absorption of NIR light and the local temperature could be elevated quickly under NIR laser irradiation. *In vitro* studies showed the Gel/Fe_3O_4 composite scaffolds had good biocompatibility and excellent photothermal therapeutic efficacy. Furthermore, the cancer cell killing efficiency of Gel/Fe_3O_4 scaffolds could be improved by repeated irradiation.

2.3 Materials and methods

2.3.1 Materials

Iron (III) chloride hexahydrate ($FeCl_3$•$6H_2O$, 97%), sodium sulfite (Na_2SO_3, 98%), 2-(Nmorpholino) ethanesulfonic acid (MES), Eagle's Minimun Essential Medium (EMEM), penicillin, streptomycin trypsin/EDTA and DNA quantification kit were purchased from Sigma-Aldrich (St. Louis, MO, USA). Trisodium citrate dihydrate ($C_6H_5Na_3O_7 \cdot 2H_2O$,) 25 wt% ammonia solution, acetic acid and N-hydroxysuccinimide (NHS) were purchased from Wako Pure Industries, Ltd (Tokyo, Japan). Porcine derived gelatin was provided by Nitta Gelatin (Osaka, Japan). 1-ethyl-3-(3-dimethylaminopropyl) carbodiimide (EDC) was purchased from Peptide Institute, Inc. (Osaka, Japan). WST-1 reagent was obtained from Roche Molecular Biochemicals (Mannheim, Germany). A cellstain live-dead double staining kit was purchased from Dojindo Laboratories (Kumamoto, Japan). All the chemicals and materials were used as received without further purification. The water in all experiments was purified using a Q-POD Milli-Q water purification system (Millipore Corp., Billerica, MA, USA) with a resistivity of 18.2 MΩ•cm.

2.3.2 Synthesis of the Fe_3O_4 nanoparticles

Fe_3O_4 nanoparticles were synthesized according to a previously reported method with some modifications.[43] Briefly, a Na_2SO_3 (0.4 g in 20 mL water) solution was mixed with a $FeCl_3 \cdot 6H_2O$ (2.6 g in 40 mL water) solution under nitrogen atmosphere protection. Subsequently, the mixture solution was transferred into a 75 ^oC water bath, followed by the addition of 4 mL ammonia solution (25 wt%) and 10 mL citrate solution (0.1 g/mL). After reaction for 40 min, the solution was cooled down to room temperature and then the formed Fe_3O_4 nanoparticles were collected by magnetic separation, washed four times with water and finally dispersed in water and stored at 4 ^oC for further use.

2.3.3 Preparation of Gel/ Fe_3O_4 composite scaffolds

Gel/Fe_3O_4 composite scaffolds were prepared by using pre-prepared ice particulates as a porogen material.[44] Briefly, an 8 wt% Gel solution was firstly prepared by dissolving appropriate amount of Gel into an acetic acid solution. The Fe_3O_4 nanoparticle suspension solution of different concentration was mixed with the same volume of Gel acetic acid solution under mechanical shaking. After that, the mixture solutions (containing 4 wt% Gel) were sonicated for 30 min at room temperature and then put at -4 ^oC for 40 min for temperature balance.

Ice particulates were prepared by spraying pure water into liquid nitrogen. The ice particulates with diameters in a range of 425 ~ 500 μm were obtained by sieving the formed ice particulates with two sieves having mesh pores of 425 and 500 μm. The ice particulates were then transferred into a cooled glass bottle and kept at -4 ^oC for 2 h for temperature balance. After that, the ice particulates were mixed thoroughly with the cooled Gel-Fe_3O_4 mixture solution at a weight/volume ratio of 7:3 (g/mL) at -4 ^oC. Subsequently, the mixture of Gel-Fe_3O_4 solution and ice particulates was poured into a cooled silicone frame to control dimension of the composite scaffold. The entire set was first pre-frozen at -20 ^oC for 12 h and then transferred to -80 ^oC for 4 h for further frozing. Finally, the entire set was freeze-dried for 3 d.

After freeze-drying, the formed composite scaffolds were washed with ethanol (99.5%) for 10 times to remove residual acetic acid. After washing with ethanol, the composite scaffolds were cross-linked with EDC and NHS ethanol aqueous solution. To protect the dissolution of collagen and maximize the cross-linking effect, three mixture solvents with a decreasing ethanol concentration (ethanol/water=95/5, 90/10, 85/15, v/v) were used to prepare the crosslinking solutions, which contained 50 mM EDC, 20 mM NHS and 0.1 (wt/v)% MES. The Gel/Fe_3O_4 composite scaffolds were crosslinked sequentially by the three crosslinking solutions of a decreasing ethanol concentration (from 95/5, 90/10, 85/15) for every 8 h in each solution. After cross-linking, the composite scaffolds were rinsed with water for 6 times and then further treated with 0.1 M glycine for 6 h. Finally, the scaffolds were washed with water and freeze-dried for 2 d to get the final Gel/Fe_3O_4 composite scaffolds. The porous Gel scaffold was also prepared by the same method without adding Fe_3O_4 nanoparticles. The Gel/Fe_3O_4 composite scaffolds prepared with a weight ratio of Fe_3O_4 nanoparticles to dry composite scaffold of 1 wt%, 5 wt%, 10 wt% and 15 wt% were denoted as Gel/Fe_3O_4-1, Gel/Fe_3O_4-5, Gel/Fe_3O_4-10 and Gel/Fe_3O_4-15, respectively.

2.3.4 Characterization of Fe_3O_4 nanoparticles and Gel/Fe_3O_4 scaffolds

Size and morphology of as-synthesized Fe_3O_4 nanoparticles were investigated by transmission electron microscopy (TEM, JEOL 2011F, Japan). The Fe_3O_4 nanoparticle size was determined by measuring more

than 100 nanoparticles in different TEM images using an ImageJ software. Dynamic light scattering (DLS) was used to measure the hydrodynamic size of the Fe_3O_4 nanoparticles. X-ray powder diffraction (XRD) analysis was carried out with a Rigaku X-ray diffractometer operating with Cu Kα radiation (λ = 0.1541 nm) at a scanning rate of 3 ^{o}/min to investigate the crystalline structure of Fe_3O_4 nanoparticles, Gel scaffolds and Gel/Fe_3O_4 composite scaffolds. The pore structures of Gel scaffolds and Gel/Fe_3O_4 composite scaffolds were observed by a scanning electron microscope (SEM, Hitachi S-4800, Japan) and the pore size was measured from SEM images by an Image J software. Four images of each scaffold and at least 20 pores per image were used for the pore size analysis. All the scaffolds were cut into cylinder shape (Φ6.0 × H5.0 mm) to measure the porosity of Gel scaffolds and Gel/Fe_3O_4 composite scaffolds (n = 3). And the porosity was calculated according to the following formula: porosity = $V_{pore}/V = ((W_2 - W_1)/\rho/V) \times 100\%$, where V_{pore} is the volume of pores, V is the total volume of the scaffold, W_1 is the dry weight of the scaffold, W_2 is the weight of scaffold with water and ρ is the density of water. [45, 46] The volume of the scaffolds was calculated from the scaffold dimension. The quantity of Fe_3O_4 nanoparticles incorporated in the composite scaffolds was determined *via* thermogravimetric analysis (TGA, Seiko Exstar 6000 TG/DTA 6200 thermal gravimetric analyzer, Tokyo, Japan). UV-visible absorption spectra of the samples were recorded using a UV-2600 UV-visible spectrophotometer (Shimadzu Corp., Japan).

2.3.5 Photothermal effect of the Gel/Fe_3O_4 composite scaffolds

To investigate the photothermal effect of the Gel/Fe_3O_4 composite scaffolds, samples filled with culture medium (EMEM) were exposed to a NIR laser (805 nm, Thorlabs Inc., USA) with a power density of 1.6 W cm^{-2} for 180 s. During the irradiation, a digital thermometer (AS ONE Corp., Japan) was used to measure the temperature of the samples every 10 s.

2.3.6 Cell culture in the scaffolds

HeLa cells (Human cervical carcinoma cell line) were cultured in a regular EMEM medium supplemented with 10% FBS, penicillin (100 U mL^{-1}) and streptomycin (100 μg mL^{-1}) in 5% CO_2 incubator at 37 ^{o}C in a humidified environment. The cells were seeded in 75 cm^2 tissue culture flasks and passaged using a 0.25% trypsin-EDTA solution after reaching confluence.

The Gel scaffolds and Gel/Fe_3O_4 composite scaffolds were cut into cubes (5 × 3 × 1 mm^3), sterilized with 70% ethanol, washed with PBS for 5 times and immersed into culture medium at 37 ^{o}C for 6 h. After removing the culture medium from the scaffolds, 1×10^5 HeLa cells were seeded into each scaffolds. After 5 h of incubation, the cell/scaffold constructs were transferred into 6-well plates and cultured in medium at 37 ^{o}C and 5% CO_2 incubator.

2.3.7 Cell adhesion and proliferation in the composite scaffolds

The adhesion and proliferation of HeLa cells were measured to determine the biocompatibility of Gel scaffolds and Gel/Fe_3O_4 composite scaffolds. After being cultured for 1 d, cell/scaffold constructs were fixed with 2.5% glutaraldehyde at room temperature for 2 h. The fixed constructs were washed with MilliQ water thoroughly and freeze-dried. SEM was used to observe the cell adhesion and distribution in the Gel scaffolds and Gel/Fe_3O_4 composite scaffolds. DNA amount was used to determine cell proliferation in the Gel scaffolds and Gel/Fe_3O_4 composite scaffolds. After being cultured for 1, 3 and 7 d, the cell/scaffold

constructs were harvested, washed with water, freeze-dried and digested with papain solution. DNA content in the Gel and Gel/Fe_3O_4 composite scaffolds was measured with Hoechst 33258 dye and quantified by a spectrofluorometer (FP-6500, JASCO, Japan).[47] Every three samples were used for the measurement to calculate the average and standard deviation.

2.3.8 *In vitro* photothermal ablation of HeLa cells

In vitro photothermal ablation of cancer cells was carries out by NIR laser irradiation (805 nm, Thorlabs Inc., USA). The power density of laser was adjusted to 1.6 W/cm^2. After 24 h of culture, cell/scaffold constructs were divided into irradiation groups (with laser irradiation) and non-irradiation groups (without laser irradiation). For the irradiation group, cell/scaffold constructs were taken out from the culture dishes and exposed to the NIR laser for 3 min. The samples without laser irradiation were also taken out from the dishes for 3 min to exclude environmental effects on cell death. After the laser irradiation, all of the cell/scaffold constructs were continuously cultured for another 5 h. Cell viability were measured by a WST-1 assay. The absorbance at 440 nm was measured by a microplate reader (Benchmark Plus, Bio-Rad, Hercules, CA, USA). In order to check the repeated photothermal effect of Gel/Fe_3O_4 scaffolds during repeated NIR laser irradiation, the cell/scaffold constructs were exposed to NIR laser for different irradiation cycles. After irradiated for 3 min (1 cycle), the cell/scaffold constructs were cooled down to the room temperature and then were irradiated for another 3 min (2 cycles). This process was repeated for 3 times. The cell viability was evaluated using WST-1 assay after each irradiation cycle. Every three samples were used for the measurement to calculate the average and standard deviation.

Live/dead staining with a cellstain live-dead double staining kit was used to confirm the live and dead cells in the scaffolds after NIR irradiation for different cycles or without NIR irradiation. The cell/scaffold constructs were washed twice with PBS and incubated in serum-free EMEM medium containing calcein AM and propidium iodide (PI) for 15 min. And then, the samples were observed under a fluorescent microscope (Olympus, Japan).

2.3.9 Statistical analysis

All of the data were presented as mean ± standard deviation (SD). Statistical analysis was performed using a one-way analysis of variance with Tukey's post hoc test for multiple comparisons. A value of $p < 0.05$ was considered to indicate a statistically significant difference.

2.4 Results and discussion

2.4.1 Morphology of Fe_3O_4 nanoparticles

The morphology and size distribution of the as-prepared Fe_3O_4 nanoparticles are shown in Fig. 2.1 (a-b). The Fe_3O_4 nanoparticles possessed a spherical or quasi-spherical shape and a shape size distribution. A small amount of nanoparticles aggregated which might be caused by the magnetic assembly. The average diameter of single Fe_3O_4 nanoparticles was 18.4 ± 2.5 nm. The hydrodynamic size of the Fe_3O_4 nanoparticles dispersed in water was measured to be 164.1 ± 2.5 nm by dynamic light scattering (DLS). The hydrodynamic size of

the nanoparticles was much larger than that measured from TEM. This may be due to the aggregation of Fe_3O_4 nanoparticles in water. The Fe_3O_4 nanoparticles would easily assemble in aqueous solution

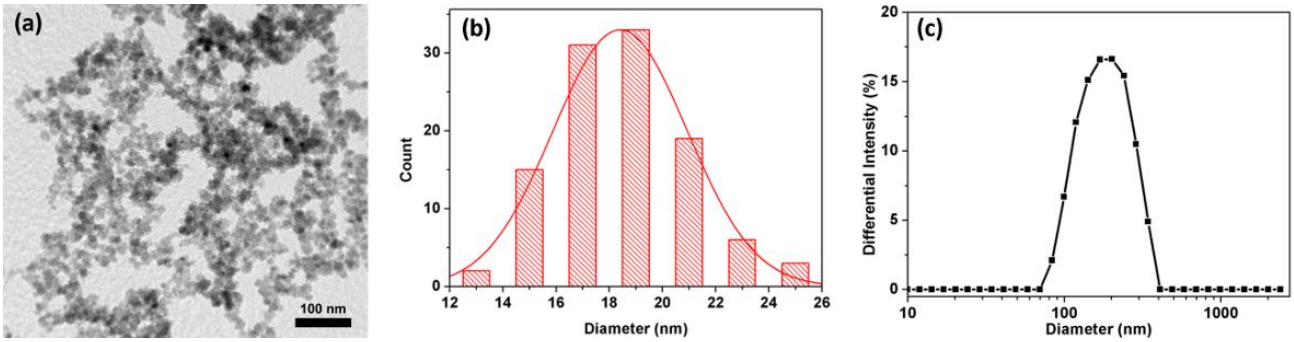

Fig. 2.1. (a) TEM image of Fe_3O_4 nanoparticles. (b) Diameter histogram of Fe_3O_4 nanoparticles measured from TEM images. (c) Hydrodynamic size of Fe_3O_4 nanoparticles measured by DLS.

2.4.2 Characterization of Gel and the Gel/Fe_3O_4 composite scaffolds

Fig.2.2 shows the gross appearance and morphology of Gel scaffolds and Gel/Fe_3O_4 composite scaffolds. The color of the composite scaffolds turned from white into brown after incorporation of Fe_3O_4 nanoparticles. With the increased amount of Fe_3O_4 nanoparticles, the color became darker, suggesting an enhanced light absorption property. SEM images showed that the pore structure of the scaffolds with different amount of Fe_3O_4 nanoparticles did not show obvious difference. All the scaffolds prepared with ice particulates had spherical large pores. The large pores were distributed homogeneously throughout the scaffolds and their size was almost equal to the size of added ice particulates (Table 2.1). Moreover, during the pre-freezing process (-20 ^{o}C, 12 h), many small ice crystals were in-situ formed around the added large ice particulates and they could also serve as porogen, thus inducing the formation of many small pores between the spherical large pores (Fig. 2.2(b)). The small pores having average size around 100 μm (Table 2.1) made the scaffolds well interconnected and the porosity of all the scaffolds was higher than 98.5 % (Table 2.1). The high porosity and good interconnectivity should be beneficial for the penetration and spatial distribution of cells. The images at a high magnification showed that the pore walls of Gel scaffold possessed a smooth surface (Fig. 2.2(c)). The surface of the pore walls in Gel/Fe_3O_4 composite scaffolds became rough and the Fe_3O_4 nanoparticles were shown to be evenly distributed on the pore walls. As the amount of Fe_3O_4 nanoparticles increased, Fe_3O_4 nanoparticles on the pore walls became more evident. The size of the Fe_3O_4 nanoparticles on pore walls was about 200 nm, which was much larger than that of Fe_3O_4 nanoparticles size measured from TEM but close to the hydrodynamic size. The result indicated the Fe_3O_4 nanoparticles were partially aggregated during scaffold preparation.

The XRD patterns of Gel scaffolds and Gel/Fe_3O_4 composite scaffolds are shown in Fig. 2.3. As a reference, the pure Fe_3O_4 nanoparticles were also analyzed, in which typical peaks of Fe_3O_4 (JCPDS 19-0629) were shown.[48] Gel scaffolds exhibited a broad peak in the range of 15 ~ 30°, which was a typical characteristic for pure gelatin.[49, 50] From the XRD patterns of all the Gel/Fe_3O_4 scaffolds, the characteristic peaks of Fe_3O_4 were detected. The results confirmed the presence of Fe_3O_4 in the Gel/Fe_3O_4 composite scaffolds.

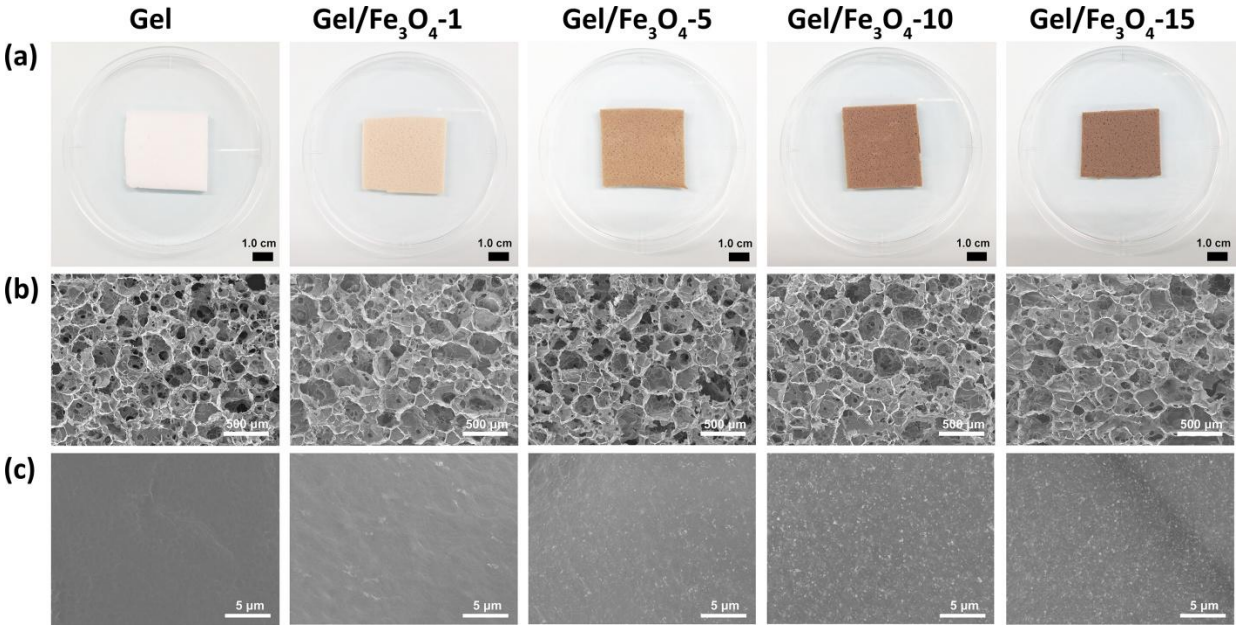

Fig. 2.2. (a) Gross appearance and (b) SEM images of Gel scaffolds and Gel/Fe_3O_4 composite scaffolds. (c) SEM images of the corresponding scaffolds showing the morphology of pore walls at a high magnification.

Table 2.1. Pore size (large pores and small pores) and porosity of Gel and Gel/Fe_3O_4 composite scaffolds. Data represent mean ± SD.

Sample	Gel	Gel/Fe_3O_4-1	Gel/Fe_3O_4-5	Gel/Fe_3O_4-10	Gel/Fe_3O_4-15
Large pores (μm)	458 ± 41	448 ± 36	441 ± 34	455 ± 27	453 ± 31
Small pores (μm)	107 ± 16	95 ± 14	99 ± 14	99 ± 13	101 ± 14
Porosity (%)	98.7 ± 0.5	98.9 ± 0.6	99.1 ± 0.2	98.7 ± 0.2	98.5 ± 0.3

TGA analysis was used to determine the quantity of Fe_3O_4 in the scaffolds. As shown in Fig. 2.4, the Fe_3O_4 nanoparticles showed a slight weight loss, which was probably due to the thermal-degradation of the the surface coated citrate on the nanoparticles that was remained during preparation of nanoparticles. The typical single mass-loss step of Gel and Gel/Fe_3O_4 scaffolds was located at 300 ~ 500 ^oC. It was attributed to the degradation of Gel fibers including depolymerization, dehydration and decomposition followed by formation of a charred residue.[50] Based on the residual mass of the composite scaffolds, the amount of Fe_3O_4 in the Gel/Fe_3O_4-1, Gel/Fe_3O_4-5, Gel/Fe_3O_4-10 and Gel/Fe_3O_4-15 porous scaffolds was 0.8 ± 0.5%, 6.8 ± 0.8%, 13.7 ± 0.6% and 18.7 ± 1.3%, respectively. The amount of incorporated Fe_3O_4 nanoparticles was almost the same as the added amount during scaffold preparation.

The UV-Vis absorption spectra were measured to investigate the absorption properties of the Gel scaffolds and Gel/Fe_3O_4 composite scaffolds in near-infrared (NIR) region (Fig. 2.5). The pure Gel scaffolds presented almost no absorption of NIR light. In contrast, after incorporating with Fe_3O_4, all the Gel/Fe_3O_4 scaffolds showed a broad and continuous absorption spectrum in the NIR region, which was well consistent with previous reports.[11, 12] Furthermore, the NIR absorption increased with the increasing amount of Fe_3O_4 nanoparticles. The obvious NIR absorption of Gel/Fe_3O_4 composite scaffolds suggested their potential for

photothermal therapy applications.

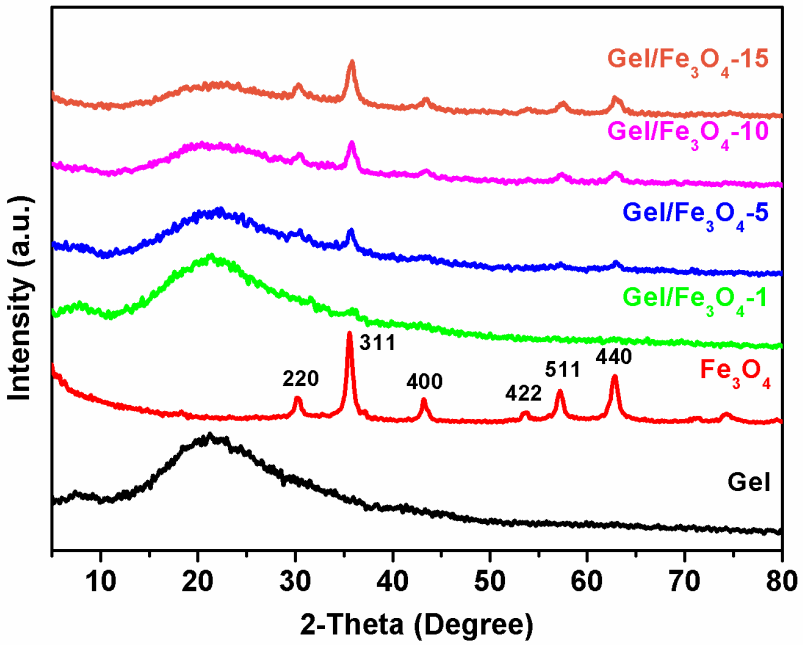

Fig. 2.3. XRD patterns of the Gel, Gel/Fe_3O_4-1, Gel/Fe_3O_4-5, Gel/Fe_3O_4-10 and Gel/Fe_3O_4-15 composite scaffolds. Pure Fe_3O_4 nanoparticles were also analysed for comparison.

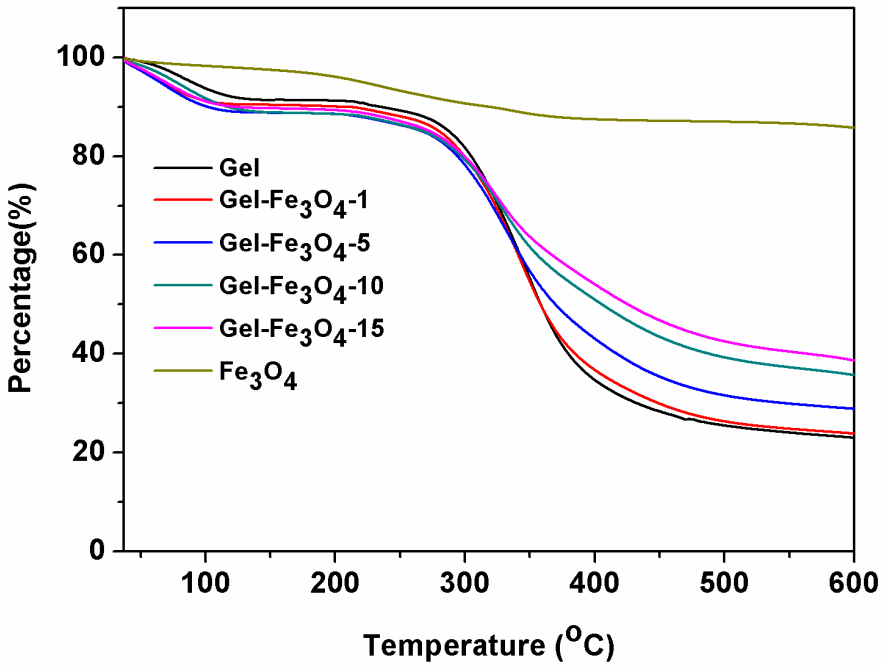

Fig. 2.4. TG analysis of the Gel, Gel/Fe_3O_4-1, Gel/Fe_3O_4-5, Gel/Fe_3O_4-10 and Gel/Fe_3O_4-15 composite scaffolds. Pure Fe_3O_4 nanoparticles were also analysed for comparison.

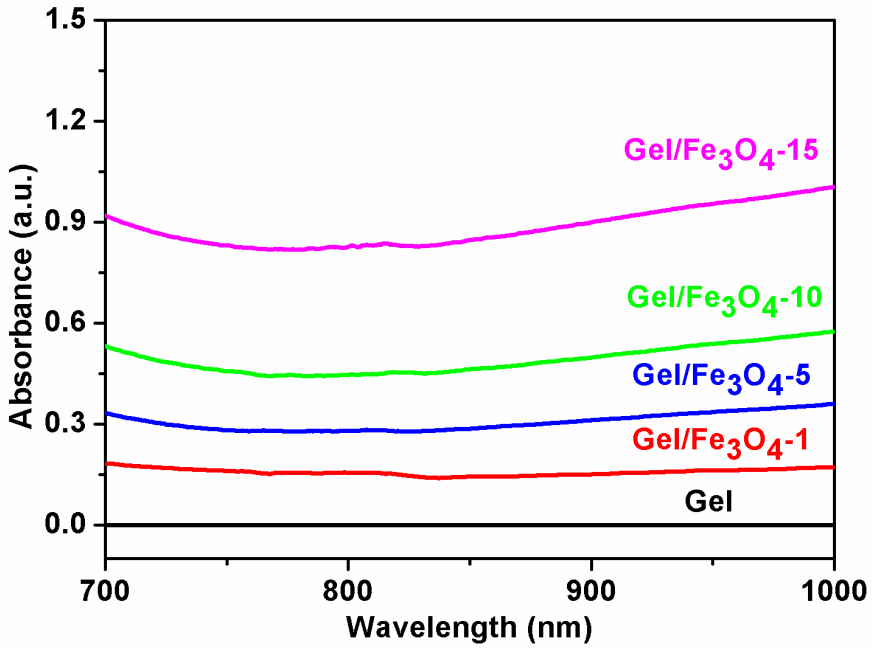

Fig. 2.5. UV-Vis absorption spectra of the Gel, Gel/Fe_3O_4-1, Gel/Fe_3O_4-5, Gel/Fe_3O_4-10 and Gel/Fe_3O_4-15 composite scaffolds.

2.4.3 Photothermal conversion efficiency of the Gel/Fe_3O_4 composite scaffolds

The photothermal conversion effect was studied by exposing scaffolds (filled with culture medium) to an 805 nm laser (Fig. 2.6). The temperature of the Gel/Fe_3O_4 composite scaffolds increased rapidly under the laser irradiation. In contrast, the pure Gel scaffolds exhibited slight heating under the identical condition. Moreover, higher content of Fe_3O_4 nanoparticles in the composite scaffolds resulted in higher temperature rise (Fig. 2.6a). The temperature increase was 9.3 ±0.3 °C, 18.4 ±0.3 °C, 21.2 ±0.9 °C and 26.1 ±0.4 °C for

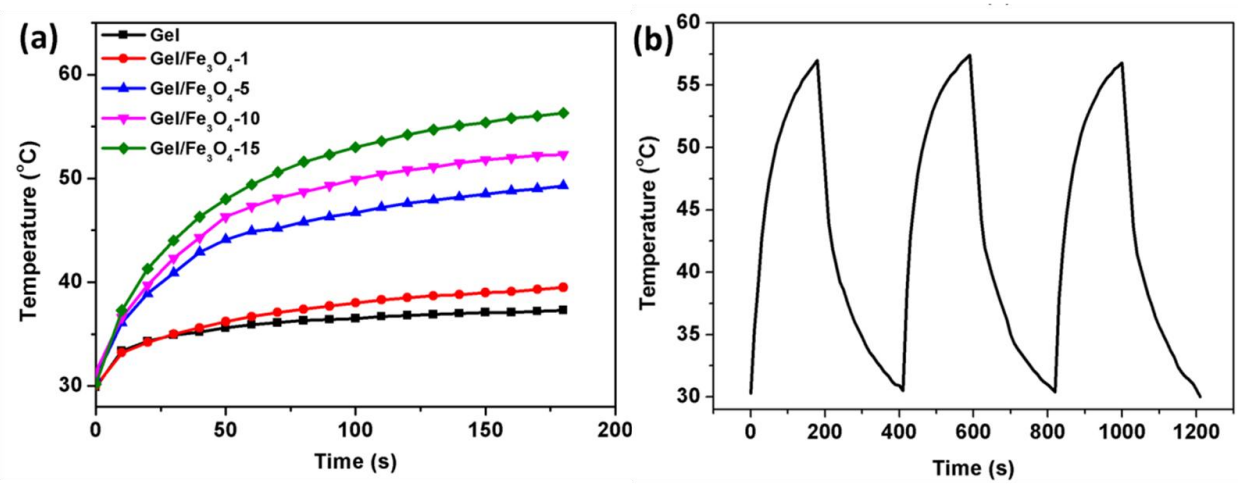

Fig. 2.6. (a) Temperature-time curve for the Gel scaffolds and Gel/Fe_3O_4 composite scaffolds under NIR irradiation, (b) Elevated temperature profile of Gel/Fe_3O_4-15 composite scaffolds over three laser on-off cycles.

Gel/Fe_3O_4-1, Gel/Fe_3O_4-5, Gel/Fe_3O_4-10 and Gel/Fe_3O_4-15 scaffolds, respectively. To examine the photostability of Gel/Fe_3O_4 composite scaffolds, Gel/Fe_3O_4-15 scaffolds were irradiated by laser for different cycles. As shown in Fig. 2.6b, no significant change in the elevated temperature profiles was observed throughout the three cycles of NIR laser irradiation, which suggested that the Gel/Fe_3O_4-15 scaffolds possessed a good photostability. The results suggested that the Gel/Fe_3O_4 porous scaffolds could rapidly and efficiently convert NIR energy into thermal energy. More importantly, a significant advantage of these scaffolds for cancer therapy was their capability for repeatable photo-heating treatment without losing the heating efficiency.

2.4.4 Cell adhesion and proliferation in the Gel and Gel/Fe_3O_4 composite scaffolds

The biocompatibility of Gel/Fe_3O_4 scaffolds was evaluated by examination of adhesion and proliferation of HeLa cells in the scaffolds. HeLa cells were seeded and cultured in the Gel and Gel/Fe_3O_4 scaffolds. After culture for 1 d, cell adhesion and spatial distribution were evaluated by SEM. After cultured

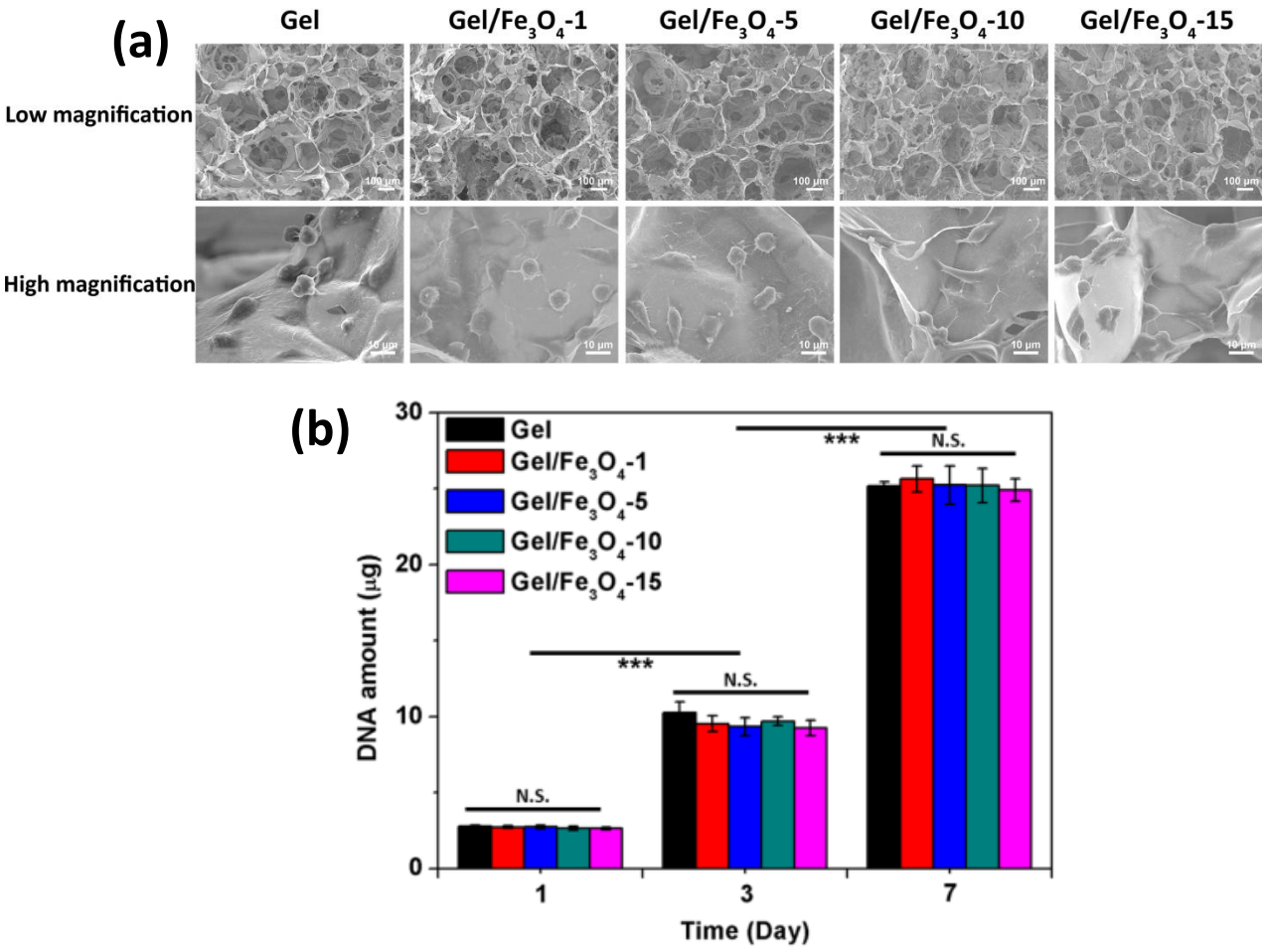

Fig. 2.7. (a) SEM images of Gel and Gel/Fe_3O_4 scaffolds after cell culture of 1 d. (b) DNA quantification of Gel and Gel/Fe_3O_4 scaffolds after cell culture of 1, 3 and 7 d. The data are presented as mean ± SD values. N.S., no significant difference, *$p < 0.05$, **$p < 0.01$ and ***$p < 0.001$.

for 1, 3, and 7 d, the cell/scaffold constructs were used for quantification of DNA amount. SEM observation showed that the cells had a homogeneous distribution and well adhered on the pore walls of the Gel and

Gel/Fe_3O_4 composite scaffolds as shown in Fig. 2.7a. There was no difference in cell adhesion among the Gel scaffolds and Gel/Fe_3O_4 composite scaffolds. The DNA amount in all the scaffolds significantly increased with culture time (Fig. 2.7b). There was no significant difference of DNA amount among the scaffolds. The results indicated that the cells could adhere and proliferate in all the scaffolds. Incorporation of Fe_3O_4 nanoparticles did not influence cell adhesion and proliferation, suggesting good biocompatibility of the Gel/Fe_3O_4 composite scaffolds. The Fe_3O_4 nanoparticles were embedded in the gelatin matrices of the composite scaffolds and should not directly interact with the cells. The cells adhered in the scaffolds through interaction with gelatin matrices that has been reported to have good biocompatibility.[51, 52]

2.4.5 *In vitro* photothermal ablation of HeLa cells

The localized photothermal therapeutic effect of Gel/Fe_3O_4 composite scaffolds on HeLa cells was evaluated by exposing the cell/scaffold constructs to NIR laser for 3 min (1 cycle). WST-1 was used to determine the cell viability (Fig. 2.8). Without laser irradiation, the cell viability in Gel and Gel/Fe_3O_4 scaffolds did not show obvious difference. When the Gel scaffolds were exposed to the NIR laser, as a control group, the cell viability decreased a little with no significant difference from the case without laser irradiation. The results indicated that the Gel scaffolds had no photothermal therapy capability for cancer cells and the laser irradiation only had very small influence on cell viability. However, a significant decrease of cell viability was observed in all the Gel/Fe_3O_4 composite scaffolds after laser irradiation for 3 min. Moreover, the cell viability decrease was dependent on the amount of Fe_3O_4 nanoparticles in the composite scaffolds. In particular, the cell viability in Gel/Fe_3O_4-15 decreased to almost 0% after laser irradiation. It meant almost all the cancer cells were killed, suggesting a very high photothermal therapy capability of the Gel/Fe_3O_4-15 scaffolds. Higher amount of Fe_3O_4 nanoparticles in the composite scaffolds had a higher killing effect.

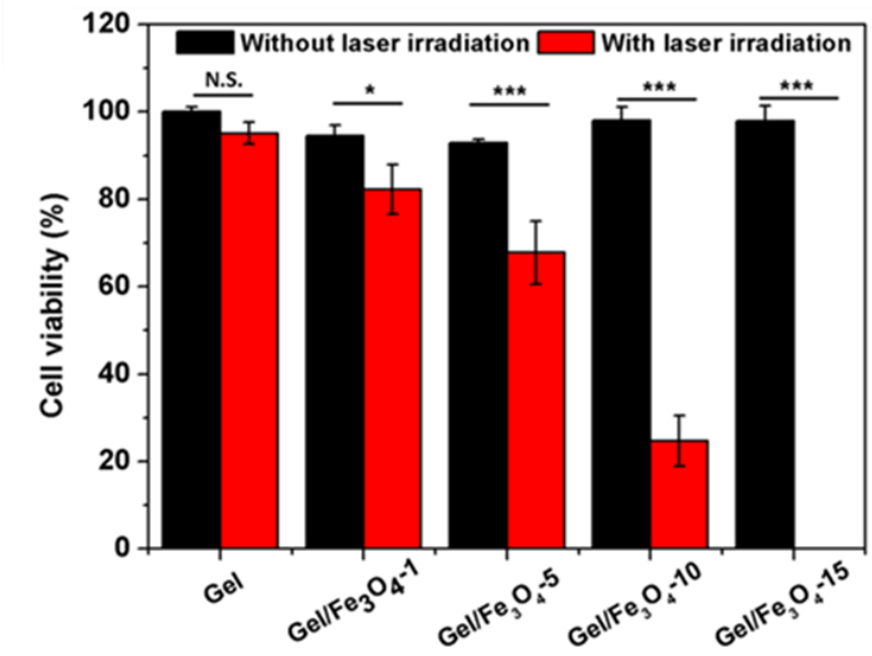

Fig. 2.8. Cell viability of HeLa cells in the Gel scaffolds and Gel/Fe_3O_4 composite scaffolds without or with 3 min laser irradiation (one irradiation cycle). The data are presented as mean ± SD values. N.S., no significant difference, *$p < 0.05$, **$p < 0.01$ and ***$p < 0.001$.

In clinical application, one of the problems is recurrence of tumor. The repeating photothermal treatment should provide an efficient solution to this issue. However, conventional nanoparticle injection-based photothermal technology is hardly to achieve this goal because of the easy leakage of nanoparticles from tumor sites. Herein, we supposed the porous Gel/Fe_3O_4 composite scaffolds could serve as a localized photothermal agent, thus providing ideal platform for repeating photothermal therapy. In order to confirm this hypothesis, the cell cultured Gel/Fe_3O_4 scaffolds were exposed to the NIR laser for different repeated heating cycles and the cell viability after each cycle was measured (Fig. 2.9). Even after 3 cycles of laser irradiation, the cell viability in the Gel scaffolds was still as high as 85.6 ± 1.6%. However, when the Gel/Fe_3O_4 composite scaffolds were exposed to the NIR laser for different irradiation cycles, the cell viability decreased significantly, especially for the Gel/Fe_3O_4-5, Gel/Fe_3O_4-10 and Gel/Fe_3O_4-15 composite scaffolds. Almost all of the cells in Gel/Fe_3O_4-15 were killed just after one cycle irradiation. Moreover, the cell viability in Gel/Fe_3O_4-5 composite scaffolds after one irradiation cycle was reduced to 67.8 ± 7.2%, and further reduced to 54.9 ± 4.5% and 35.6 ± 9.3% after two and three irradiation cycles, respectively. The photothermal killing effect during repeating irradiation increased with the amount of incorporated Fe_3O_4 nanoparticles. Particularly, almost all of the cancer cells in Gel/Fe_3O_4-10 scaffold were shown to be killed after three cycle of irradiation. These results indicated that the repeated laser irradiation could lead to an enhanced photothermal killing effect on cancer cells in the Gel/Fe_3O_4 composite scaffolds, suggesting the composite scaffolds might offer a good therapy strategy to address the recurrence of tumor.

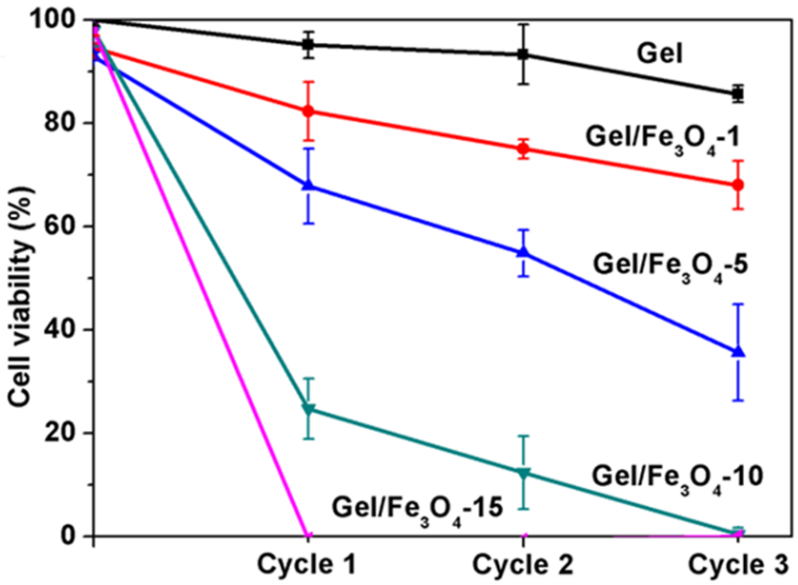

Fig. 2.9. Cell viability of HeLa cells in the scaffolds with repeating laser irradiation for different cycles. The data are presented as mean ± SD values.

Live/dead staining of cells cultured in the Gel and Gel/Fe_3O_4 scaffolds with and without laser irradiation was conducted to visualize the photothermal ablation of cancer cells. As shown in the Fig. 2.10, most of the cells were alive (indicated by green fluorescence) in the Gel scaffolds even after 3 times of laser irradiation. As for the Gel/Fe_3O_4 composite scaffolds, few dead cells (indicated by red fluorescence) were observed without laser irradiation treatment. However, upon exposure to the NIR laser, numerous HeLa cells were dead. More dead cells were observed when the amount of Fe_3O_4 nanoparticles in composite scaffolds and laser irradiation cycle increased. For the Gel/Fe_3O_4-15 composite scaffold, one laser irradiation cycle was enough to kill all of the Hela cells, indicating their high photothermal cancer ablation efficiency. These live/dead staining results were well consistent with the above WST-1 results.

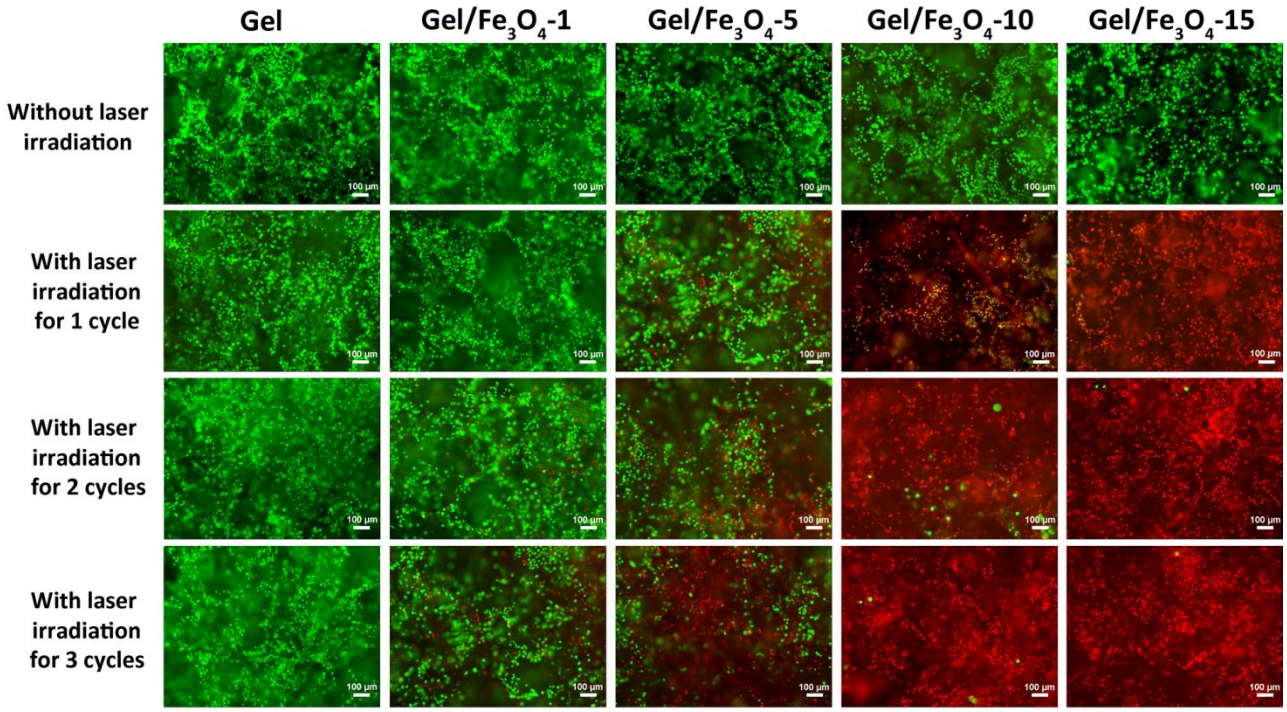

Fig. 2.10. Live/Dead staining of HeLa cells in the Gel scaffolds and Gel/Fe_3O_4 composite scaffolds without or with laser irradiation for different cycles.

The results indicated that the Gel/Fe_3O_4 composite scaffolds could kill cancer cells efficiently through NIR laser irradiation. The killing efficiency of the Gel/Fe_3O_4 scaffolds could be improved by repeated photothermal treatment. The killing effect of the composite scaffolds should be due to the raised temperate generated from the photothermal conversion during NIR laser irradiation. Higher content of Fe_3O_4 nanoparticles in the composite scaffolds induced higher temperature rise and therefore showed higher photothermal ablation effect. The increased capacity of photothermal ablation of the composite scaffolds with repeated laser irradiation should be due to the big increase of temperature in the composite scaffolds during repeated NIR laser irradiation. On the other hand, Fe_3O_4 nanoparticles in the scaffolds could be gradually degraded and Fe^{3+} ions should be released. Fe^{3+} ions have been reported to have good effects on cell responses.[38, 42] Wu *et al*. have reported that the released Fe^{3+} ion can enhance bone-related gene expression and promote osteogenic differentiation of rBMSCs.[38] Besides cancer cell ablation effect, the scaffolds should also have the capacity to stimulate tissue regeneration.

2.5 Conclusions

In summary, Gel/Fe_3O_4 composite scaffolds with controlled pore structures were prepared by incorporating Fe_3O_4 nanoparticles in the Gel porous scaffolds using ice particulates as a porogen material. The Gel/Fe_3O_4 composite scaffolds could absorb the NIR light and convert it to heat to elevate the local temperature efficiently. *In vitro* studies demonstrated that the Gel/Fe_3O_4 composite scaffolds had good biocompatibility and showed excellent photothermal ablation of cancer cells. All the cancer cells in the Gel/Fe_3O_4-15 composite scaffold having a high content of Fe_3O_4 nanoparticles could be killed after one cycle of laser irradiation. The Gel/Fe_3O_4 composite also showed the repeated local heating ablation of cancer cells

and repeated irradiation enhanced photothermal ablation effect. All of results indicated that Gel/Fe_3O_4 composite scaffolds should be useful for photothermal therapy of cancer.

2.6 References

1. Baskar, R.; Lee, K. A.; Yeo, R.; Yeoh, K.-W., Cancer and radiation therapy: current advances and future directions. *Int. J. Med. Sci.* **2012,** 9, (3), 193-199.
2. DeVita, V. T.; Chu, E., A history of cancer chemotherapy. *Cancer Res* **2008,** 68, (21), 8643-8653.
3. Bird, J. E., Advances in the surgical management of bone tumors. *Curr. Oncol. Rep.* **2014,** 16, (7), 1-6.
4. Maeng, J. H.; Lee, D.-H.; Jung, K. H.; Bae, Y.-H.; Park, I.-S.; Jeong, S.; Jeon, Y.-S.; Shim, C.-K.; Kim, W.; Kim, J., Multifunctional doxorubicin loaded superparamagnetic iron oxide nanoparticles for chemotherapy and magnetic resonance imaging in liver cancer. *Biomaterials* **2010,** 31, (18), 4995-5006.
5. Li, Z.; Huang, H.; Tang, S.; Li, Y.; Yu, X.-F.; Wang, H.; Li, P.; Sun, Z.; Zhang, H.; Liu, C., Small gold nanorods laden macrophages for enhanced tumor coverage in photothermal therapy. *Biomaterials* **2016,** 74, 144-154.
6. Kim, J.; Kim, J.; Jeong, C.; Kim, W. J., Synergistic nanomedicine by combined gene and photothermal therapy. *Adv. Drug Deliv. Rev.* **2015,** 98, (1), 99-112.
7. Shen, S.; Wang, S.; Zheng, R.; Zhu, X.; Jiang, X.; Fu, D.; Yang, W., Magnetic nanoparticle clusters for photothermal therapy with near-infrared irradiation. *Biomaterials* **2015,** 39, 67-74.
8. Lal, S.; Clare, S. E.; Halas, N. J., Nanoshell-enabled photothermal cancer therapy: impending clinical impact. *Acc. Chem. Res.* **2008,** 41, (12), 1842-1851.
9. Yang, K.; Xu, H.; Cheng, L.; Sun, C.; Wang, J.; Liu, Z., *In vitro* and *in vivo* near-infrared photothermal therapy of cancer using polypyrrole organic nanoparticles. *Adv. Mater.* **2012,** 24, (41), 5586-5592.
10. Melancon, M. P.; Zhou, M.; Li, C., Cancer theranostics with near-infrared light-activatable multimodal nanoparticles. *Acc. Chem. Res.* **2011,** 44, (10), 947-956.
11. Chu, M.; Shao, Y.; Peng, J.; Dai, X.; Li, H.; Wu, Q.; Shi, D., Near-infrared laser light mediated cancer therapy by photothermal effect of Fe_3O_4 magnetic nanoparticles. *Biomaterials* **2013,** 34, (16), 4078-4088.
12. Shen, S.; Kong, F.; Guo, X.; Wu, L.; Shen, H.; Xie, M.; Wang, X.; Jin, Y.; Ge, Y., CMCTS stabilized Fe 3 O 4 particles with extremely low toxicity as highly efficient near-infrared photothermal agents for in vivo tumor ablation. *Nanoscale* **2013,** 5, (17), 8056-8066.
13. Chen, H.; Burnett, J.; Zhang, F.; Zhang, J.; Paholak, H.; Sun, D., Highly crystallized iron oxide nanoparticles as effective and biodegradable mediators for photothermal cancer therapy. *J. Mater. Chem. B* **2014,** 2, (7), 757-765.
14. Zhiguo, Z.; Yanan, S.; Jinchao, S.; Jie, W.; Chao, Y.; Bin, K.; Wei, L.; Hong, Y.; Shiping, Y.; Wei, W., Iron/iron oxide core/shell nanoparticles for magnetic targeting MRI and near-infrared photothermal therapy. *Biomaterials* **2014,** 35, (26), 7470-7478.
15. Song, X.; Gong, H.; Yin, S.; Liang, C.; Wang, C.; Li, Z.; Li, Y.; Wang, X.; Liu, G.; Liu, Z., Ultra-Small Iron Oxide Doped Polypyrrole Nanoparticles for In Vivo Multimodal Imaging Guided Photothermal Therapy. *Adv. Funct. Mater.* **2014,** 24, (9), 1194–1201.

16. Liu, T.; Shi, S.; Liang, C.; Shen, S.; Cheng, L.; Wang, C.; Song, X.; Goel, S.; Barnhart, T. E.; Cai, W., Iron oxide decorated MoS_2 nanosheets with double PEGylation for chelator-free radiolabeling and multimodal imaging guided photothermal therapy. *ACS Nano* **2015,** 9, (1), 950-960.
17. Wang, X.; Wang, C.; Cheng, L.; Lee, S.-T.; Liu, Z., Noble metal coated single-walled carbon nanotubes for applications in surface enhanced Raman scattering imaging and photothermal therapy. *J. Am. Chem. Soc.* **2012,** 134, (17), 7414-7422.
18. Moon, H. K.; Lee, S. H.; Choi, H. C., *In vivo* near-infrared mediated tumor destruction by photothermal effect of carbon nanotubes. *ACS Nano* **2009,** 3, (11), 3707-3713.
19. †, F. Z.; †, S. W.; Wu, B.; Chen, W. R.; Da, X., Mitochondria-targeting single-walled carbon nanotubes for cancer photothermal therapy. *Small* **2011,** 7, (19), 2727–2735.
20. Yang, K.; Zhang, S.; Zhang, G.; Sun, X.; Lee, S.-T.; Liu, Z., Graphene in mice: ultrahigh in vivo tumor uptake and efficient photothermal therapy. *Nano Lett.* **2010,** 10, (9), 3318-3323.
21. Robinson, J. T.; Tabakman, S. M.; Liang, Y.; Wang, H.; Sanchez Casalongue, H.; Vinh, D.; Dai, H., Ultrasmall reduced graphene oxide with high near-infrared absorbance for photothermal therapy. *J. Am. Chem. Soc.* **2011,** 133, (17), 6825-6831.
22. Wang, Y. W.; Fu, Y. Y.; Peng, Q.; Guo, S. S.; Liu, G.; Li, J.; Yang, H. H.; Chen, G. N., Dye-enhanced graphene oxide for photothermal therapy and photoacoustic imaging. *J. Mater. Chem. B* **2013,** 1, (42), 5762-5767.
23. Li, J.; Cai, R.; Kawazoe, N.; Chen, G., Facile preparation of albumin-stabilized gold nanostars for the targeted photothermal ablation of cancer cells. *J. Mater. Chem. B* **2015,** 3, (28), 5806-5814.
24. Zhang, J.; Liu, G.; He, F.; Chen, L.; Huang, Y., Au@ Cu 7 S 4 yolk–shell nanoparticles as a 980 nm laser-driven photothermal agent with a heat conversion efficiency of 63%. *RSC Adv.* **2015,** 5, (107), 87903-87907.
25. Jang, B.; Park, J. Y.; Tung, C. H.; Kim, I. H.; Choi, Y., Gold nanorod-photosensitizer complex for near-infrared fluorescence imaging and photodynamic/photothermal therapy in vivo. *ACS Nano* **2011,** 5, (2), 1086-1094.
26. Samal, S. K.; Dash, M.; Shelyakova, T.; Declercq, H. A.; Uhlarz, M.; Bañobre-López, M.; Dubruel, P.; Cornelissen, M.; Herrmannsdörfer, T.; Rivas, J., Biomimetic magnetic silk scaffolds. *ACS Appl. Mater. Interfaces* **2015,** 7, (11), 6282-6292.
27. Tampieri, A.; Iafisco, M.; Sandri, M.; Panseri, S.; Cunha, C.; Sprio, S.; Savini, E.; Uhlarz, M.; Herrmannsdörfer, T., Magnetic bioinspired hybrid nanostructured collagen–hydroxyapatite scaffolds supporting cell proliferation and tuning regenerative process. *ACS Appl. Mater. Interfaces* **2014,** 6, (18), 15697-15707.
28. Mao, H.; Li, J.; Dulińska-Molak, I.; Kawazoe, N.; Takeda, Y.; Mamiya, H.; Chen, G., Cellular effects of magnetic nanoparticles explored by atomic force microscopy. *Biomater. Sci.* **2015,** 3, (9), 1284-1290.
29. Shi, D.; Sadat, M.; Dunn, A. W.; Mast, D. B., Photo-fluorescent and magnetic properties of iron oxide nanoparticles for biomedical applications. *Nanoscale* **2015,** 7, (18), 8209-8232.
30. Demirer, G. S.; Okur, A. C.; Kizilel, S., Synthesis and design of biologically inspired biocompatible iron oxide nanoparticles for biomedical applications. *J. Mater. Chem. B* **2015,** 3, (40), 7831-7849.
31. Luo, Y.; Yang, J.; Yan, Y.; Li, J.; Shen, M.; Zhang, G.; Mignani, S.; Shi, X., RGD-functionalized ultrasmall iron oxide nanoparticles for targeted T1-weighted MR imaging of gliomas. *Nanoscale* **2015,** 7, (34).

32. Huang, C.; Soenen, S. J.; Rejman, J.; Trekker, J.; Chengxun, L.; Lagae, L.; Ceelen, W.; Wilhelm, C.; Demeester, J.; De Smedt, S. C., Magnetic electrospun fibers for cancer therapy. *Adv. Funct. Mater.* **2012,** 22, (12), 2479-2486.
33. Hsiao, C.-W.; Chuang, E.-Y.; Chen, H.-L.; Wan, D.; Korupalli, C.; Liao, Z.-X.; Chiu, Y.-L.; Chia, W.-T.; Lin, K.-J.; Sung, H.-W., Photothermal tumor ablation in mice with repeated therapy sessions using NIR-absorbing micellar hydrogels formed in situ. *Biomaterials* **2015,** 56, 26-35.
34. Wang, S.; Chen, Y.; Li, X.; Gao, W.; Zhang, L.; Liu, J.; Zheng, Y.; Chen, H.; Shi, J., Injectable 2D MoS_2-integrated drug delivering implant for highly efficient NIR-triggered synergistic tumor hyperthermia. *Adv. Mater.* **2015,** 27, (44), 7117-7122.
35. Kim, Y. J.; Ebara, M.; Aoyagi, T., A smart hyperthermia nanofiber with switchable drug release for inducing cancer apoptosis. *Adv. Funct. Mater.* **2013,** 23, (46), 5753-5761.
36. Zhang, Z.; Liu, S.; Xiong, H.; Jing, X.; Xie, Z.; Chen, X.; Huang, Y., Electrospun PLA/MWCNTs composite nanofibers for combined chemo-and photothermal therapy. *Acta Biomater.* **2015,** 26, 115-123.
37. GhavamiNejad, A.; Sasikala, A. R. K.; Unnithan, A. R.; Thomas, R. G.; Jeong, Y. Y.; Vatankhah-Varnoosfaderani, M.; Stadler, F. J.; Park, C. H.; Kim, C. S., Mussel-inspired electrospun smart magnetic nanofibers for hyperthermic chemotherapy. *Adv. Funct. Mater.* **2015,** 25, (19), 2867-2875.
38. Zhang, Y.; Zhai, D.; Xu, M.; Yao, Q.; Chang, J.; Wu, C., 3D-printed bioceramic scaffolds with a Fe 3 O 4/graphene oxide nanocomposite interface for hyperthermia therapy of bone tumor cells. *J. Mater. Chem. B* **2016,** 4, (17), 2874-2886.
39. Ma, H.; Jiang, C.; Zhai, D.; Luo, Y.; Chen, Y.; Lv, F.; Yi, Z.; Deng, Y.; Wang, J.; Chang, J., A bifunctional biomaterial with photothermal effect for tumor therapy and bone regeneration. *Adv. Funct. Mater.* **2016,** 26, (8), 1197-1208.
40. Lin, T.-C.; Lin, F.-H.; Lin, J.-C., In vitro feasibility study of the use of a magnetic electrospun chitosan nanofiber composite for hyperthermia treatment of tumor cells. *Acta Biomater.* **2012,** 8, (7), 2704-2711.
41. Chen, Y.; Jiang, L.; Wang, R.; Lu, M.; Zhang, Q.; Zhou, Y.; Wang, Z.; Lu, G.; Liang, P.; Ran, H., Injectable smart phase-transformation implants for highly efficient *in vivo* magnetic-hyperthermia regression of tumors. *Adv. Mater.* **2014,** 26, (44), 7468-7473.
42. Zhang, J.; Zhao, S.; Zhu, M.; Zhu, Y.; Zhang, Y.; Liu, Z.; Zhang, C., 3D-printed magnetic Fe 3 O 4/MBG/PCL composite scaffolds with multifunctionality of bone regeneration, local anticancer drug delivery and hyperthermia. *J. Mater. Chem. B* **2014,** 2, (43), 7583-7595.
43. Li, J.; Hu, Y.; Yang, J.; Sun, W.; Cai, H.; Wei, P.; Sun, Y.; Zhang, G.; Shi, X.; Shen, M., Facile synthesis of folic acid-functionalized iron oxide nanoparticles with ultrahigh relaxivity for targeted tumor MR imaging. *J. Mater. Chem. B* **2015,** 3, (28), 5720-5730.
44. Zhang, Q.; Lu, H.; Kawazoe, N.; Chen, G., Pore size effect of collagen scaffolds on cartilage regeneration. *Acta Biomater.* **2014,** 10, (5), 2005-2013.
45. Karageorgiou, V.; Kaplan, D., Porosity of 3D biomaterial scaffolds and osteogenesis. *Biomaterials* **2005,** 26, (27), 5474-5491.
46. Nge, T. T.; Nogi, M.; Yano, H.; Sugiyama, J., Microstructure and mechanical properties of bacterial cellulose/chitosan porous scaffold. *Cellulose* **2010,** 17, (2), 349-363.

47. Chen, S.; Zhang, Q.; Kawazoe, N.; Chen, G., Effect of high molecular weight hyaluronic acid on chondrocytes cultured in collagen/hyaluronic acid porous scaffolds. *RSC Adv*. **2015,** 5, (114), 94405-94410.
48. Liu, G.; He, F.; Zhang, J.; Li, L.; Li, F.; Chen, L.; Huang, Y., Yolk–shell structured Fe_3O_4@ C@ F-TiO 2 microspheres with surface fluorinated as recyclable visible-light driven photocatalysts. *Appl. Catal. B* **2014,** 150, 515-522.
49. Ki, C. S.; Baek, D. H.; Gang, K. D.; Lee, K. H.; Um, I. C.; Park, Y. H., Characterization of gelatin nanofiber prepared from gelatin–formic acid solution. *Polymer* **2005,** 46, (14), 5094-5102.
50. Chang, M. C.; Ko, C.-C.; Douglas, W. H., Preparation of hydroxyapatite-gelatin nanocomposite. *Biomaterials* **2003,** 24, (17), 2853-2862.
51. Lien, S.-M.; Ko, L.-Y.; Huang, T.-J., Effect of pore size on ECM secretion and cell growth in gelatin scaffold for articular cartilage tissue engineering. *Acta Biomater.* **2009,** 5, (2), 670-679.

Chapter 3

Multifunctional gelatin/Fe_3O_4 scaffolds for cancer cell capture and ablation

3.1 Summary

Scaffolds have been explored as a useful carrier to deliver efficient photothermal conversion agents for localized photothermal therapy applications because of the limitations of free nanoparticles. However, cell capture by porous structures cannot discriminate cancer cells and normal cells. In this study, folic acid (FA) as a typical targeting ligand for cancer cells was introduced in the porous Gel/Fe_3O_4 scaffolds. Poly-L-lysine (PLL) was mixed with gelatin to increase amino side groups for FA incorporation. By changing PLL amount, the number of free amino groups in the composite scaffolds could be controlled. After reaction with activated FA, Gel/Fe_3O_4-FA composite scaffolds with different FA incorporation amount were prepared. Cell culture results showed that the Gel/Fe_3O_4-FA scaffolds could efficiently capture folate-positive cervical cancer cells (HeLa) compared with pure Gel scaffold within 30 min incubation. The capture efficiency increased with the increase of FA amount in the scaffolds. Furthermore, the Gel/Fe_3O_4-FA composite scaffold could efficiently kill cancer cells. Cancer cells in the composite scaffolds were killed during NIR laser irradiation. The results indicated that the multifunctional Gel/Fe_3O_4-FA porous scaffolds had good cancer cell capture ability and excellent cancer cells ablation efficacy, which may provide useful information for the design of multifunctional scaffolds with cancer cell capture capacity and photothermal ablation ability.

3.2 Introduction

As a promising strategy for malignant tumor treatment, photothermal therapy (PTT) has received intensive attention. PTT uses photothermal conversion agents to convert near infrared (NIR) light into heat to damage and kill cancer cells.[1, 2, 3, 4] Because of the small size and high photothermal conversion efficiency of nanomaterials, they have attracted great interest for PTT.[5-10] Iron oxide (Fe_3O_4) nanoparticles have been widely investigated as conversion agents for PTT application due to their excellent photothermal conversion efficiency and non-invasive manipulation ability.[11-15] However the poor targeting specificity and easy diffusion of free nanoparticles still restrict their broad application in clinic.[16-19]

Recently, porous scaffold have been used as an effective carrier for localized delivery of photothermal

conversion agents.[20-25] The scaffolds possess photothermal effect and can elevate local temperature quickly during NIR laser irradiation. Using photothermal scaffolds for PTT applications have some advantages comparing to free nanoparticles. One of main advantages of photothermal scaffolds is that they can be directly implanted into the tumor site.[26, 27] Therefore, the immobilized photothermal conversion agents can be efficiently delivered and localized to the tumor site, which should be beneficial to achieving high local heating effect. More importantly, because the photothermal conversion agents are immobilized on the pore surfaces of the scaffold or embedded in the scaffold matrix, they can be easily retained at the tumor site for a long period and can been repeatedly used without leakage and decrement of heating efficiency.[28, 29] Furthermore, after tumor ablation, the porous scaffolds can also support penetration of healthy cells and promote regeneration of healthy tissue, which contributes to the subsequent tissue recovery and regeneration.[30-32] However, although the photothermal scaffolds can accommodate various cells and have excellent photothermal efficiency, they cannot specifically or selectively capture and kill cancer cells. Therefore, it is highly desirable to increase the capture ability of cancer cells in porous scaffolds while minimize their damage to healthy cells.

In this study, folic acid (FA), as a cancer cells recognition ligand,[33-38] was introduced in the porous gelatin/iron oxide (Gel/Fe_3O_4) composite scaffolds. To increase the amount of FA in the scaffolds with a controllable manner, poly-L-lysine (PLL), was incorporated in gelatin (Gel) porous scaffolds to increase free amino side groups in the scaffolds for binding with FA. The Gel/Fe_3O_4-FA composite scaffolds possessed strong absorption in NIR region and the temperature could be quickly elevated during laser irradiation. Folate-positive cancer cells (HeLa) could be efficiently captured by the Gel/Fe_3O_4-FA composite scaffolds and the capture efficiency could be enhanced by the increasing of FA amount in the scaffolds. Furthermore, cancer cells in the Gel/Fe_3O_4-FA composite scaffold could be efficiently killed during laser irradiation.

3.3 Materials and methods

3.3.1 Materials

Iron (III) chloride hexahydrate ($FeCl_3{\cdot}6H_2O$, 97.0%), sodium sulfite (Na_2SO_3, 98.0%), 2-(Nmorpholino) ethanesulfonic acid (MES), Eagle's minimum essential medium (EMEM), penicillin, streptomycin and trypsin/EDTA were purchased from Sigma-Aldrich (St. Louis, MO, USA). Trisodium citrate dihydrate ($C_6H_5Na_3O_7{\cdot}2H_2O$,), 25 wt% ammonia solution, acetic acid, ethanol (99.5%), folic acid (FA), dimethyl sulfoxide (DMSO), glysine (99.0%), 6 mol/L hydrochloric acid (HCl), sodium hydroxide (NaOH, 96.0%) and N-hydroxysuccinimide (NHS) were purchased from Wako Pure Industries, Ltd (Tokyo, Japan). Porcine derived gelatin was provided by Nitta Gelatin (Osaka, Japan). Poly-L-lysine (PLL) and 1-ethyl-3-(3-dimethylaminopropyl) carbodiimide (EDC) were purchased from Peptide Institute, Inc. (Osaka, Japan). WST-1 reagent was obtained from Roche Molecular Biochemicals (Mannheim, Germany). DAPI solution and live/dead double staining kit was purchased from Dojindo Laboratories (Kumamoto, Japan). Collagenese type I was purchased from Worthington Biochemical Corporation (Lakewood, NJ, USA). All the chemicals and materials were used as received without further purification. The water in all experiments was purified using a Q-POD Milli-Q water purification system (Millipore Corp., Billerica, MA, USA) with a resistivity of 18.2 MΩ·cm.

3.3.2 Synthesis of Fe_3O_4 nanoparticles

Citrate-stabilized Fe_3O_4 nanoparticles were synthesized according to a previously reported method.[39] Briefly, 20.0 mL Na_2SO_3 aqueous solution (20.0 mg/mL) was mixed with 40.0 mL $FeCl_3{\cdot}6H_2O$ aqueous solution (65.0 mg/mL) under nitrogen atmosphere protection. After mixing for 10 min, the mixture solution was put into a 75 ^oC water bath, followed by the addition of 4.0 mL ammonia solution (25 wt%) and 10 mL citrate solution (0.1 g/mL). After reaction for 40 min, the whole set was transferred on a magnetic stirrer at room temperature for more than 1.5 h to cool down solution and then the formed Fe_3O_4 nanoparticles were collected by magnetic separation, washed four times with MilliQ water and finally re-suspended in water and stored at 4 ^oC for further use.

3.3.3 Preparation of PLL-incorporated porous Gel/Fe_3O_4 composite scaffolds

PLL-incorporated porous Gel/Fe_3O_4 composite scaffolds were prepared by an ice particulates templating method according to a previously reported method with some modification.[40, 41] Briefly, a Gel solution (95.0 mg/mL) was firstly prepared by dissolving Gel into an acetic acid solution. An appropriate amount PLL (43.6 mg, 60.9 mg, 95.4 mg and 164.5 mg) was dissolved in 4.2 mL water. And then 4.2 mL PLL solution was added into 5.0 mL Gel solution during magnetic stirring. After that, 970.0 μL Fe_3O_4 nanoparticles suspension solution (38.2 mg/mL) was added into the mixture solution dropwise and sonicated at room temperature for 30 min. The mixture suspension solution was put at -4 ^oC for 40 min for temperature balance.

Ice particulates were prepared by spraying pure water into liquid nitrogen.[42, 43] The ice particulates with diameters in a range of 425 ~ 500 μm were obtained by sieving the prepared ice particulates at -15 ^oC with two sieves having average mesh sizes of 425 and 500 μm. And then the ice particulates were transferred into a cooled glass bottle and kept at -5 ^oC for 2 h for temperature balance. After 2 h temperature balance, the ice particulates were mixed thoroughly with the aforementioned cooled mixture suspension solution at a weight/volume ratio of 7 : 3 (g/mL) at -5 ^oC. The mixture of solution and ice particulates was poured into a cooled silicone mold and the entire set was first put into -20 ^oC low temperature chamber for 12 h and then transferred to -80 ^oC freezer for 4 h for further freezing. Finally, the frozen construct was freeze-dried for 3 d under a vacuum of less than 5 Pa for 24 h by using a freeze dryer (FDU-2200, Tokyo Rikakikai Co., Ltd.).

After freeze-drying, the scaffolds were cut into thin slices and washed with ethanol (99.5%) for 10 times to remove residual acetic acid. After washing with ethanol, the composite scaffolds were cross-linked with EDC and NHS ethanol/water solution. Three mixture solvents with a decreasing ethanol concentration (ethanol/water = 95/5, 90/10, 85/15, v/v) were used to prepare the crosslinking solutions, which contained 50 mM EDC, 20 mM NHS and 0.1% (wt/v) MES. The composite scaffolds were crosslinked sequentially by the three crosslinking solutions at room temperature for every 8 h in each solution. After cross-linking, the composite scaffolds were rinsed with PBS for 3 times. The composite scaffolds were further treated with 0.1 M glycine at room temperature for 6 h to block the un-reacted but activated carboxyl groups in the scaffolds. Finally, the scaffolds were thoroughly washed with water for more than 10 times and freeze-dried for 2 d to obtain PLL-incorporated porous Gel/Fe_3O_4 composite scaffolds. The PLL-incorporated porous Gel/Fe_3O_4 composite scaffolds prepared from the weight feeding ratio of PLL to (PLL and Gel) of 8.4, 11.4, 16.7 and 25.7% were referred as CS-1, CS-2, CS-3 and CS-4, respectively. The pure Gel and Gel/Fe_3O_4 scaffolds were also prepared as controls. The preparation procedure was the same as that of the CS scaffolds without adding of PLL and Fe_3O_4 (Gel scaffold) or without PLL (Gel/Fe_3O_4 scaffold).

3.3.4 Preparation of porous Gel/Fe_3O_4-FA composite scaffolds

FA was linked to the composite scaffolds by using ECD/NHS technique.[44-46] Firstly, FA (0.5 mmol) was dissolved in 2.5 mL DMSO. And then EDC (1.0 mmol) and NHS (1.0 mmol) were added into the FA solution under stirring for 3 h. After activation, 2.5 mL FA/DMSO solution was added in 47.5 mL PBS solution (FA/DMSO/PBS). Subsequently the Gel/Fe_3O_4 scaffolds that were prepared as above mentioned without blocking with glycine were immersed in the FA/DMSO/PBS solution to react for 1 d. The ratio of feeding FA amount to the free amino groups in the scaffolds was set to 3 : 1. After reaction, the Gel/Fe_3O_4-FA scaffolds were washed with DMSO/PBS for 3 times, PBS for 3 times, MilliQ water for 3 times and then further treated with 0.1 M glycine for 6 h. Finally, the scaffolds were thoroughly washed with water for more than 10 times and freeze-dried for 2 d to obtain the final Gel/Fe_3O_4-FA composite scaffolds. The Gel/Fe_3O_4-FA composite scaffolds prepared from CS-1, CS-2, CS-3 and CS-4 were referred as CS-FA1, CS-FA2, CS-FA3 and CS-FA4, respectively.

3.3.5 Characterization of Fe_3O_4 nanoparticles and scaffolds

Morphology of the prepared Fe_3O_4 nanoparticles was investigated by transmission electron microscopy (TEM, JEOL 2011F, Japan). Dynamic light scattering (DLS) was used to measure the hydrodynamic size of the Fe_3O_4 nanoparticles. The morphology of Gel scaffolds and Gel/Fe_3O_4-FA composite scaffolds were observed by a scanning electron microscope (SEM, Hitachi S-4800, Japan). UV-visible absorption spectra of the solid phase scaffolds were recorded using a UV-2600 UV-visible spectrophotometer (Shimadzu Corp., Japan).

3.3.6 Photothermal effect of the Gel/Fe_3O_4-FA composite scaffolds

Photothermal effect of the Gel/Fe_3O_4-FA composite scaffolds with different FA grafting density was determined by exposing the scaffolds (5 × 3 × 1 mm) filled with 20 μL culture medium to a NIR laser (805 nm, Thorlabs Inc., USA) with a power density of 1.6 W cm^{-2} for 180 s. During laser irradiation, a digital thermometer (AS ONE Corp., Japan) was used to measure the temperature of the samples every 10 s. Pure Gel scaffold was also exposed for 180 s as a control. Every three samples were used to calculate the average and standard deviation.

3.3.7 Quantification of FA amount in Gel/Fe_3O_4-FA composite scaffolds

UV-Vis absorbance was used to quantify the FA amount in the Gel/Fe_3O_4-FA composite scaffolds. Firstly, a small piece (17 × 11 × 1 mm) of Gel/Fe_3O_4-FA composite scaffold was dissolved in 2 mL HCl solution (6 M) for 6 h. In order to exclude the effect of Fe^{3+} ion, 6 M NaOH was added into above solution and adjusted pH of the solution above 13. And then the mixture solution was centrifuged at 9500 rpm for 10 min. Finally, the supernant was taken out to measure the absorbance at FA specific absorption peak of 365 nm by a V-660 UV-Vis spectrophotometer (Jasco Corp., Tokyo, Japan). Every three samples were used to calculate the average and standard deviation.

3.3.8 Cancer cell capture experiment

A folate receptor-positive cell type, human cervical carcinoma cell line (HeLa cells), was used to evaluate the cell capture ability of Gel/Fe_3O_4-FA composite scaffolds. HeLa cells were seeded in 75 cm^2 tissue culture flasks and cultured in a regular EMEM medium supplemented with 10% FBS, penicillin (100 U mL^{-1}) and streptomycin (100 μg mL^{-1}) in 5% CO_2 incubator at 37 ^oC in a humidified environment. The cells were subcultured using a 0.05% trypsin-EDTA solution after reaching confluence. The subcultured HeLa cells were collected by centrifugation and re-suspended in serum-free EMEM medium to a concentration of 1×10^6/mL for cell seeding.

Before cell seeding, the Gel and Gel/Fe_3O_4 scaffolds, CS scaffolds and CS-FA scaffolds were cut into discs, sterilized with 70% ethanol, washed with water for 5 times and immersed into serum-free medium at 37 ^oC for 6 h. After removing the medium by using a sterile tissue paper, 1×10^5 HeLa cells were seeded into Gel scaffolds and Gel/Fe_3O_4-FA composite scaffolds.

For cell capture experiment, scaffolds were cut to cylinder-shape discs with a diameter of 6 mm and a height of 1 mm. The scaffold discs were put into glass rings (Φ 6 × H 10 mm) that were placed in the wells of a 24-well polystyrene cell culture plate. The glass rings were used to protect medium and cell leakage during cell seeding. 100 μL cell suspension solution (1×10^6/mL) was added to the scaffolds and incubated for 30 min. After 30 min incubation, the scaffolds were washed thoroughly with PBS for 3 times to remove un-attached cells. Gel, Gel/Fe_3O_4, CS-1, CS-2, CS-3 and CS-4 were also conducted as controls.

3.3.9 Counting of captured cell number and DAPI staining

After being cultured for 30 min as above mentioned, the cell/scaffold constructs were washed thoroughly by PBS. And then the cell/scaffolds constructs were put into 0.5 mL collagenase type I solution (0.5% (wt/v)) to digest for 10 min under mechanical shaking. After 10 min digestion, cell/scaffolds constructs were taken out and put into another 0.5 mL collagenase type I solution (0.5% (wt/v)) to digest for another 10 min. This process was repeated for 6 times and all the collagenase type I digestion solutions were collected (3.0 mL) into a 15.0 mL tube. 3.0 mL culture medium was added into the 15-mL tubes to stop the digestion. After that, the mixture solution was centrifuged at 1100 rpm for 5 min. Finally, supernatant was discarded and the cell pellets were re-suspended in 1.0 mL solution for counting cell number. Every six samples were used to calculate the average and standard deviation.

DAPI staining was conducted to stain the cells nuclei to visualize the captured cells in the scaffolds. After 30 min culture, the cell/scaffold constructs were washed thoroughly by PBS and fixed with 2.5% glutaraldehyde at room temperature for 2 h. And then the cell/scaffold constructs were washed with PBS for 3 times. Cell nuclei were stained with 1000-fold diluted DAPI solution in PBS at room temperature for 8 min. After staining, cell/scaffold constructs were rinsed with PBS for 3 times and their fluorescence images were obtained by using a fluorescent microscope (Olympus, Japan).

3.3.10 Cell viability and photothermal effect of composite scaffolds

For cell viability and photothermal effect experiments, the scaffolds were cut into discs (5 × 3 × 1 mm). 10.0 μL cell suspension containing 1×10^5 HeLa cells were seeded into each scaffold disc. After 5 h of incubation, the cell/scaffold constructs were transferred into 6-well plates and cultured in 5.0 mL serum medium in 5% CO_2 incubator at 37 ^oC. After cultured for 1 d, the cell/scaffold constructs were separated into

two different groups (without or with laser irradiation). For laser irradiation group, the cell/scaffold constructs were exposed to an NIR laser of 805 nm for 180 s. For no laser irradiation group, the cell/scaffold constructs were taken out from the incubator and put at room temperature for 180 s. After the treatments, the cell/scaffold constructs were cultured in serum medium for another 3 h. After that, cell viability was determined by WST-1 assay. The absorbance at 440 nm was measured by a microplate reader (Benchmark Plus, Bio-Rad, Hercules, CA, USA). The cell viability was normalized with the viability data of cells cultured in the Gel scaffolds. Every three samples were used for the measurement to calculate the average and standard deviation.

3.3.11 Statistical analysis

All of the data were presented as mean ± standard deviation (SD). Statistical analysis was performed using a one-way analysis of variance with Tukey's *post hoc* test for multiple comparisons. A value of $p < 0.05$ was considered to indicate a statistically significant difference. The data were indicated with (*) for $p < 0.05$, (**) for $p < 0.01$ and (***) for $p < 0.001$, respectively.

3.4 Results and discussion

3.4.1 Morphology of citrate-stabilized Fe_3O_4 nanoparticles

The Fe_3O_4 nanoparticles had spherical or quasi-spherical morphology as shown in Figure 3.1a. DLS analysis showed that the Fe_3O_4 nanoparticles dispersed in water had a single peak distribution (Figure 3.1b). Their hydrodynamic size was 123.1 ± 1.3 nm, which was much larger than the size measured from TEM images. This should be due to the partial aggregation of Fe_3O_4 nanoparticles in water. The partial aggregation in water should not affect the distribution of Fe_3O_4 nanoparticles in gelatin aqueous solution during scaffold preparation.

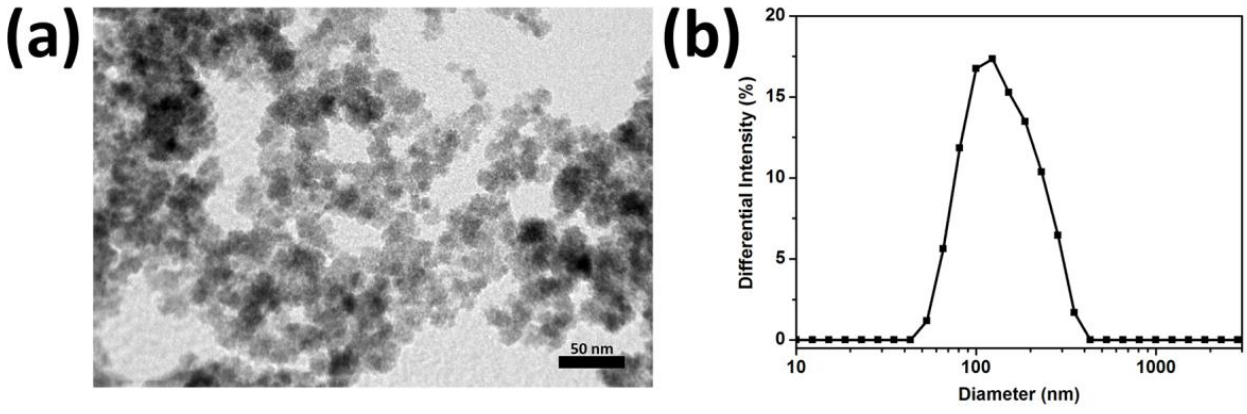

Fig. 3.1. TEM image of Fe_3O_4 nanoparticles (a). Hydrodynamic size of Fe_3O_4 nanoparticles measured by DLS (b).

3.4.2 Pore structure and surface morphology of Gel/Fe_3O_4-FA composite scaffolds

The Gel/Fe_3O_4-FA composite scaffolds were prepared by using ice particulates as a porogen material to control large pore structures. SEM observation showed that Gel and Gel/Fe_3O_4-FA composite scaffolds with different amount of FA had similar pore structures (Figure 3.2). Their pore structures and pore surfaces did not show obvious change. All the scaffolds possessed well controlled and interconnected pore structures consisting spherical large pores and interconnected small pores. The large pores were formed by the added ice particulates with controlled size (425 ~ 500 μm). The small pores should be due to the formed new ice crystals during freezing process. The well interconnected pore structure should be beneficial for cell penetration and adhesion into the scaffolds, resulting in a homogenous cell distribution throughout the scaffolds. High magnification SEM images showed the Gel/Fe_3O_4-FA composite scaffolds had rougher pore surfaces than did the pure Gel scaffolds. The size of Fe_3O_4 nanoparticles on the pore surfaces was larger than their size in TEM images but close to their hydrodynamic size. The results indicated that the Fe_3O_4 nanoparticles were partially aggregated in the Gel/Fe_3O_4-FA composite scaffolds.

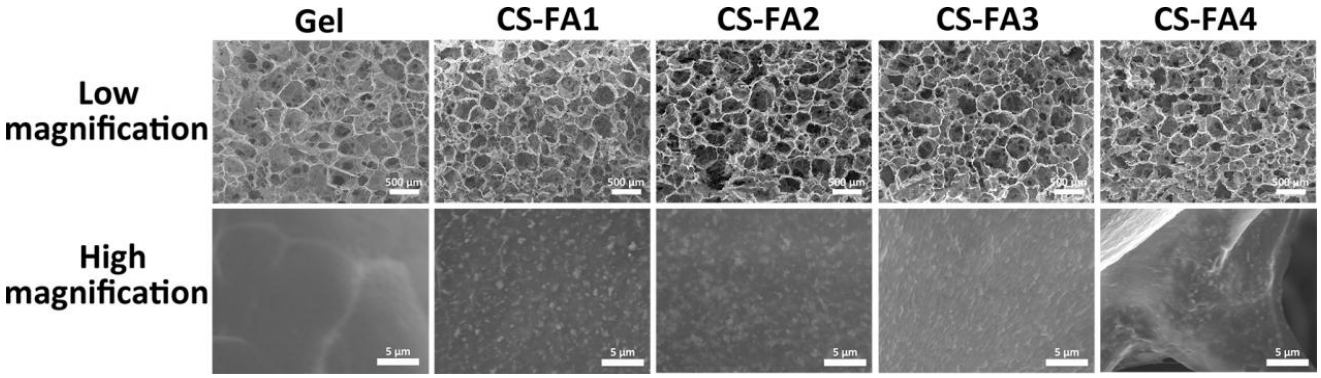

Fig. 3.2. SEM images of Gel, CS-FA1, CS-FA2, CS-FA3 and CS-FA4 scaffolds at a low magnification and morphology of pore surfaces at a high magnification.

3.4.3 UV absorption and photothermal conversion effect of Gel/Fe_3O_4-FA composite scaffolds

UV-Vis spectra were measured to evaluate the absorption properties of the Gel scaffolds and Gel/Fe_3O_4-FA composite scaffolds (Figure 3.3). Gel scaffolds showed no absorption at NIR wavelength (700 ~ 1100 nm). However the Gel/Fe_3O_4 composite scaffolds showed strong absorption at the NIR wavelength. The strong absorption of Gel/Fe_3O_4 composite scaffolds was due to the incorporation of Fe_3O_4 nanoparticles. Introduction of PLL and FA had no influence on the absorption of the composite scaffolds.

Photothermal conversion effect was investigated by irradiating Gel and Gel/Fe_3O_4-FA composite scaffolds with an 805 nm laser (Figure 3.4). The temperature of Gel scaffolds only slightly increased during laser irradiation. In contrast, the temperature of Gel/Fe_3O_4-FA composite scaffolds increased rapidly with laser irradiation. The temperature increase was 24.3 ± 0.6 ^oC, 24.2 ± 0.3 ^oC, 24.1 ± 0.9 ^oC and 23.7 ± 0.4 ^oC for CS-FA1, CS-FA2, CS-FA3 and CS-FA4 scaffolds, respectively. The photothermal conversion effect was ascribed to the strong NIR absorption of Fe_3O_4 nanoparticles in the composite scaffolds. Because the same amount of Fe_3O_4 nanoparticles was incorporated in all the composite scaffolds, temperature change of all the

Gel/Fe_3O_4-FA composite scaffolds with different FA grafting density was almost the same.

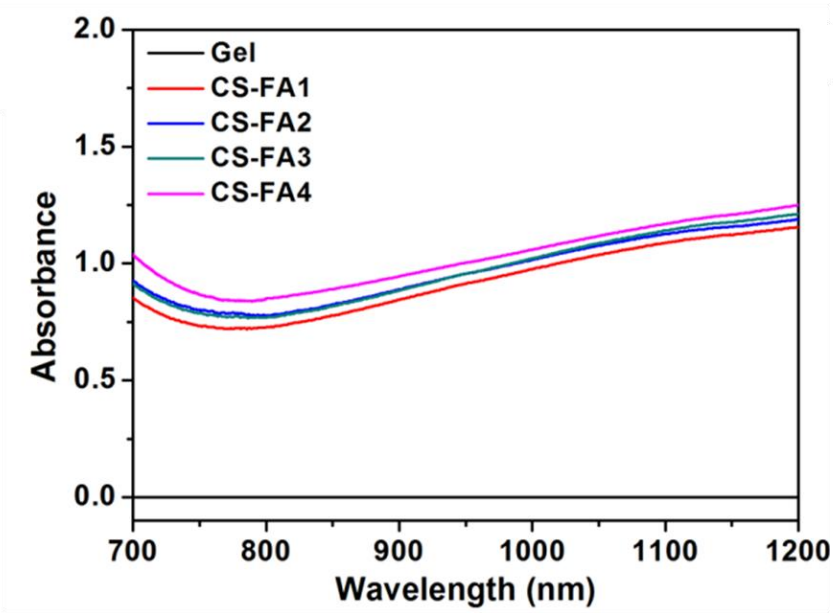

Fig. 3.3. UV spectra of Gel, CS-FA1, CS-FA2, CS-FA3 and CS-FA4 scaffolds

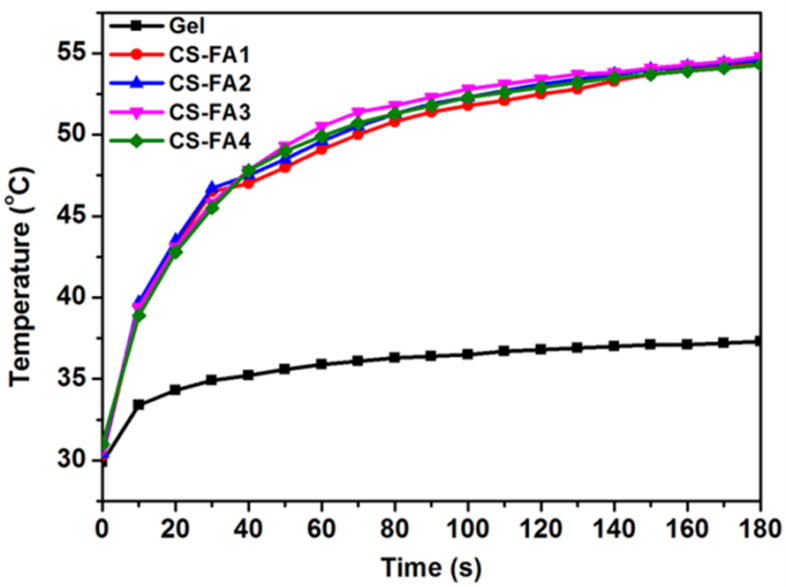

Figure 3.4. Temperature-heating time curves (b) of Gel, CS-FA1, CS-FA2, CS-FA3 and CS-FA4 scaffolds.

3.4.4 FA amount in Gel/Fe_3O_4-FA composite scaffolds

The amount of FA in each composite scaffold was measured by detecting FA absorbance of scaffold digestion solution after dissolving the scaffolds and removing iron ions from the digestion solution (Figure 3.5). The typical absorption peaks of FA are located at 274 and 365 nm.[47, 48] The spectra showed that the composite scaffolds without incorporation of FA had no absorption near 365 nm. However, after introducing FA, the absorption peaks near 274 and 365 nm appeared and the absorbance intensity of the Gel/Fe_3O_4-FA

composite scaffolds increased with the increasing of FA amount. A UV-Vis calibration curve for FA has been drawn according to the FA concentration *versus* the absorption value at 365 nm (Fig. 3.6). Based on the calibration curve, the FA amount in the Gel/Fe_3O_4-FA composite scaffolds was calculated to be 88.0 ± 9.0 μg, 223.7 ± 22.6 μg, 325.3 ± 1.2 μg and 517.4 ± 129.7 μg for CS-FA1, CS-FA2, CS-FA3 and CS-FA4, respectively. According to the theoretical value of free amino groups in the composite scaffolds, the reaction efficiency was 30.8 ± 4.9%, 39.1 ± 2.2%, 30.6 ± 1.4% and 30.5 ± 3.8% for CS-FA1, CS-FA2, CS-FA3 and CS-FA4, respectively. The feed ratio of FA to free amino groups was kept at the same and therefore the reaction efficiency of FA to the free amino acid group was almost at the same level. The results indicated that the incorporated FA amount could be controlled by the free amino groups in the scaffolds, which could be regulated by the incorporated PLL amount in the scaffolds.

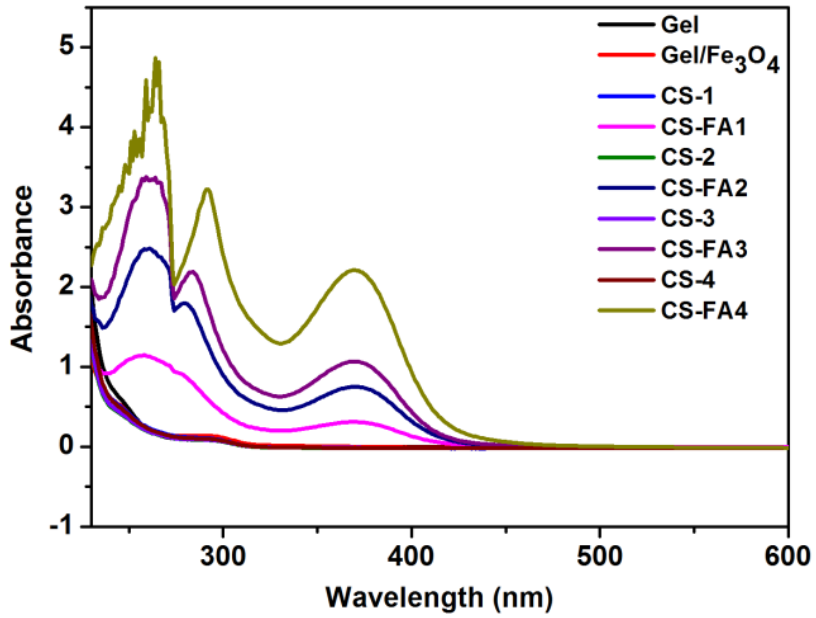

Figure 3.5. UV spectra of Gel, Gel/Fe_3O_4, CS-1, CS-2, CS-3 and CS-4, CS-FA1, CS-FA2, CS-FA3 and CS-FA4 scaffolds after dissolution in an alkaline solution and removal of iron ions.

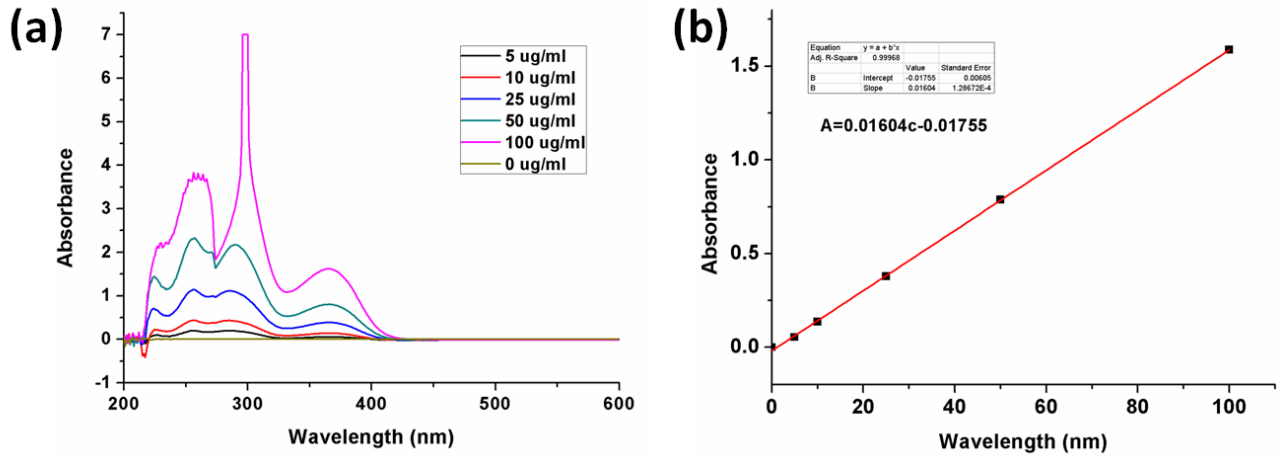

Fig. 3.6. UV spectra of FA solution with different FA concentration(a). Calibration curve of FA according to the FA concentration *versus* the absorption value at 365 nm (b).

3.4.5 Cancer cell capture and quantification

HeLa cells were seeded and cultured in the Gel, Gel/Fe_3O_4 and Gel/Fe_3O_4-FA composite scaffolds for 30 min. DAPI staining showed the distribution of captured HeLa cells in the scaffolds (Figure 3.7a). The cells were captured by the pore structures in the scaffolds. More cells were observed in the Gel/Fe_3O_4-FA composite scaffolds than were in the Gel and Gel/Fe_3O_4 composite scaffolds. Furthermore, the number of captured cells was counted (Figure 3.7b). There were some cells adhered in the Gel and Gel/Fe_3O_4 scaffolds. The cell adhesion cites such as RGD sequence in gelatin molecules could support cell adhesion. There was no significant difference between the cell number in Gel scaffold and Gel/Fe_3O_4 composite scaffolds. Due to the positive charge of PLL, introduction of PLL slightly enhanced cell adhesion. Introduction of FA in the scaffolds significantly increased the captured cell number. The captured cell number in Gel/Fe_3O_4-FA composite scaffolds was significantly higher than the captured cell number in Gel scaffold and Gel/Fe_3O_4 scaffolds. Furthermore the captured cell number in Gel/Fe_3O_4-FA composite scaffolds increased with the increasing of FA amount until saturation. CS-4, CS-3 composite scaffolds possessed the same highest captured cell number, which indicated that the capture efficiency would not increase if the FA amount continued to increase after saturation.

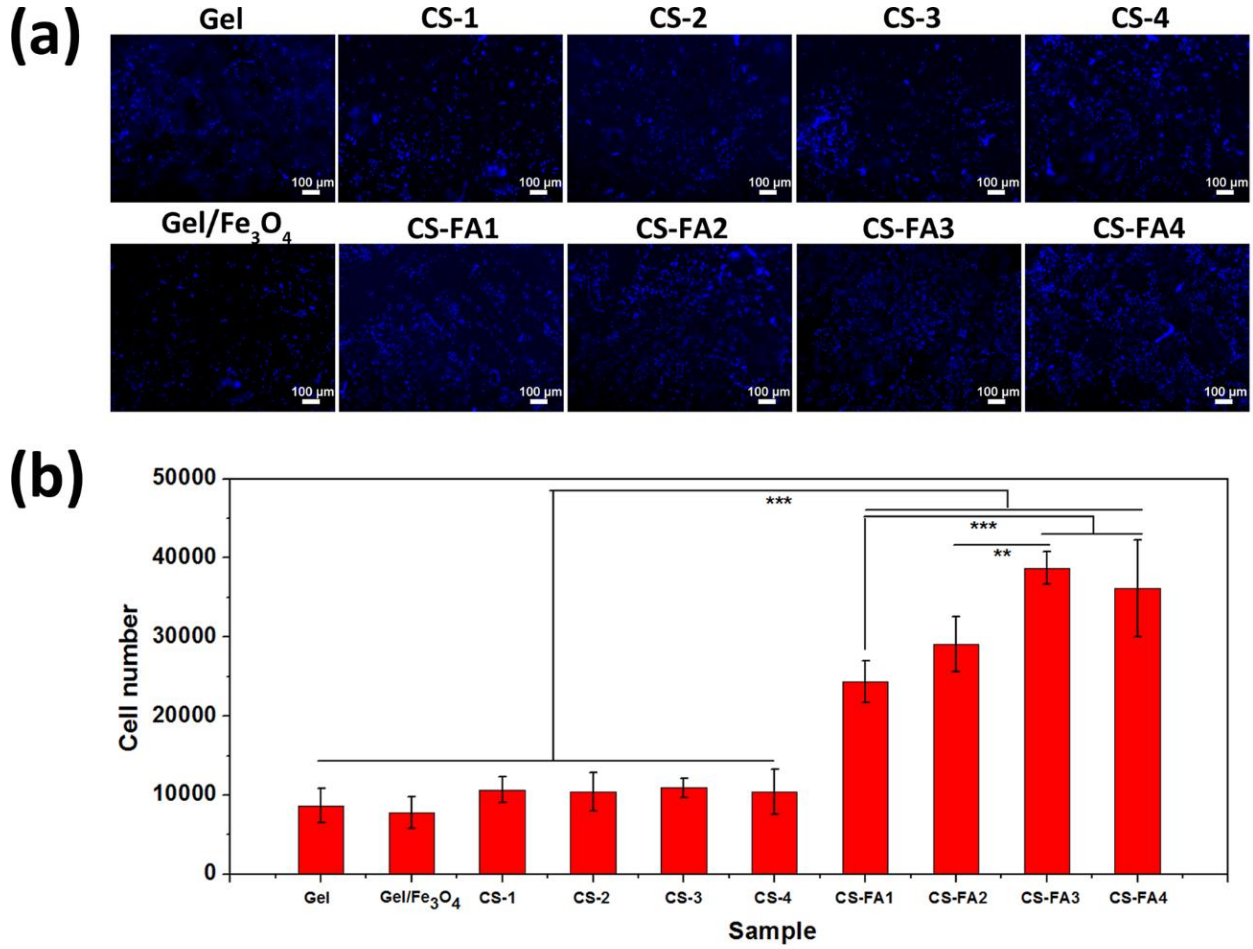

Fig. 3.7. DAPI staining (a) and quantified cell number (b) of the Gel, Gel/Fe_3O_4, CS-1, CS-2, CS-3, CS-4, CS-FA1, CS-FA2, CS-FA3 and CS-FA4 scaffolds after incubation with HeLa cells for 30 min.

3.4.6 *In vitro* photothermal ablation of cancer cells

The killing effect of the composite scaffolds was confirmed by measuring cell viability without and with laser irradiation (Figure 3.8). Without laser irradiation, cell viability in Gel, CS-FA1 and CS-FA2 scaffolds showed no significant difference and all of them possessed quite high cell viability. However, the cell viability significantly decreased in CS-FA3 and further decreased in CS-FA4, which should be due to the high PLL amount in CS-FA3 and CS-FA4. PLL has been reported to have some cytotoxicity to the cells.[49, 50] To confirm cytotoxicity of introduced PLL in the composite scaffolds, cell viability of Gel, Gel/Fe_3O_4, CS-1, CS-2, CS-3 and CS-4 scaffolds was also measured and compared (Figure 3.9). The results showed that incorporation of Fe_3O_4 nanoparticles in the scaffolds did not cause obvious cytotoxicity. However cell viability decreased with the increasing PLL amount in the composite scaffolds. Therefore, too high PLL amount in the composite scaffolds was not desirable because of its cytotoxicity. After laser irradiation for 3 min, most of the cells in the Gel/Fe_3O_4-FA composite scaffolds were dead. Cell viability in the CS-FA1, CS-FA2, CS-FA3 and CS-FA4 was 0.8 ± 0.4%, 1.2 ± 1.8%, 0.7 ± 1.2% and 1.2 ± 1.2%, respectively. However cell viability in Gel scaffold was not significantly different from that without laser irradiation. The results indicated that the Gel/Fe_3O_4-FA composite scaffolds possessed excellent cancer cell ablation ability. The well controlled pore structures of the composite scaffolds facilitated cell penetration and access to the pores of the scaffolds. The FA ligands on the pore surfaces of Gel/Fe_3O_4-FA composite scaffolds helped to effectively capture cancers when the cells entered the scaffolds. Fe_3O_4 nanoparticles in the Gel/Fe_3O_4-FA composite scaffolds could efficiently transfer the energy for laser irradiation to heat to kill the captured cancer cells. The multifunctional composite scaffolds should be useful for photothermal cancer therapy.

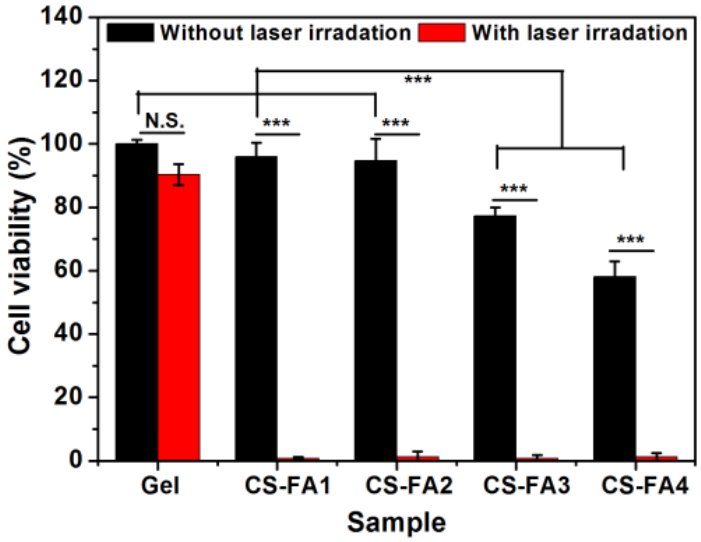

Fig. 3.8. Cell viability of HeLa cells in the Gel scaffolds and Gel/Fe_3O_4-FA composite scaffolds without or with 3 min laser irradiation.

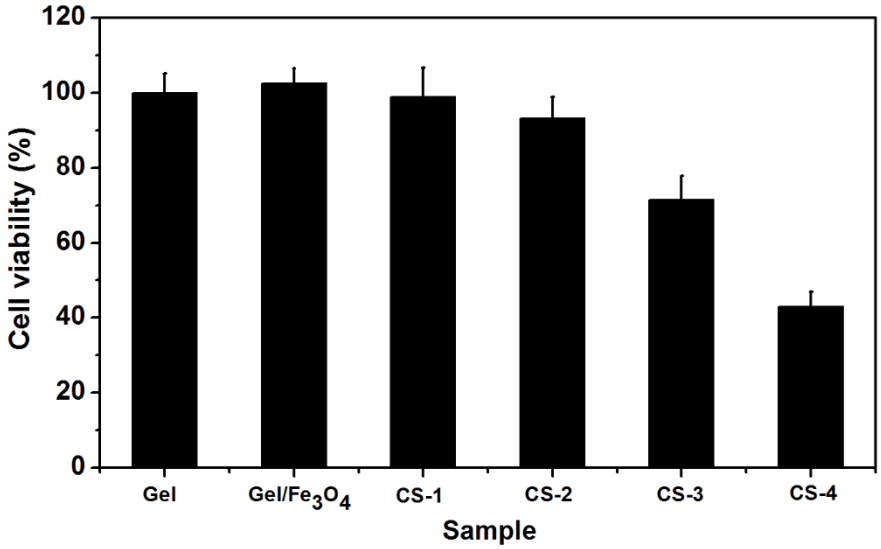

Fig. 3.9. Cell viability of HeLa cells on Gel, Gel/Fe_3O_4, CS-1, CS-2, CS-3 and CS-4 without laser irradiation.

3.5 Conclusions

In summary, a multifunctional Gel/Fe_3O_4-FA composite scaffold for cancer cell capture and photothermal ablation was successfully prepared. The pore structures were controlled by using pre-prepared ice particulates. By adjusting the fed PLL amount, the number of free amino groups in the composite scaffolds could be easily modulated. The targeting ligand, FA, was immobilized in the Gel/Fe_3O_4 composite scaffolds by reaction with the free amino groups in the scaffolds to obtain Gel/Fe_3O_4-FA composite scaffold with different FA grafting density. The Gel/Fe_3O_4-FA composite scaffold could efficiently capture cancer cells and the captured cell number significantly increased with the increasing FA amount in the composite scaffolds. The composite scaffolds showed good photothermal conversion efficiency and could efficiently kill the cancer cell during NIR laser irradiation. The results should be important for the design and preparation of biomaterials and scaffolds for effective photothermal cancer therapy and tissue regeneration.

3.6 References

1. Kim, J.; Park, S.; Lee, J. E.; Jin, S. M.; Lee, J. H.; Lee, I. S.; Yang, I.; Kim, J. S.; Kim, S. K.; Cho, M. H. Designed fabrication of multifunctional magnetic gold nanoshells and their application to magnetic resonance imaging and photothermal therapy. *Angew. Chem., Int. Ed.* 2006, 118, 7918-7922.
2. Markovic, Z. M.; Harhaji-Trajkovic, L. M.; Todorovic-Markovic, B. M.; Kepić, D. P.; Arsikin, K. M.; Jovanović, S. P.; Pantovic, A. C.; Dramićanin, M. D.; Trajkovic, V. S. *In vitro* comparison of the photothermal anticancer activity of graphene nanoparticles and carbon nanotubes. *Biomaterials* 2011, 32, 1121-1129.
3. Kim, J.; Kim, J.; Jeong, C.; Kim, W. J. Synergistic nanomedicine by combined gene and photothermal therapy. *Adv. Drug Delivery Rev.* 2016, 98, 99-112.
4. Shen, S.; Wang, S.; Zheng, R.; Zhu, X.; Jiang, X.; Fu, D.; Yang, W. Magnetic nanoparticle clusters for

photothermal therapy with near-infrared irradiation. *Biomaterials* 2015, 39, 67-74.

5. Wang, X.; Wang, C.; Cheng, L.; Lee, S.-T.; Liu, Z. Noble metal coated single-walled carbon nanotubes for applications in surface enhanced raman scattering imaging and photothermal therapy. *J. Am. Chem. Soc.* 2012, 134, 7414-7422.

6. Moon, H. K.; Lee, S. H.; Choi, H. C. *In vivo* near-infrared mediated tumor destruction by photothermal effect of carbon nanotubes. *ACS Nano* 2009, 3, 3707-3713.

7. Zhou, F.; Wu, S.; Wu, B.; Chen, W. R.; Xing, D. Mitochondria-targeting single-walled carbon nanotubes for cancer photothermal therapy. *Small* 2011, 7, 2727-2735.

8. Li, J.; Cai, R.; Kawazoe, N.; Chen, G. Facile preparation of albumin-stabilized gold nanostars for the targeted photothermal ablation of cancer cells. *J. Mater. Chem. B* 2015, 3, 5806-5814.

9. Zhang, J.; Liu, G.; He, F.; Chen, L.; Huang, Y. Au@Cu_7S_4 yolk-shell nanoparticles as a 980 nm laser-driven photothermal agent with a heat conversion efficiency of 63%. *RSC Adv.* 2015, 5, 87903-87907.

10. Yang, K.; Zhang, S.; Zhang, G.; Sun, X.; Lee, S.-T.; Liu, Z. Graphene in mice: ultrahigh *in vivo* tumor uptake and efficient photothermal therapy. *Nano Lett.* 2010, 10, 3318-3323.

11. Chu, M.; Shao, Y.; Peng, J.; Dai, X.; Li, H.; Wu, Q.; Shi, D. Near-infrared laser light mediated cancer therapy by photothermal effect of Fe_3O_4 magnetic nanoparticles. *Biomaterials* 2013, 34, 4078-4088.

12. Chen, H.; Burnett, J.; Zhang, F.; Zhang, J.; Paholak, H.; Sun, D. Highly crystallized iron oxide nanoparticles as effective and biodegradable mediators for photothermal cancer therapy. *J. Mater. Chem. B* 2014, 2, 757-765.

13. Zhou, Z.; Sun, Y.; Shen, J.; Wei, J.; Yu, C.; Kong, B.; Liu, W.; Yang, H.; Yang, S.; Wang, W. Iron/iron oxide core/shell nanoparticles for magnetic targeting MRI and near-infrared photothermal therapy. *Biomaterials* 2014, 35, 7470-7478.

14. Shen, S.; Kong, F.; Guo, X.; Wu, L.; Shen, H.; Xie, M.; Wang, X.; Jin, Y.; Ge, Y. CMCTS stabilized Fe_3O_4 particles with extremely low toxicity as highly efficient near-infrared photothermal agents for *in vivo* tumor ablation. *Nanoscale* 2013, 5, 8056-8066.

15. Mao, H.; Li, J.; Dulińska-Molak, I.; Kawazoe, N.; Takeda, Y.; Mamiya, H.; Chen, G. Cellular effects of magnetic nanoparticles explored by atomic force microscopy. *Biomater. Sci.* 2015, 3, 1284-1290.

16. Huang, C.; Soenen, S. J.; Rejman, J.; Trekker, J.; Chengxun, L.; Lagae, L.; Ceelen, W.; Wilhelm, C.; Demeester, J.; De Smedt, S. C. Magnetic electrospun fibers for cancer therapy. *Adv. Funct. Mater.* 2012, 22, 2479-2486.

17. Hsiao, C.-W.; Chuang, E.-Y.; Chen, H.-L.; Wan, D.; Korupalli, C.; Liao, Z.-X.; Chiu, Y.-L.; Chia, W.-T.; Lin, K.-J.; Sung, H.-W. Photothermal tumor ablation in mice with repeated therapy sessions using NIR-absorbing micellar hydrogels formed in situ. *Biomaterials* 2015, 56, 26-35.

18. Huang, W.-C.; Chen, S.-H.; Chiang, W.-H.; Huang, C.-W.; Lo, C.-L.; Chern, C.-S.; Chiu, H.-C. Tumor microenvironment-responsive nanoparticle delivery of chemotherapy for enhanced selective cellular uptake and transportation within tumor. *Biomacromolecules* 2016.

19. You, J.; Cao, J.; Zhao, Y.; Zhang, L.; Zhou, J.; Chen, Y. Improved mechanical properties and sustained release behavior of cationic cellulose nanocrystals reinforeced cationic cellulose injectable hydrogels. *Biomacromolecules* 2016, 17, 2839-2848.

20. Wang, S.; Chen, Y.; Li, X.; Gao, W.; Zhang, L.; Liu, J.; Zheng, Y.; Chen, H.; Shi, J. Injectable 2D MoS_2-integrated drug delivering implant for highly efficient NIR-triggered synergistic tumor hyperthermia. *Adv. Mater.* 2015, 27, 7117-7122.

21. Kim, Y. J.; Ebara, M.; Aoyagi, T. A smart hyperthermia nanofiber with switchable drug release for inducing cancer apoptosis. *Adv. Funct. Mater.* 2013, 23, 5753-5761.

22. Zhang, Z.; Liu, S.; Xiong, H.; Jing, X.; Xie, Z.; Chen, X.; Huang, Y. Electrospun PLA/MWCNTs composite nanofibers for combined chemo- and photothermal therapy. *Acta Biomater.* 2015, 26, 115-123.
23. GhavamiNejad, A.; Sasikala, A. R. K.; Unnithan, A. R.; Thomas, R. G.; Jeong, Y. Y.; Vatankhah‐Varnoosfaderani, M.; Stadler, F. J.; Park, C. H.; Kim, C. S. Mussel‐inspired electrospun smart magnetic nanofibers for hyperthermic chemotherapy. *Adv. Funct. Mater.* 2015, 25, 2867-2875.
24. Zhang, Y.; Zhai, D.; Xu, M.; Yao, Q.; Chang, J.; Wu, C. 3D-printed bioceramic scaffolds with a Fe_3O_4/graphene oxide nanocomposite interface for hyperthermia therapy of bone tumor cells. *J. Mater. Chem. B* 2016, 4, 2874-2886.
25. Lin, T.-C.; Lin, F.-H.; Lin, J.-C. In Vitro Feasibility Study of The Use of A magnetic electrospun chitosan nanofiber composite for hyperthermia treatment of tumor cells. *Acta Biomater.* 2012, 8, 2704-2711.
26. Chen, Y.; Jiang, L.; Wang, R.; Lu, M.; Zhang, Q.; Zhou, Y.; Wang, Z.; Lu, G.; Liang, P.; Ran, H. Injectable smart phase-transformation implants for highly efficient *in vivo* magnetic-hyperthermia regression of tumors. *Adv. Mater.* 2014, 26, 7468-7473.
27. Zhang, J.; Li, J.; Chen, S.; Kawazoe, N.; Chen, G. Preparation of gelatin/Fe_3O_4 composite scaffolds for enhanced and repeatable cancer cell ablation. *J. Mater. Chem. B* 2016, 4, 5664-5672.
28. Zhang, J.; Li, J.; Kawazoe, N.; Chen, G. Composite scaffolds of gelatin and gold nanoparticles with tunable size and shape for photothermal cancer therapy. *J. Mater. Chem. B* 2016, DOI: 10.1039/C6TB02872A.
29. Xing, R.; Liu, K.; Jiao, T.; Zhang, N.; Ma, K.; Zhang, R.; Zou, Q.; Ma, G.; Yan, X. An injectable self-assembling collagen-gold hybrid hydrogel for combinatorial antitumor photothermal/photodynamic therapy. *Adv. Mater.* 2016, 28, 3669-3676.
30. Zhang, J.; Zhao, S.; Zhu, M.; Zhu, Y.; Zhang, Y.; Liu, Z.; Zhang, C. 3D-printed magnetic Fe_3O_4/MBG/PCL composite scaffolds with multifunctionality of bone regeneration, local anticancer drug delivery and hyperthermia. *J. Mater. Chem. B* 2014, 2, 7583-7595.
31. Ma, H.; Jiang, C.; Zhai, D.; Luo, Y.; Chen, Y.; Lv, F.; Yi, Z.; Deng, Y.; Wang, J.; Chang, J. A bifunctional biomaterial with photothermal effect for tumor therapy and bone regeneration. *Adv. Funct. Mater.* 2016, 26, 1197-1208.
32. Ma, H.; Luo, J.; Sun, Z.; Xia, L.; Shi, M.; Liu, M.; Chang, J.; Wu, C. 3D printing of biomaterials with mussel-inspired nanostructures for tumor therapy and tissue regeneration. *Biomaterials* 2016, 111, 138-148.
33. Chen, Y.; Cao, W.; Zhou, J.; Pidhatika, B.; Xiong, B.; Huang, L.; Tian, Q.; Shu, Y.; Wen, W.; Hsing, I.-M. Poly(l-lysine)-graft-folic acid-coupled poly (2-methyl-2-oxazoline)(PLL-g-PMOXA-c--a): a bioactive copolymer for specific targeting to rolate receptor-positive cancer cells. *ACS Appl. Mater. Interfaces* 2015, 7, 2919-2930.
34. Feng, X.; Zhang, S.; Wu, H.; Lou, X. A novel folic acid-conjugated TiO_2-SiO_2 photosensitizer for cancer targeting in photodynamic therapy. *Colloids Surf., B* 2015, 125, 197-205.
35. Salem, M.; Xia, Y.; Allan, A.; Rohani, S.; Gillies, E. R. Curcumin-loaded, folic acid-functionalized magnetite particles for targeted drug delivery. *RSC Adv.* 2015, 5, 37521-37532.
36. Zhou, B.; Yang, J.; Peng, C.; Zhu, J.; Tang, Y.; Zhu, X.; Shen, M.; Zhang, G.; Shi, X. PEGylated polyethylenimine-entrapped gold nanoparticles modified with folic acid for targeted tumor CT imaging. *Colloids Surf., B* 2016, 140, 489-496.
37. Wang, C. E.; Wei, H.; Tan, N.; Boydston, A. J.; Pun, S. H. Sunflower polymers for folate-mediated drug delivery. *Biomacromolecules* 2015, 17, 69-75.
38. Jones, S. K.; Lizzio, V.; Merkel, O. M. Folate receptor targeted delivery of siRNA and paclitaxel to ovarian cancer cells via folate conjugated triblock copolymer to overcome TLR4 driven chemotherapy

resistance. *Biomacromolecules* 2015, 17, 76-87.

39. Li, J.; Hu, Y.; Yang, J.; Sun, W.; Cai, H.; Wei, P.; Sun, Y.; Zhang, G.; Shi, X.; Shen, M. Facile synthesis of folic acid-functionalized iron oxide nanoparticles with ultrahigh relaxivity for targeted tumor MR imaging. *J. Mater. Chem. B* 2015, 3, 5720-5730.

40. Zhang, Q.; Lu, H.; Kawazoe, N.; Chen, G. Pore size effect of collagen scaffolds on cartilage regeneration. *Acta Biomater.* 2014, 10, 2005-2013.

41. Chen, S.; Zhang, Q.; Nakamoto, T.; Kawazoe, N.; Chen, G. Gelatin scaffolds with controlled pore structure and mechanical property for cartilage tissue engineering. *Tissue Eng., Part C* 2016, 22, 189-198.

42. Zhang, Q.; Lu, H.; Kawazoe, N.; Chen, G. Preparation of collagen porous scaffolds with a gradient pore size structure using ice particulates. *Mater. Lett.* 2013, 107, 280-283.

43. Chen, S.; Zhang, Q.; Kawazoe, N.; Chen, G. Effect of high molecular weight hyaluronic acid on chondrocytes cultured in collagen/hyaluronic acid porous scaffolds. *RSC Adv.* 2015, 5, 94405-94410.

44. Huang, P.; Bao, L.; Zhang, C.; Lin, J.; Luo, T.; Yang, D.; He, M.; Li, Z.; Gao, G.; Gao, B. Folic acid-conjugated silica-modified gold nanorods for X-ray/CT imaging-guided dual-mode radiation and photo-thermal therapy. *Biomaterials* 2011, 32, 9796-9809.

45. Zhang, Y.; Kohler, N.; Zhang, M. Surface modification of superparamagnetic magnetite nanoparticles and their intracellular uptake. *Biomaterials* 2002, 23, 1553-1561.

46. Zhou, J.; Romero, G.; Rojas, E.; Ma, L.; Moya, S.; Gao, C. Layer by layer chitosan/alginate coatings on poly(Lactide-Co-Glycolide) nanoparticles for antifouling protection and folic acid binding to achieve selective cell targeting. *J. Colloid Interface Sci.* 2010, 345, 241-247.

47. Dántola, M. L.; Denofrio, M. P.; Zurbano, B.; Gimenez, C. S.; Ogilby, P. R.; Lorente, C.; Thomas, A. H. Mechanism of photooxidation of folic acid sensitized by unconjugated pterins. *Photochem. Photobiol. Sci.* 2010, 9, 1604-1612.

48. Hong, X.; Wang, Z.; Yang, J.; Zheng, Q.; Zong, S.; Sheng, Y.; Zhu, D.; Tang, C.; Cui, Y. Silylated bodipy dyes and their use in dye-encapsulated silica nanoparticles with switchable emitting wavelengths for cellular imaging. *Analyst* 2012, 137, 4140-4149.

49. Fischer, D.; Li, Y.; Ahlemeyer, B.; Krieglstein, J.; Kissel, T. *In vitro* cytotoxicity testing of polycations: influence of polymer structure on cell viability and hemolysis. *Biomaterials* 2003, 24, 1121-1131.

50. Symonds, P.; Murray, J. C.; Hunter, A. C.; Debska, G.; Szewczyk, A.; Moghimi, S. M. Low and high molecular weight poly(l-Lysine)/poly (l-Lysine) DNA complexes initiate mitochondrial-mediated apoptosis differently. *FEBS Lett.* 2005, 579, 6191-6198.

Chapter 4

Composite scaffolds of gelatin and gold nanoparticles with tunable size and shape for photothermal cancer therapy

4.1 Summary

Photothermal therapy (PTT) has been extensively investigated as a promising strategy for cancer therapy. For successful application of this technique, various nanomaterials have been explored as photothermal conversion agents. Gold nanoparticles (AuNPs), especially Au nanorods and Au nanostars have received much attention for photothermal therapy because of their facile preparation and high photothermal conversion efficiency. Due to the limited accumulation and easy diffusion of free nanoparticles, incorporation of nanoparticles in scaffolds for direct implantation has been demonstrated as an attractive way for cancer therapy application. In this study, composite porous scaffolds of gelatin and AuNPs were prepared by introducing Au nanorods and nanostars with an average size around 35.0, 65.0 and 115.0 nm in gelatin scaffolds. The composite scaffolds were used for localized PTT application of cancer cells. Gel/AuNP composite scaffolds supported cell adhesion and showed good biocompatibility. Temperature in the composite scaffolds increased quickly upon NIR laser irradiation. The photothermal efficiency and cancer cell killing efficiency were dependent on the shape, size and amount of AuNPs in the composite scaffolds. The composite scaffold prepared with 65.0 nm Au nanorods showed the highest photothermal efficiency and cell killing efficiency. The results indicated the importance of shape and size modulation of AuNPs for photothermal therapy application.

4.2 Introduction

Cancer is one of the leading causes of death in the world.[1, 2] Current cancer therapies still face some challenges such as cancer recurrence and side effects.[3-5] Recently, photothermal therapy (PTT) has emerged as a novel approach for cancer therapy application. PTT is based on localized heating by utilizing the photothermal conversion agents to absorb near infrared (NIR, 700-1100 nm) light, thereby leading to the destruction of cancer cells.[6] Nowadays, a variety of nanoscaled materials have been reported to be used as PTT agents such as magnetic nanoparticles (NPs),[7-9] copper sulfide NPs,[10-12] molybdenum sulfide nanosheets,[13-15] carbon-based nanomaterials [16-19] and gold-based nanomaterials.[20-24] Among them, gold

nanoparticles (AuNPs) have received increasing attention because of their facile preparation and good photothermal conversion properties. AuNPs with different size and shape can be easily prepared and their surface plasmon resonance (LSPR) peaks are tunable by altering their size and shape.[25, 26] In addition, high photothermal conversion efficiency and good biocompatibility also make them as ideal photothermal conversion agents.[27-29] However, the local and precise delivery of NPs to cancer sites still remains a great challenge. After injection of free NPs, accumulation of AuNPs in tumor sites is very limited and the accumulated NPs can easily diffuse because of their small size.[2, 30] Therefore, developing other effective strategy for localized therapy is highly needed.

Some recent studies have reported immobilization of PTT agents in three-dimensional scaffolds to prepare composite scaffolds for cancer therapy application.[31-34] In such cases, the composite scaffolds can retain the PTT agents in tumor sites at a high amount for a long period, hence achieving repeated local heating without losing photothermal efficiency. [30, 34, 35] Therefore, in this study AuNPs were immobilized in gelatin (Gel) porous scaffolds to prepare Gel/AuNP composite scaffolds to increase localized photothermal therapy. Au nanorod (AuNR) and Au nanostar (AuNS) with different sizes were used to prepare the composite scaffolds because the shape and size of AuNPs may change their LSPR peaks and influence their photothermal efficiency. SEM and UV-Vis were used to investigate the morphology and LSPR peaks of Gel/AuNP composite scaffolds. The photothermal conversion efficiency and cancer cell killing efficiency of the Gel/AuNP composite scaffolds were determined by exposing the scaffolds to a NIR laser. The results showed that the local photothermal efficiency and cancer cell killing efficiency were highly dependent on the shape, size and amount of corresponding AuNPs. Compared with the other composite scaffolds, composite scaffolds immobilized with 65.0 nm AuNR exhibited the superior photothermal efficiency and cancer cell killing efficiency. The results not only highlighted the importance of shape and size modulation on AuNP for PTT application but also indicated the potential to use of this Gel/AuNP composite scaffold as an implantable material for tumor resection. They will provide guidance towards the design and application of efficient photothermal scaffolds for cancer therapy.

4.3 Materials and methods

4.3.1 Materials

Hexadecyltrimethylammonium bromide (CTAB), ascorbic acid (AA), sodium borohydride ($NaBH_4$), silver nitrate ($AgNO_3$), 2-(nmorpholino) ethane sulfonic acid (MES), Eagle's minimun essential medium (EMEM), penicillin, streptomycin, L-glutamine and trypsin/EDTA were purchased from Sigma-Aldrich (St. Louis, MO, USA). Hydrogen tetrachloroaurate tetrahydrate ($HAuCl_4 \cdot 4H_2O$, 99.9%), hydrochloric acid, hydroquinone, trisodium citrate dihydrate ($C_6H_5Na_3O_7 \cdot 2H_2O$,), acetic acid (99.9%), ethanol (99.5%) and N-hydroxysuccinimide (NHS) were purchased from Wako Pure Industries, Ltd (Tokyo, Japan). Fetal bovine serum (FBS) was purchased from Funakoshi Industries (Tokyo, Japan). Porcine derived gelatin was provided by Nitta Gelatin (Osaka, Japan). 1-ethyl-3-(3-dimethylaminopropyl) carbodiimide (EDC) was purchased from Peptide Institute, Inc. (Osaka, Japan). WST-1 reagent was obtained from Roche Molecular Biochemicals (Mannheim, Germany). Cellstain live-dead double staining kit was purchased from Dojindo Laboratories (Kumamoto, Japan). All the chemicals and materials were used as received without further purification. The water in all experiments was purified using a Q-POD Milli-Q water purification system (Millipore Corp., Billerica, MA, USA) with a resistivity of 18.2 MΩ cm.

4.3.2 Preparation of AuNPs with different size and shape

AuNPs with different size (around 35.0 nm, 65.0 nm and 115.0 nm) and shape (AuNR and AuNS) were prepared according to a previous report.[36] Briefly, AuNR35 (R35) and AuNR65 (R65) were synthesized by a seed-mediated growth method and the Au seed solution was prepared by a chemical reduction of $HAuCl_4$ with $NaBH_4$ with CTAB as a stabilizer. The growth solution was prepared by adding 30 mL of 0.01 M $HAuCl_4$, 12 mL of 1.0 M HCl, 1.32 mL or 6.6 mL of 10 mM $AgNO_3$ and 4.8 mL of 0.1 M AA in 600 mL of 0.1 M CTAB solution. 1.44 mL of the Au seed solution was added to the growth solution and the mixture solution was incubated at room temperature for 12 h. By varying the amount of $AgNO_3$, AuNR with diff erent length were formed. AuNR115 (R115) was synthesized by a facile one-pot method. In brief, 22.8 mL of $HAuCl_4$ (0.01 M), 6 mL of $AgNO_3$ (0.02 M) and 4.8 mL of hydroquinone (0.62 M) were sequentially added to 534 mL of CTAB solution (0.11 M) to yield a colorless solution. Subsequently, 378 μL of $NaBH_4$ solution (0.5 M) was added and the resultant mixture was kept standing at 30 ℃ for 24 h. The obtained AuNR were collected by centrifugation and washed with water to remove the free CTAB. The seed-mediated growth method was also used to synthesize AuNS35 (S35), AuNS65 (S65) and AuNS115 (S115). Au seed solution was prepared via a chemical reduction of $HAuCl_4$ by $NaBH_4$ in the presence of trisodium citrate. Subsequently, $HAuCl_4$ solution (30.0 mg mL^{-1}, 2.25 mL), Au seed solution (75, 25 and 3.3 mL), $AgNO_3$ solution (5.0 mg mL^{-1}, 0.9 mL) and AA solution (38.0 mg mL^{-1}, 1.5 mL) was successively dropped into 75 mL water under gentle stirring for 10 min. Usage of different volumes of Au seed solution resulted in AuNS having different diameter. After preparation, AuNR and AuNS solutions were mixed with an aqueous solution of Gel at a concentration of 0.5 (wt/v) % and the resultant solution was stirred at room temperature for 24 h. The gelatin-stabilized AuNPs were then collected by centrifugation, washed with water and re-dispersed in water for further use.

4.3.3 Preparation of Gel/AuNP composite scaffolds

An ice particulate porogen method was used to fabricate the Gel/AuNP composite scaffolds.[37-40] At first, appropriate amount of Gel was dissolved in a 70% acetic acid aqueous solution to obtain an aqueous Gel solution at a concentration of 8.0 (wt/v)%. Subsequently, an aqueous solution of the above prepared AuNPs at a designated concentration was mixed with the aqueous Gel solution under sonication. The final of Au in the mixture solution was adjusted to 1.0 mM, 2.0 mM and 4.0 mM. The final concentration of Gel in the mixture solution was adjusted to 4.0 (wt/v)%. The mixture solution was placed in low temperature chamber at -4 ^{o}C for 40 min for temperature balance before mixture with ice particulates.

Ice particulates were firstly prepared by spraying pure water into liquid nitrogen according to our previous work.[37-39, 41] Ice particulates were sieved through two sieves having a mesh size of 425 and 500 μm to obtain ice particulates having a diameter range of 425-500 μm. The ice particulates were mixed with the temperature-balanced Gel/AuNP mixture solution at a weight/volume ratio of 7:3 (g/mL) at -4 ^{o}C. Subsequently, the mixture of Gel/AuNP solution and ice particulates was poured into a cooled silicone frame. The entire construct was frozen at -20 ^{o}C for 12 h and then transferred to -80 ^{o}C and kept there for another 4 h. Finally, the entire set was freeze-dried for 3 d.

After freeze-drying, the composite scaffolds were washed with ethanol to remove residual acetic acid. After that, the Gel/AuNP composite scaffolds were cross-linked with 50.0 mM EDC and 20.0 mM NHS dissolved in an ethanol aqueous solution. In order to prevent the dissolution of Gel during cross-linking and to maximize the cross-linking degree, three mixture solvents of ethanol and water with a decreasing ethanol

concentration (ethanol/water (v/v) = 95/5, 90/10 and 85/15) were used. The Gel/AuNR and Gel/AuNPs composite scaffolds were crosslinked sequentially by these three crosslinking solutions for 8 h each. After crosslinking, the composite scaffolds were rinsed with MilliQ water for 6 times and then further treated with 0.1 M glycine for 6 h. Finally, the Gel/AuNP composite scaffolds were washed with water and freeze-dried for 2 d. Porous Gel scaffold was also prepared at the same conditions without adding AuNR or AuNS. The Gel/AuNR and Gel/AuNS composite scaffolds prepared with AuNPs having an average diameter of around 35.0 nm, 65.0 nm and 115.0 nm were denoted as Gel/R35, Gel/R65, Gel/R115, Gel/S35, Gel/S65 and Gel/S115, respectively.

4.3.4 Characterization techniques

The morphology of AuNR and AuNS was observed by transmission electron microscopy (TEM, JEOL 2011F, Japan) with an operation voltage of 200 kV. Dynamic light scattering (DLS, ELSZ-2000, Japan) was used to measure the hydrodynamic size of the AuNPs. The pore structure of Gel scaffold, Gel/AuNR and Gel/AuNS composite scaffolds was investigated by a scanning electron microscope (SEM, Hitachi S-4800, Japan). The AuNP size was measured from TEM images by an Image J software. At least 100 AuNPs were measured for size analysis. UV-visible absorption spectra of the Gel, Gel/AuNR and Gel/AuNS scaffolds and the AuNPs aqueous solutions were recorded using a UV-2600 UV-visible spectrophotometer (Shimazu Corp., Japan).

4.3.5 Photothermal efficiency of Gel/AuNP composite scaffolds

The Gel/AuNP composite scaffolds and control Gel scaffold were cut into discs having a dimension of 5.0 × 3.0 × 1.0 mm. Each of the scaffold discs was hydrated with 20 μL culture medium (EMEM) and was exposed to a NIR laser (805 nm, Thorlabs Inc., USA) with a power density of 1.6 W cm^{-2} for 180 s. A digital thermometer (AS ONE Corp., Japan) was used to measure the temperature of the samples every 10 s during laser irradiation.

4.3.6 Cell culture in composite scaffolds

Human cervical carcinoma cell line (HeLa cells) were seeded in 75 cm^2 tissue culture flasks and cultured in EMEM medium supplemented with 10% FBS, penicillin (100 U mL^{-1}) and streptomycin (100 μg mL^{-1}) in 5% CO_2 incubator at 37 ^oC in a humidified environment. The cells were passaged using a 0.05% trypsin-EDTA solution after reaching confluence.

Before cell seeding, Gel and Gel/AuNP composite scaffolds were cut into discs (5.0 × 3.0 × 1.0 mm), sterilized with 70% ethanol aqueous solution for 40 min, washed with PBS for 5 times and immersed into culture medium at 37 ^oC for 6 h. After removing the culture medium by using a sterile tissue paper, 1×10^5 HeLa cells were seeded into each scaffold. After 5 h of incubation, the cell/scaffold constructs were transferred into 6-well plates and cultured in 5 mL medium in 5% CO_2 incubator at 37 ^oC.

4.3.7 Cell adhesion in composite scaffolds

After being cultured for 1 d, cells in Gel and Gel/AuNP composite scaffold were fixed with 2.5% glutaraldehyde at room temperature for 2 h. And then the cell/scaffold constructs were washed with MilliQ

water thoroughly, frozen and freeze-dried. SEM was used to observe cell adhesion and distribution in the scaffolds.

4.3.8 Photothermal ablation of HeLa cells in composite scaffolds

After 1 d culture, the cell/scaffold constructs were divided into two groups (without or with laser irradiation). For laser irradiation group, the cell/scaffold constructs were taken from the culture dishes and exposed to the NIR laser (805 nm) for 180 s. The samples without laser irradiation were also taken out from incubator for 180 s to exclude environmental effects on cell viability. After laser irradiation, the cell/scaffold constructs were cultured for another 5 h. And then cell viability was determined by WST-1 assay. The absorbance at 440 nm was measured by a microplate reader (Benchmark Plus, Bio-Rad, Hercules, CA, USA). Every three samples were used for the measurement to calculate the average and standard deviation. Live/dead staining was conducted with a cellstain live-dead double staining kit to determine the live and dead cells in the scaffolds without or with NIR irradiation. The cell/scaffold constructs were washed twice with PBS and incubated in serum-free EMEM medium containing calcein AM and propidium iodide (PI) for 15 min. After staining, the samples were observed under a fluorescent microscope (Olympus, Japan).

4.3.9 Statistical analysis

All of the data were presented as mean ± standard deviation (SD). Statistical analysis was performed using a one-way analysis of variance with Tukey's *post hoc* test for multiple comparisons. A value of $p < 0.05$ was considered to indicate a statistically significant difference.

4.4 Results and Discussion

4.4.1 Morphology of AuNPs

The morphology and UV-Vis spectra of AuNR and AuNS with different diameter are shown in Fig.4.1. TEM images showed that the AuNR and AuNS had rod-like and star-like structures. The size of the three AuNR was (35.0 ± 6.2) × (20.4 ± 3.1), (65.9 ± 6.6) × (13.2 ± 2.2) and (117.1 ± 11.5 nm) × (27.4 ± 5.8 nm) in length × width, respectively. The size of the three AuNS was 37.0 ± 7.8, 66.6 ± 13.0 and 115.1 ± 24.4 nm, respectively. The size of the three types of AuNR and AuNS was controlled at around 35, 65 and 115 nm. Most of the AuNPs were found to be distributed homogeneously, which indicated the good stability of gelatin-stabilized AuNR and AuNS. The hydrodynamic size of R35, R65 and R115 was 35.6 ± 0.6 nm, 64.8 ± 14.8 nm and 132.4 ± 9.5 nm, respectively. The hydrodynamic size of S35, S65 and S115 was 70.0 ± 7.0 nm, 101.4 ± 5.4 nm and 139.1 ± 8.1 nm, respectively. The hydrodynamic size of AuNPs was slightly bigger than that measured from TEM, which may be due to partial aggregation of AuNPs. UV-Vis spectra of AuNPs with different size and shape are shown in Fig. 1g and h. The absorption spectra of AuNR possessed two LSPR peaks, which was due to the different size in transverse and longitudinal directions of AuNR. R35, R65 and R115 displayed a strong longitudinal absorption peak at 611, 833 and 880 nm, respectively. AuNS showed abroad LSPR peak around 800 nm. The absorption peak of R65, R115, S35, S65 and S115 was located in the NIR region, which indicated that they should be useful for photothermal therapy.

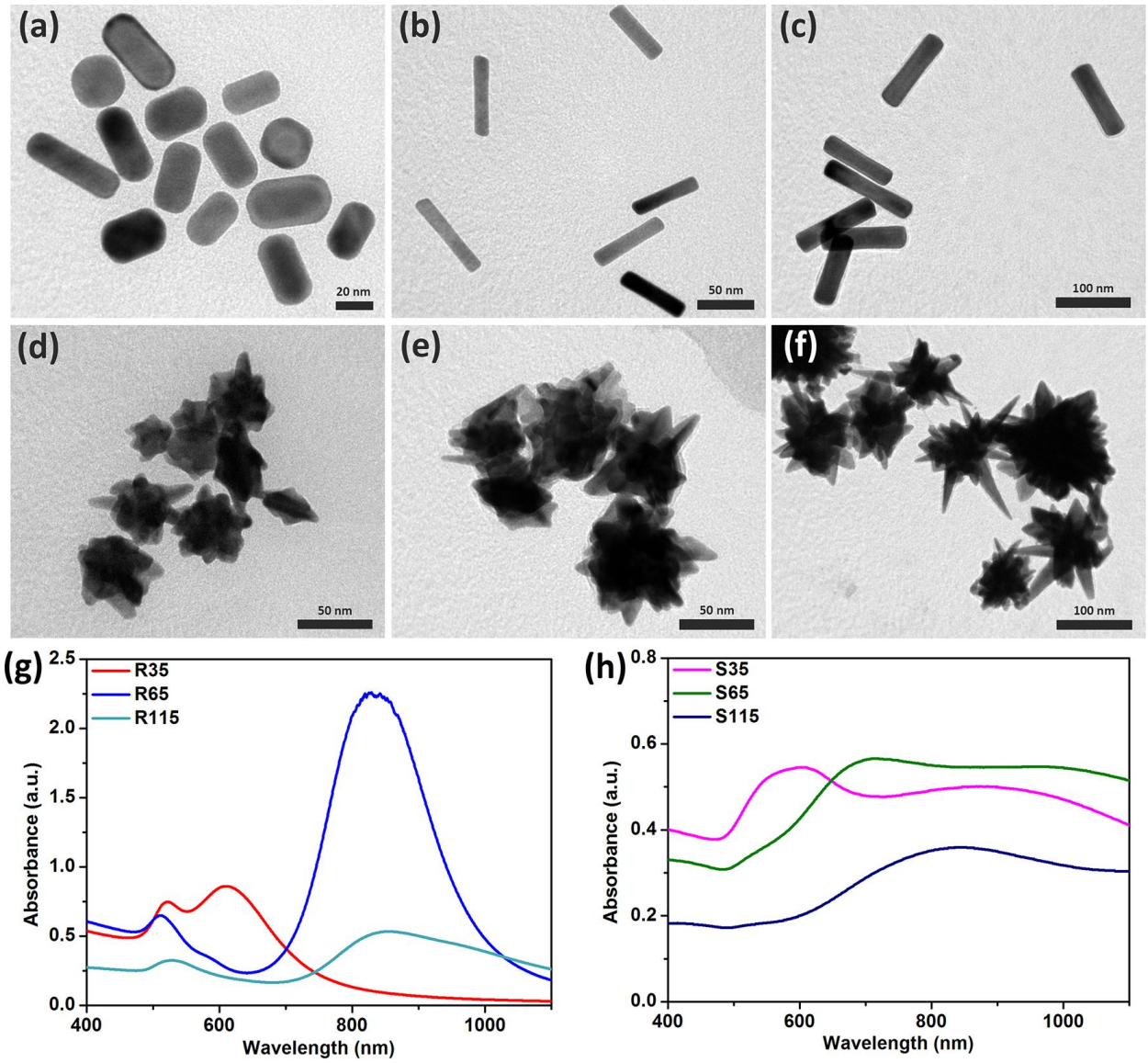

Fig. 4.1. TEM image of AuNR and AuNS: (a) Rod35, (b) Rod65, (c) Rod115, (d) Star35, (e) Star65 and (f) Star115. UV-Vis spectra of AuNR (g) and AuNS (h) in pure water.

4.4.2 Porous structure of Gel and Gel/AuNP composite scaffolds

The porous structure of Gel and Gel/AuNP composite scaffolds was observed by SEM (Fig. 4.2). Gel scaffold and Gel/AuNP composite scaffolds showed almost the same pore structure, which was consisted of spherical large pores and interconnected small pores. The size of large pores was almost equal to the size of ice particulates (425 ~ 500 μm) used as porogen. Formation of interconnected small pores was attributed to the newly formed ice crystals that formed during freezing process. The well interconnected pore structure should be beneficial for penetration and spatial distribution of cells throughout the scaffolds. Gross appearance of the corresponding composite scaffolds showed different color depending on the size, shape and amount of AuNPs. The color of composite scaffolds was similar to that of the corresponding aqueous

solution of AuNPs (Fig. 4.3). The color of composite scaffolds became darker when the amount of AuNP in the scaffolds increased.

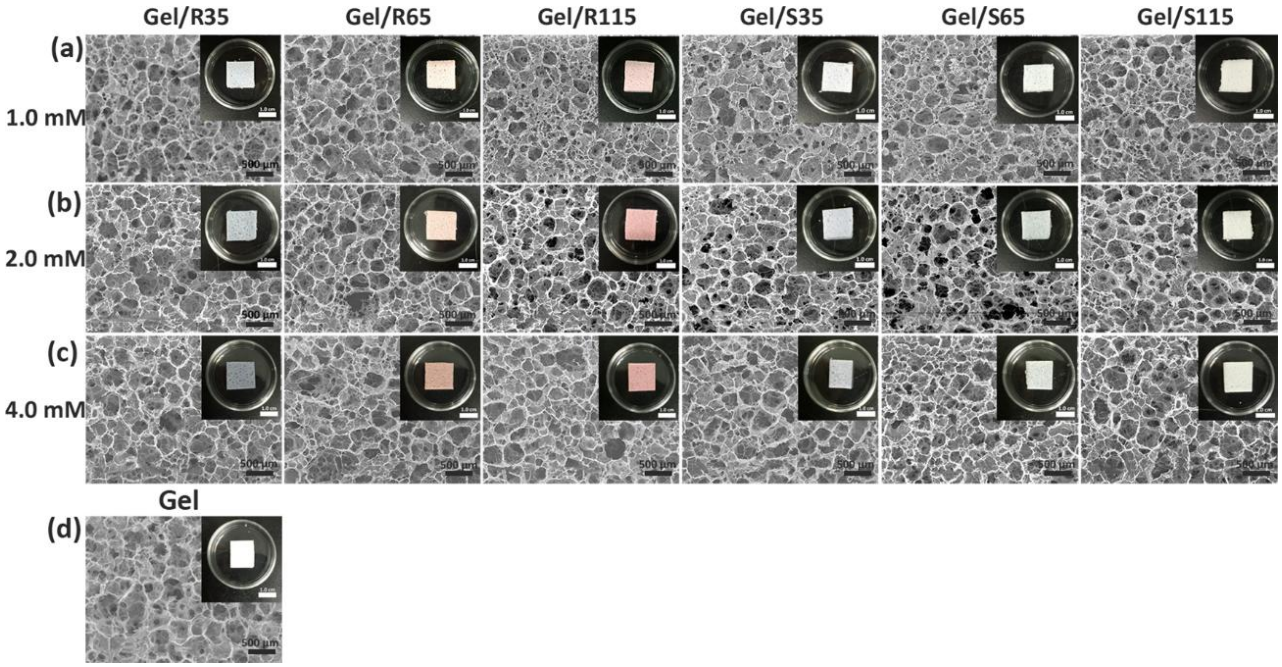

Fig. 4.2. SEM images of Gel/R35, Gel/R65, Gel/R115, Gel/S35, Gel/S65 and Gel/S115 composite scaffolds prepared with different Au concentration of (a) 1.0 mM, (b) 2.0 mM, (c) 4.0 mM and (d) control Gel scaffold. The inserts are gross appearance of the corresponding composite scaffolds.

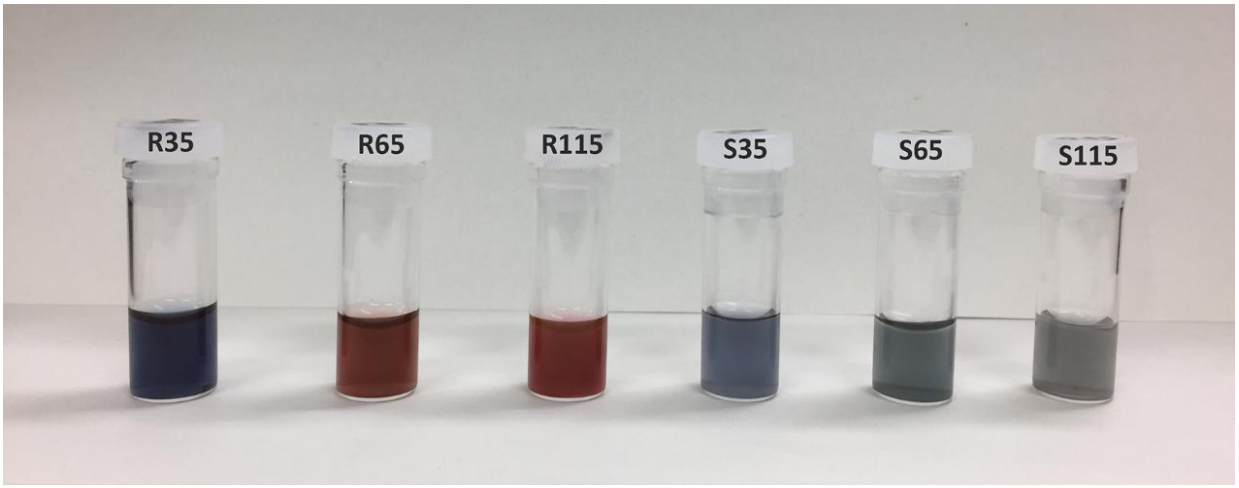

Fig. 4.3. Gross appearance of R35, R65, R115, S35, S65 and S115.

High magnification SEM images (Fig. 4.4) of Gel/AuNP composite scaffolds showed that the pore surface became rougher after introduction of AuNPs. AuNR and AuNS were distributed homogenously on the walls of composite scaffolds and more AuNPs were observed with increasing AuNPs amount. Furthermore, single AuNR or AuNS was visible on the pore surface at a further high magnification. The results indicated that AuNR and AuNS could be homogenously dispersed in the composite scaffolds without aggregation. The homogenous distribution of AuNPs in the composite scaffolds could heat the scaffolds

evenly to avoid the localized over-heating resulted from nanoparticle aggregation.

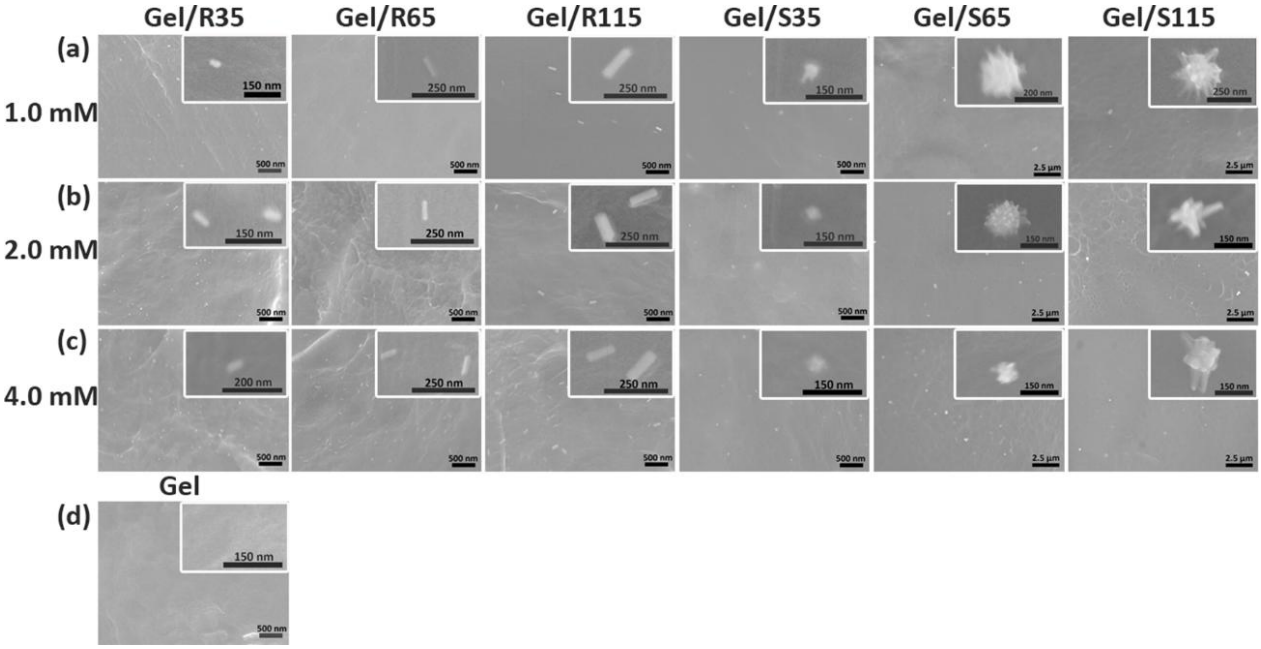

Fig. 4.4. Surface morphology of Gel/R35, Gel/R65, Gel/R115, Gel/S35, Gel/S65 and Gel/S115 composite scaffolds prepared with different Au concentration of (a) 1.0 mM, (b) 2.0 mM, (c) 4.0 mM and (d) control Gel scaffold. The inserts are high magnification SEM images of the corresponding scaffolds.

4.4.3 Photothermal conversion efficiency of Gel/AuNP composite scaffold

Photothermal conversion effect of Gel/AuNP composite scaffold was investigated by exposing the scaffolds to an 805 nm laser. The photothermal conversion effect of the different types of composite scaffolds was compared by the same concentration of Au used to prepare the composite scaffolds (Fig. 4.5a-c). Temperature in the composite scaffolds during NIR laser irradiation increased with the irradiation time and Au concentration. Temperature change was also deeply dependent on the size and shape of AuNPs (Table 4.1). Gel/R65 composite scaffold showed the highest heating efficiency compared with the other five types of composite scaffolds. Heating efficiency of the composite scaffolds was an order of Gel/R65 > Gel/S65 > Gel/S35 > Gel/S115 > Gel/R115 ≈ Gel/R35. The heating efficiency of the scaffolds should be related to their NIR absorption properties. The UV-Vis absorption spectra of the solid phase Gel and Gel/AuNP composite scaffolds were measured to show their absorption properties in NIR region (Fig. 4.5d-e). The absorption peak of composite scaffolds showed a slight red-shift as compared with their corresponding aqueous solution of AuNPs. There may be two reasons for the highest photothermal efficiency of Gel/R65. One is that the LSPR peak of Gel/R65 well matched to the common used irradiation wavelength for photothermal therapy. The other reason may be that the intensity of Gel/R65 UV-Vis absorption spectrum was higher than the other composite scaffolds, indicating the good heating effect of Gel/R65.

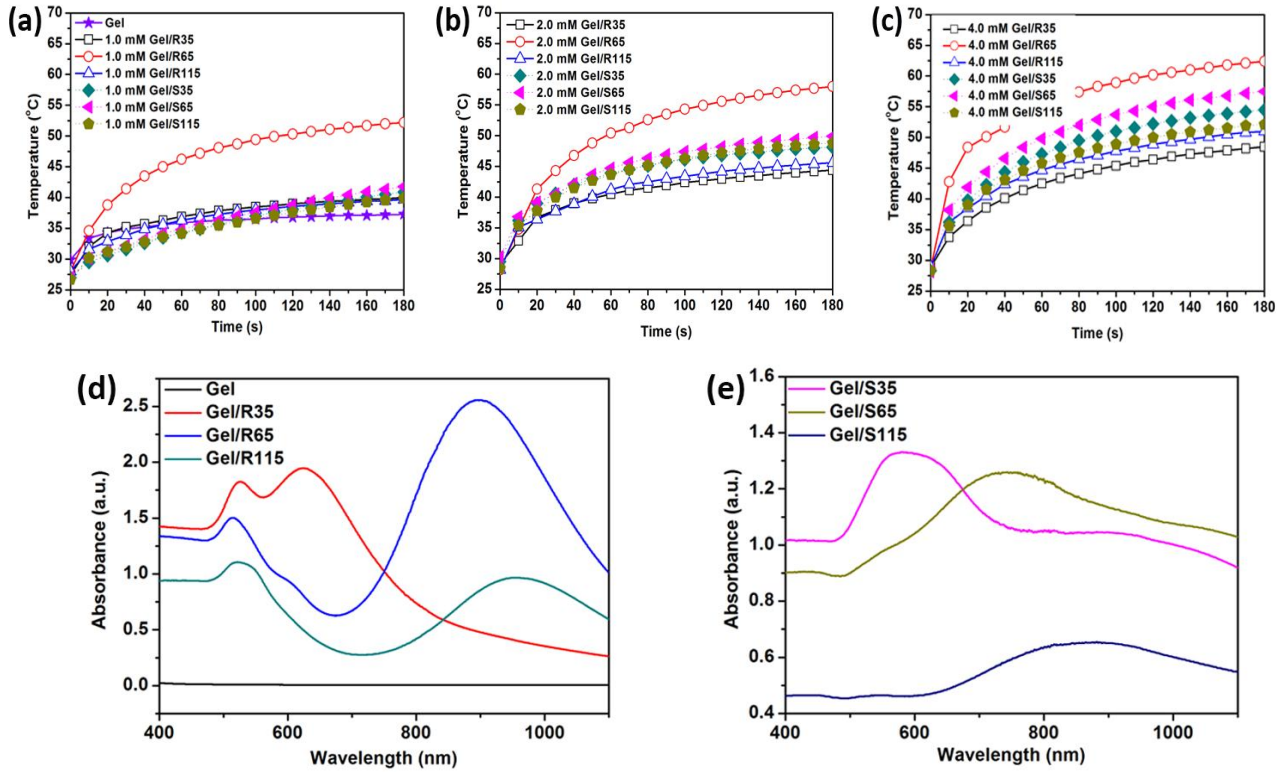

Fig. 4.5. Temperature-time curves of Gel/R35, Gel/R65, Gel/R115, Gel/S35, Gel/S65 and Gel/S115 composite scaffolds prepared with different Au concentration of (a) 1.0 mM, (b) 2.0 mM and (c) 4.0 mM. The scaffolds were exposed to an 805 nm laser for 180 s. Temperature-time curve of Gel scaffold is also shown in (a). UV-Vis spectra of Gel/AuNR composite scaffolds (d) and Gel/AuNS composite scaffolds (e).

Table 4.1. Temperature change (^{o}C) of Gel and Gel/AuNP composite scaffolds after 180 s laser irradiation. Data represent mean ± SD.

Sample	0.0 mM	1.0 mM	2.0 mM	4.0 mM
Gel/R35	—	13.2 ± 1.6	16.8 ± 2.1	20.5 ± 1.3
Gel/R65	—	24.2 ± 0.9	29.8 ± 0.5	33.3 ± 1.4
Gel/R115	—	12.5 ± 0.7	17.6 ± 1.8	20.6 ± 1.4
Gel/S35	—	16.3 ± 0.2	20.0 ± 0.8	25.8 ± 1.9
Gel/S65	—	17.8 ± 1.3	21.5 ± 1.2	27.6 ± 0.7
Gel/S115	—	14.3 ± 1.8	18.6 ± 0.9	23.2 ± 1.6
Gel	7.4 ± 0.8	—	—	—

4.4.4 Cell attachment in Gel/AuNP composite scaffolds

HeLa cells were seeded in Gel and Gel/AuNP composite scaffolds to examine cell attachment. HeLa cells showed homogeneous distribution throughout Gel scaffold and Gel/AuNP composite scaffolds (Fig. 4.6). The homogeneous cell distribution should be due to the interconnected pore structures of Gel and

Gel/AuNP composite scaffolds. High magnification images showed that many cells spread and had pseudopodia, which indicated cells could well adhere on the walls of Gel scaffold and Gel/AuNP composite scaffolds. Incorporation of AuNPs with different size and shape did not show obvious influence on cell adhesion, indicating the good biocompatibility of the Gel/AuNP composite scaffolds. Unlike free AuNPs in culture medium, the AuNR or AuNS were embedded in the gelatin matrices of the composite scaffolds. The coated gelatin layer improved the biocompatibility of composite scaffolds.[42]

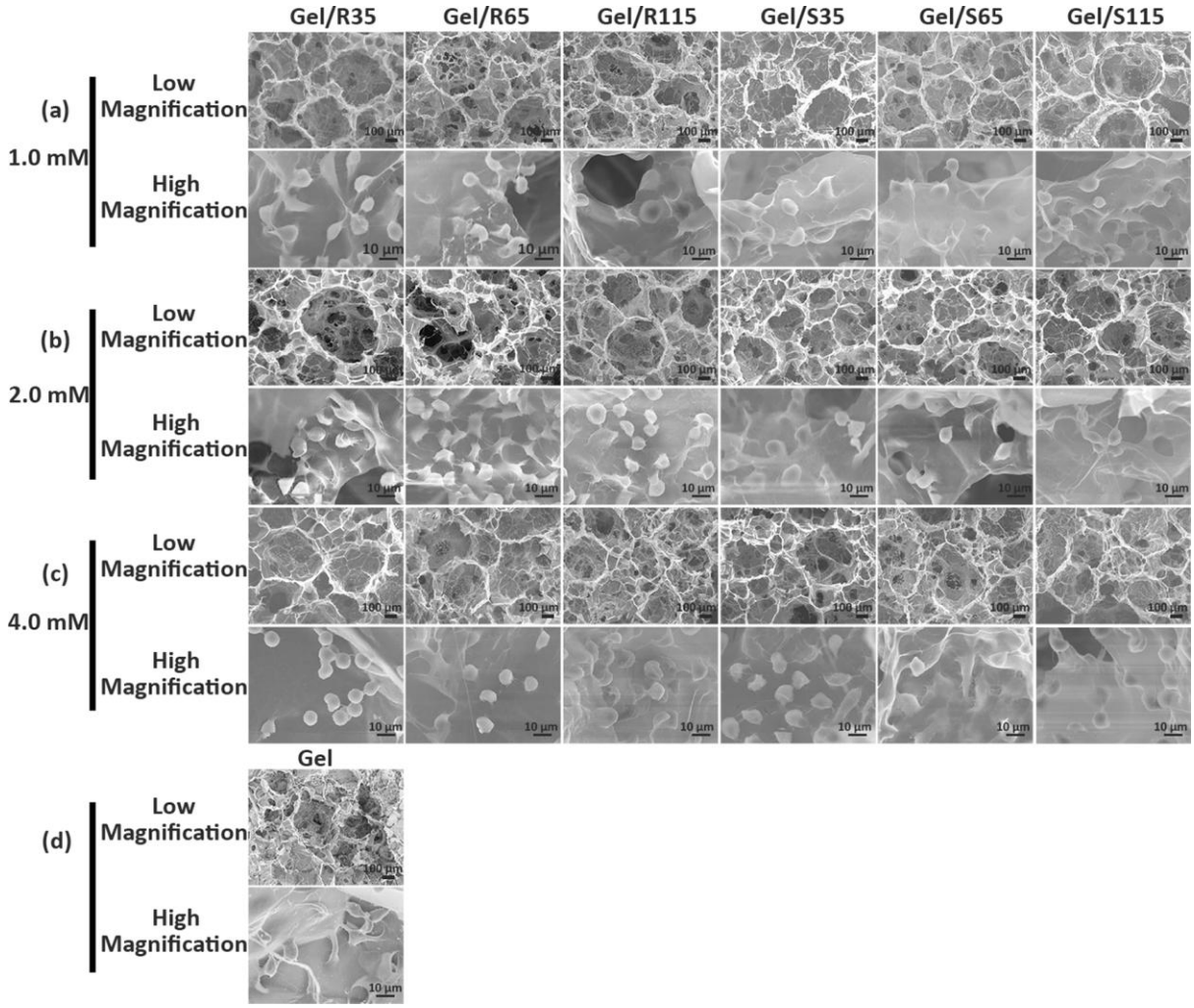

Fig. 4.6. SEM images of Gel/R35, Gel/R65, Gel/R115, Gel/S35, Gel/S65 and Gel/S115 composite scaffolds prepared with different Au concentration of (a) 1.0 mM, (b) 2.0 mM, (c) 4.0 mM and (d) control Gel scaffold after 1 d cell culture.

4.4.5 Photothermal ablation of HeLa cells

In order to investigate photothermal ablation of Gel/AuNP composite scaffolds on HeLa cells, cell/scaffold constructs were exposed to an NIR laser for 180 s. WST-1 was used to quantify the cell viability (Fig. 4.7). Without laser irradiation, cells in the Gel scaffold and Gel/AuNP composite scaffolds showed very high cell viability at almost the same level. When the cell/scaffold constructs were exposed to NIR laser irradiation, cell viability in the control Gel scaffold showed no significant change compared with that without laser irradiation (Fig. 4.7b). The result indicated that cellular viability in Gel scaffold did not change because

Gel scaffold had no photothermal therapy capability. Cell viability in Gel/R35, Gel/R115, Gel/S35, Gel/S65 and Gel/S115 composite scaffolds decreased a little and in Gel/R65 scaffolds decreased from 97.6 ± 1.1% to 32.3 ± 7.5% after laser irradiation when the Au concentration was 1.0 mM. Increasing the Au concentration to 2.0 mM, cell viability of all the Gel/AuNP scaffolds significantly decreased and cell viability of Gel/R65 decreased to 0.4 ± 0.2%. The cell viability further decreased when the Au concentration increased to 4.0 mM. Cell viability in Gel/R35, Gel/R65, Gel/R115, Gel/S35, Gel/S65 and Gel/S115 composite scaffolds prepared at 4.0 mM of Au were 45.5 ± 8.2%, 0.2 ± 0.2%, 38.2 ± 6.4%, 20.1 ± 6.4%, 11.0 ± 3.9% and 34.9 ± 1.9%, respectively. The results indicated killing efficiency of Gel/AuNP composite scaffolds had an order of Gel/R65 > Gel/S65 > Gel/S35 > Gel/S115 > Gel/R115 > Gel/R35.

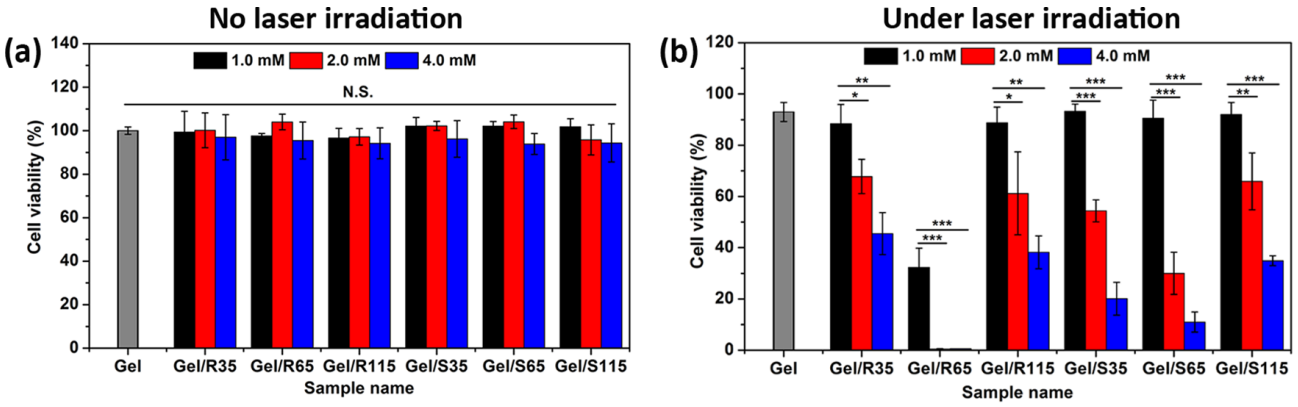

Fig. 4.7. Viability of HeLa cells in Gel, Gel/R35, Gel/R65, Gel/R115, Gel/S35, Gel/S65 and Gel/S115 composite scaffolds without (a) or with (b) laser irradiation for 180 s. The data are presented as mean ± SD values. N.S., no significant difference, * $p < 0.05$, ** $p < 0.01$ and *** $p < 0.001$

Live/dead staining was conducted to visualize the cell viability in scaffolds without or with laser irradiation. As shown in Fig. 4.8, almost no dead cells (indicated by red fluorescence) was observed in the scaffolds before laser irradiation. However, upon exposure to NIR laser, live cell number in Gel/AuNP composite scaffolds decreased. More and more dead cells were observed as the Au concentration in composite scaffolds increased. Especially, for the Gel/R65 composite scaffold, almost all the cancer cells were killed when the Au concentration was 2.0 mM. Furthermore, when the Au concentration was 4.0 mM, most of cancer cells in Gel/S65 and Gel/S35 scaffolds were killed after laser irradiation. The live/dead staining results were well consistent with the WST-1 results. The cancer cell killing efficiency was in the same order of the photothermal heating efficiency. The higher heating efficiency resulted in higher temperature raising to kill more cells. The Gel/R65 had the highest photothermal conversion efficiency and highest cancer cell ablation effect.

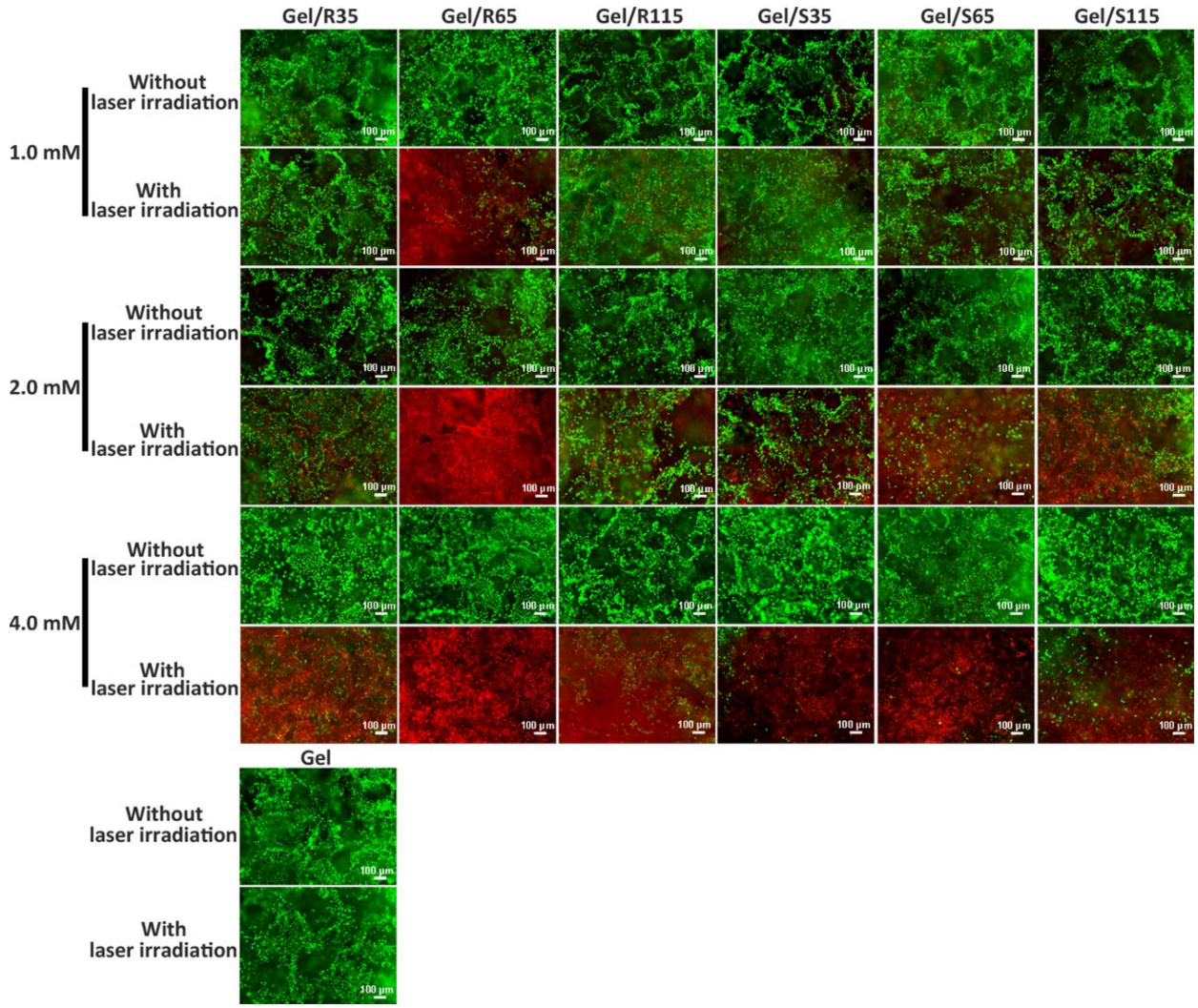

Fig. 4.8. Live/dead staining of HeLa cells in the Gel, Gel/R35, Gel/R65, Gel/R115, Gel/S35, Gel/S65 and Gel/S115 composite scaffolds without or with laser irradiation for 180 s.

4.5 Conclusions

AuNPs with tunable shape (nanorod and nanostar) and size (35.0, 65.0 and 115.0 nm) were incorporated into porous gelatin scaffold to function as localized PTT agents. All the Gel/AuNP composite scaffolds showed good biocompatibility. Local temperature in the composite scaffolds could be quickly elevated under NIR laser irradiation to kill the cells in the scaffolds. The photothermal efficiency and cancer cell killing efficiency of the composite scaffolds were highly dependent on the size and shape of AuNPs. The Gel/R65 composite scaffold showed the highest photothermal efficiency and killing efficiency. The results will be useful for the design and fabrication of efficient photothermal scaffolds for cancer therapy.

4.6 References

1. Zhang, Y.; Zhai, D.; Xu, M.; Yao, Q.; Chang, J.; Wu, C., 3D-printed bioceramic scaffolds with a Fe_3O_4/graphene oxide nanocomposite interface for hyperthermia therapy of bone tumor cells. *J. Mater. Chem. B* **2016,** 4, (17), 2874-2886.
2. Huang, C.; Soenen, S. J.; Rejman, J.; Trekker, J.; Chengxun, L.; Lagae, L.; Ceelen, W.; Wilhelm, C.; Demeester, J.; De Smedt, S. C., Magnetic electrospun fibers for cancer therapy. *Adv. Funct. Mater.* **2012,** 22, (12), 2479-2486.
3. Bird, J. E., Advances in the surgical management of bone tumors. *Curr Oncol Rep* **2014,** 16, (7), 1-6.
4. DeVita, V. T.; Chu, E., A history of cancer chemotherapy. *Cancer Res* **2008,** 68, (21), 8643-8653.
5. Baskar, R.; Lee, K. A.; Yeo, R.; Yeoh, K.-W., Cancer and radiation therapy: current advances and future directions. *Int J Med Sci* **2012,** 9, (3), 193-199.
6. Kim, J.; Park, S.; Lee, J. E.; Jin, S. M.; Lee, J. H.; Lee, I. S.; Yang, I.; Kim, J. S.; Kim, S. K.; Cho, M. H., Designed fabrication of multifunctional magnetic gold nanoshells and their application to magnetic resonance imaging and photothermal therapy. *Angew. Chem. Int. Ed.* **2006,** 118, (46), 7918-7922.
7. Shen, S.; Kong, F.; Guo, X.; Wu, L.; Shen, H.; Xie, M.; Wang, X.; Jin, Y.; Ge, Y., CMCTS stabilized Fe_3O_4 particles with extremely low toxicity as highly efficient near-infrared photothermal agents for in vivo tumor ablation. *Nanoscale* **2013,** 5, (17), 8056-8066.
8. Song, X.; Gong, H.; Yin, S.; Cheng, L.; Wang, C.; Li, Z.; Li, Y.; Wang, X.; Liu, G.; Liu, Z., Ultra-small iron oxide doped polypyrrole nanoparticles for *in vivo* multimodal imaging guided photothermal therapy. *Adv. Funct. Mater.* **2014,** 24, (9), 1194-1201.
9. Zhou, Z.; Sun, Y.; Shen, J.; Wei, J.; Yu, C.; Kong, B.; Liu, W.; Yang, H.; Yang, S.; Wang, W., Iron/iron oxide core/shell nanoparticles for magnetic targeting MRI and near-infrared photothermal therapy. *Biomaterials* **2014,** 35, (26), 7470-7478.
10. Zhou, M.; Zhang, R.; Huang, M.; Lu, W.; Song, S.; Melancon, M. P.; Tian, M.; Liang, D.; Li, C., A chelator-free multifunctional [64Cu] CuS nanoparticle platform for simultaneous micro-PET/CT imaging and photothermal ablation therapy. *J. Am. Chem. Soc.* **2010,** 132, (43), 15351-15358.
11. Hessel, C. M.; Pattani, V. P.; Rasch, M.; Panthani, M. G.; Koo, B.; Tunnell, J. W.; Korgel, B. A., Copper selenide nanocrystals for photothermal therapy. *Nano Lett.* **2011,** 11, (6), 2560-2566.
12. Mohamed, M. S.; Poulose, A. C.; Veeranarayanan, S.; Aburto, R. R.; Mitcham, T.; Suzuki, Y.; Sakamoto, Y.; Ajayan, P. M.; Bouchard, R. R.; Yoshida, Y., Plasmonic fluorescent CdSe/Cu 2 S hybrid nanocrystals for multichannel imaging and cancer directed photo-thermal therapy. *Nanoscale* **2016,** 8, (15), 7876-7888.
13. Tan, L.; Wang, S.; Xu, K.; Liu, T.; Liang, P.; Niu, M.; Fu, C.; Shao, H.; Yu, J.; Ma, T., Layered MoS_2 hollow spheres for highly-efficient photothermal therapy of rabbit liver orthotopic transplantation tumors. *Small* **2016,** 12, (15), 2046–2055.
14. Liu, T.; Shi, S.; Liang, C.; Shen, S.; Cheng, L.; Wang, C.; Song, X.; Goel, S.; Barnhart, T. E.; Cai, W., Iron oxide decorated MoS2 nanosheets with double PEGylation for chelator-free radiolabeling and multimodal imaging guided photothermal therapy. *ACS Nano* **2015,** 9, (1), 950-960.
15. Wang, J.; Tan, X.; Pang, X.; Liu, L.; Tan, F.; Li, N., MoS_2 quantum dot@ polyaniline inorganic–organic nanohybrids for *in vivo* dual-modal imaging guided synergistic photothermal/radiation therapy. *ACS Appl. Mater. Interfaces* **2016,** 8, (37), 24331-24338.

16. Wang, X.; Wang, C.; Cheng, L.; Lee, S.-T.; Liu, Z., Noble metal coated single-walled carbon nanotubes for applications in surface enhanced Raman scattering imaging and photothermal therapy. *J. Am. Chem. Soc.* **2012,** 134, (17), 7414-7422.
17. Wang, Y.-W.; Fu, Y.-Y.; Peng, Q.; Guo, S.-S.; Liu, G.; Li, J.; Yang, H.-H.; Chen, G.-N., Dye-enhanced graphene oxide for photothermal therapy and photoacoustic imaging. *J. Mater. Chem. B* **2013,** 1, (42), 5762-5767.
18. Chen, Y.-W.; Su, Y.-L.; Hu, S.-H.; Chen, S.-Y., Functionalized graphene nanocomposites for enhancing photothermal therapy in tumor treatment. *Adv. Drug Delivery Rev.* **2016,** 105, 190–204.
19. Zhang, B.; Wang, H.; Shen, S.; She, X.; Shi, W.; Chen, J.; Zhang, Q.; Hu, Y.; Pang, Z.; Jiang, X., Fibrin-targeting peptide CREKA-conjugated multi-walled carbon nanotubes for self-amplified photothermal therapy of tumor. *Biomaterials* **2016,** 79, 46-55.
20. Li, J.; Cai, R.; Kawazoe, N.; Chen, G., Facile preparation of albumin-stabilized gold nanostars for the targeted photothermal ablation of cancer cells. *J. Mater. Chem. B* **2015,** 3, (28), 5806-5814.
21. Zhang, J.; Liu, G.; He, F.; Chen, L.; Huang, Y., Au@ Cu 7 S 4 yolk–shell nanoparticles as a 980 nm laser-driven photothermal agent with a heat conversion efficiency of 63%. *RSC Adv.* **2015,** 5, (107), 87903-87907.
22. Ali, M. R.; Ali, H. R.; Rankin, C. R.; El-Sayed, M. A., Targeting heat shock protein 70 using gold nanorods enhances cancer cell apoptosis in low dose plasmonic photothermal therapy. *Biomaterials* **2016,** 102, 1-8.
23. Espinosa, A.; Silva, A. K.; Sánchez-Iglesias, A.; Grzelczak, M.; Péchoux, C.; Desboeufs, K.; Liz-Marzán, L. M.; Wilhelm, C., Cancer cell internalization of gold nanostars impacts their photothermal efficiency *in vitro* and *in Vivo*: toward a plasmonic thermal fingerprint in tumoral environment. *Adv. Healthc. Mater.* **2016,** 5, (9), 1040-1048.
24. Li, Z.; Huang, H.; Tang, S.; Li, Y.; Yu, X.-F.; Wang, H.; Li, P.; Sun, Z.; Zhang, H.; Liu, C., Small gold nanorods laden macrophages for enhanced tumor coverage in photothermal therapy. *Biomaterials* **2016,** 74, 144-154.
25. Wang, Y.; Black, K. C.; Luehmann, H.; Li, W.; Zhang, Y.; Cai, X.; Wan, D.; Liu, S.-Y.; Li, M.; Kim, P., Comparison study of gold nanohexapods, nanorods, and nanocages for photothermal cancer treatment. *ACS Nano* **2013,** 7, (3), 2068-2077.
26. Chen, J.; Glaus, C.; Laforest, R.; Zhang, Q.; Yang, M.; Gidding, M.; Welch, M. J.; Xia, Y., Gold nanocages as photothermal transducers for cancer treatment. *Small* **2010,** 6, (7), 811-817.
27. Liu, H.; Chen, D.; Li, L.; Liu, T.; Tan, L.; Wu, X.; Tang, F., Multifunctional gold nanoshells on silica nanorattles: a platform for the combination of photothermal therapy and chemotherapy with low systemic toxicity. *Angew. Chem. Int. Ed.* **2011,** 123, (4), 921-925.
28. Kuo, W.-S.; Chang, Y.-T.; Cho, K.-C.; Chiu, K.-C.; Lien, C.-H.; Yeh, C.-S.; Chen, S.-J., Gold nanomaterials conjugated with indocyanine green for dual-modality photodynamic and photothermal therapy. *Biomaterials* **2012,** 33, (11), 3270-3278.
29. Wang, S.; Huang, P.; Nie, L.; Xing, R.; Liu, D.; Wang, Z.; Lin, J.; Chen, S.; Niu, G.; Lu, G., Single continuous wave laser induced photodynamic/plasmonic photothermal therapy using photosensitizer-functionalized gold nanostars. *Adv. Mater.* **2013,** 25, (22), 3055-3061.
30. Hsiao, C.-W.; Chuang, E.-Y.; Chen, H.-L.; Wan, D.; Korupalli, C.; Liao, Z.-X.; Chiu, Y.-L.; Chia, W.-T.; Lin, K.-J.; Sung, H.-W., Photothermal tumor ablation in mice with repeated therapy sessions using NIR-absorbing micellar hydrogels formed in situ. *Biomaterials* **2015,** 56, 26-35.

31. Ma, H.; Jiang, C.; Zhai, D.; Luo, Y.; Chen, Y.; Lv, F.; Yi, Z.; Deng, Y.; Wang, J.; Chang, J., A bifunctional biomaterial with photothermal effect for tumor therapy and bone regeneration. *Adv. Funct. Mater.* **2016,** 26, (8), 1197-1208.
32. Wang, S.; Chen, Y.; Li, X.; Gao, W.; Zhang, L.; Liu, J.; Zheng, Y.; Chen, H.; Shi, J., Injectable 2D MoS_2-integrated drug delivering implant for highly efficient NIR-triggered synergistic tumor hyperthermia. *Adv. Mater.* **2015,** 27, (44), 7117-7122.
33. Ma, H.; Luo, J.; Sun, Z.; Xia, L.; Shi, M.; Liu, M.; Chang, J.; Wu, C., 3D printing of biomaterials with mussel-inspired nanostructures for tumor therapy and tissue regeneration. *Biomaterials* **2016,** 111, 138-148.
34. Zhang, J.; Li, J.; Chen, S.; Kawazoe, N.; Chen, G., Preparation of gelatin/Fe 3 O 4 composite scaffolds for enhanced and repeatable cancer cell ablation. *J. Mater. Chem. B* **2016,** 4, (34), 5664-5672.
35. Xing, R.; Liu, K.; Jiao, T.; Zhang, N.; Ma, K.; Zhang, R.; Zou, Q.; Ma, G.; Yan, X., An injectable self-Assembling collagen–gold hybrid hydrogel for combinatorial antitumor photothermal/photodynamic therapy. *Adv. Mater.* **2016,** 28, (19), 3669-3676.
36. Li, J.; Zhang, J.; Wang, X.; Kawazoe, N.; Chen, G., Gold nanoparticle size and shape influence on osteogenesis of mesenchymal stem cells. *Nanoscale* **2016,** 8, (15), 7992-8007.
37. Zhang, Q.; Lu, H.; Kawazoe, N.; Chen, G., Preparation of collagen porous scaffolds with a gradient pore size structure using ice particulates. *Mater. Lett.* **2013,** 107, 280-283.
38. Zhang, Q.; Lu, H.; Kawazoe, N.; Chen, G., Pore size effect of collagen scaffolds on cartilage regeneration. *Acta Biomater.* **2014,** 10, (5), 2005-2013.
39. Chen, S.; Zhang, Q.; Nakamoto, T.; Kawazoe, N.; Chen, G., Gelatin scaffolds with controlled pore structure and mechanical property for cartilage tissue engineering. *Tissue Eng Part C Methods* **2016,** 22, (3), 189-198.
40. Chen, S.; Zhang, Q.; Kawazoe, N.; Chen, G., Effect of high molecular weight hyaluronic acid on chondrocytes cultured in collagen/hyaluronic acid porous scaffolds. *RSC Adv.* **2015,** 5, (114), 94405-94410.
41. Mao, H.; Kawazoe, N.; Chen, G., Cell response to single-walled carbon nanotubes in hybrid porous collagen sponges. *Colloids Surf., B* **2015,** 126, 63-69.
42. Li, X.; Chen, S.; Li, J.; Wang, X.; Zhang, J.; Kawazoe, N.; Chen, G., 3D culture of chondrocytes in gelatin hydrogels with different stiffness. *Polymers* **2016,** 8, (8), 269.

Chapter 5

Concluding remarks and future prospects

5.1 Concluding remarks

This thesis summarizes the design and fabrication of porous photothermal scaffolds for photothermal therapy application and investigates the effect of immobilized nanoparicles properties on therapeutic efficacy of implanted photothermal scaffolds.

Chapter 1 introduces some current and new strategies, especially photothermal therapy for cancer therapy. Because of the limitations of free nanoparticles, porous scaffolds were explored as carriers for photothermal therapy application. The requirements, materials and fabrication methods of porous scaffolds were summarized. Finally, the objective of this study was defined.

Chapter 2 describes the preparation of porous gelatin/iron oxide (Gel/Fe_3O_4) composite scaffolds by a facile ice particulates templating method. The Gel/Fe_3O_4 composite scaffolds could elevate the local temperature efficiently during laser irradiation. Cell experiment results demonstrated that the Gel/Fe_3O_4 composite scaffolds had nontoxicity and showed excellent photothermal ablation ability of cancer cells. The composite scaffolds containing 15 wt% Fe_3O_4 nanoparticles could be kill almost all of the cancer cells after 180 s laser irradiation. The Gel/Fe_3O_4 composite also showed the enhanced and repeatable photothermal ablation effect on cancer cells. The results indicated that Gel/Fe_3O_4 composite scaffolds should be useful for photothermal therapy of cancer.

Chapter 3 developed a multifunctional Gel/Fe_3O_4-FA composite scaffold for cancer cell capture and ablation. A typical targeting ligand, folic acid (FA), was immobilized in the composite scaffolds by reaction with the excess amino groups in the scaffolds. By changing the excess amount of amino groups, the Gel/Fe_3O_4-FA composite scaffolds with different FA grafting density were also prepared. Cell capture experiment results showed that the cancer cells could be efficiently captured by Gel/Fe_3O_4-FA composite scaffolds and the captured cell number increased with the increasing FA amount in the composite scaffolds. Moreover, the Gel/Fe_3O_4-FA composite scaffolds also possessed excellent photothermal ablation efficiency. This multifunctional scaffold may provide an attractive way for specifically cancer cell capture and killing and supporting the subsequent cells and tissues regeneration.

Chapter 4 investigates the importance of immobilized nanoparticle size and shape modulation for photothermal therapy. AuNPs with tunable shape (gold nanorod (AuNR) and gold nanostar (AuNS)) and size (35.0, 65.0 and 115.0 nm) were incorporated into porous gelatin scaffold for localized PTT application. The photothermal efficiency and cancer cell killing efficiency of the composite scaffolds were highly dependent on the size and shape of AuNPs. The composite scaffold prepared with 65.0 nm Au nanorods showed the highest photothermal efficiency and cell killing efficiency. All the Gel/AuNS composite scaffolds with different AuNS sizes also had excellent photothermal efficiency and cell killing because of the broad absorption of AuNS in NIR region. The results highlighted the importance of shape and size modulation of AuNPs for PTT and may provide useful information for design and preparation of efficient photothermal scaffolds for cancer therapy.

In conclusion, a few composite porous scaffolds of nanoparticles and gelatin were prepared for PTT application. By using ice particulate as porogen, a well controlled and interconnected pore structure was formed in the composite porous scaffolds. Fe_3O_4 nanoparticles could be easily immobilized in the porous Gel scaffolds by mixing Fe_3O_4 aqueous solution with gelatin solution. The Gel/Fe_3O_4 composite scaffolds possessed excellent local heating efficiency and cancer cell killing efficiency. Moreover, the therapeutic efficacy of Gel/Fe_3O_4 composite scaffolds could be enhanced by repeated heating treatment, which is particularly critical for their application in clinic. In order to improve the specificity to cancer cells, targeting ligand FA was introduced in Gel/Fe_3O_4 composite scaffolds. The multifunctional Gel/Fe_3O_4-FA composite scaffolds could capture cancer cells efficiently and most of cancer cells in the composite scaffolds could be killed during NIR laser irradiation, which indicated excellent therapeutic efficacy of Gel/Fe_3O_4-FA composite scaffolds. Another kind of very useful photothermal conversion agent, AuNP, was also immobilized in Gel scaffolds for PTT application. The effect of AuNPs size and shape on photothermal conversion and cancer cell killing were compared. The results indicated that photothermal efficiency and cancer cell killing efficiency of Gel/AuNP composite scaffolds highly depended on the size and shape of AuNPs. The results indicated the importance of shape and size modulation of AuNPs for photothermal therapy application. This study should contribute to the design and fabrication of efficient photothermal scaffolds for cancer therapy applications.

5.2 Future prospects

Because of the limitations of current therapies for cancer therapy application, the study described in this thesis was mainly focused on the design and fabrication of porous gelatin scaffold with controlled pore structure and photothermal conversion ability for tumor resection. The prepared different kinds of photothermal scaffolds had interconnected pore structure and excellent therapeutic efficacy for cancer cell ablation. Although all these results have proved that the immobilizing PTT agents in porous scaffold is an effective way for cancer therapy, the photothermal scaffolds is still far from clinical application. Therefore, many efforts are still needed to meet the requirements in the clinical cancer therapy application.

The implanted scaffolds should possess the similar mechanical property to the implanted site to sustain the mechanical loading. The mechanical property has been also proved to be an important factor to effect cell phenotype and cell-cell interaction. Due to different mechanical strength of organs, many other kinds of scaffold materials should be developed to prepare photothermal scaffolds. For example, usually, Young's modulus of cortical bone is about 10 GPa , while Young's modulus of scaffolds prepared by natural polymers such as gelatin and collagen are much lower than the bone tissue. Therefore, photothermal scaffolds prepared

by ceramics or synthetic polymer may be suitable to treat the bone tumor. On the other hand, in this thesis, Fe_3O_4 nanoparticles and gold nanoparticles are incorporated into the porous scaffold for PTT application. Some other PTT agents can be also introduced into the porous scaffold by this facile preparation process to meet different application requirements and achieve better cancer cell ablation capacity.

Because the malignant and resistant nature of tumor, it is important to develop effective methods for cancer therapy. The combination of different cancer therapy strategies could achieve better therapeutic efficacy and prevent cancer recurrence. For example, the anti-cancer drugs can be also loaded in the PTT agents and then these drug-loaded PTT agents are introduced into the porous scaffold. These photothermal scaffolds with controlled structure may enable the controlled and sustainable anticancer drug release and also possess photothermal conversion ability. The combination of chemotherapy and PTT could obtain an improved and repeatable effect on tumor resection.

The prepared porous scaffolds in this study focus on their cancer cell killing capability. The normal cells can be also cultured on these scaffolds to investigate normal cell growth, migration, proliferation and differentiation on these composite scaffolds. Many studies have reported that nanomaterials could promote or inhibit the normal cell proliferation and differentiation. Therefore, the interaction between cells and nanomaterials in the scaffolds should be also studied.

The porous photothermal scaffolds were used to *in vitro* cancer cell ablation. However, the cell culture conditions *in vitro* are quite different from the *in vivo* environment. In order to further validate the photothermal effect of these scaffolds *in vivo* environment, the photothermal scaffolds can be implanted into the tumor site to evaluate their tumor resection ability *in vivo*. More importantly, after the tumor resection, the subsequent surrounding normal cell growth and tissue recover should be also checked.

Above all, prepare a good and suitable porous photothermal scaffold would provide a promising way for not only cancer therapy but also tissue engineering applications.

List of publications

1. Jing Zhang, Jingchao Li, Shangwu Chen, Naoki Kawazoe and Guoping Chen.
   Preparation of gelatin/Fe_3O_4 composite scaffolds for enhanced and repeatable cancer cell ablation.
   Journal of Material Chemistry B 2016, 4: 5664-5672.

2. Jing Zhang, Jingchao Li, Naoki Kawazoe and Guoping Chen.
   Composite scaffolds of gelatin and gold nanoparticles with tunable size and shape for photothermal cancer therapy.
   Journal of Material Chemistry B 2016, DOI: 10.1039/c6tb02872a

3. Jing Zhang, Jingchao Li, Xiuhui Wang, Naoki Kawazoe and Guoping Chen.
   Multifunctional gelatin/Fe_3O_4 scaffolds for cancer cell capture and ablation.
   Submitted

.

Acknowledgements

I would like to express my great and sincere gratitude to my supervisor, Professor Guoping Chen for his continuous support, patience and understanding on my research. Throughout my entire PhD study, Professor Chen has devoted to instructing my research from selecting research topics, offering guidance on my experiments, and helping me figure out from experimental problems, to giving suggestions and instructions on writing research papers and thesis. He taught me not only how to do the research, but also how to think as a researcher. I really appreciate the aspiring guidance, invaluably constructive criticism and insightful advice from Prof. Chen, which deeply impresses me, encourages me and lets me learn so much during my study. It is my great honor and pleasure to be able to join and work in Professor Chen's group.

I would also like to give my thanks to Dr. Naoki Kawazoe for his warm support and encouragement on my work in NIMS. His positive attitude, modest character professional skill, and thoughtful consideration have impressed me deeply. I am very grateful to work with him and to learn from him.

I would also like to acknowledge my thesis committee, Professor Hee Young Kim, Professor Tetsushi Taguchi, and Professor Mitsuhiro Ebara, for their valuable comments, kind help and constructive suggestions on my PhD defense and this thesis

I would like to give my sincere thanks to current and former members in our group. They are Dr. Tomoko Nakamoto, Dr. Jia'En Jasmine Li, Dr. Lingfeng Guo, Dr. Jianmin Yang, Dr. Hongli Mao, Dr. Himansu Nandasekhar, Dr. Rong Cai, Dr. Shangwu Chen, Dr. Xinlong Wang, Mr. Jingchao Li, Ms. Xiaohong Hu, Mr. Xiaomeng Li, Ms. Ying Chen, Mr. Yingjun Yang, Ms. Xiuhui Wang, Ms. Jia Hui NG and Ms. Nur Rofiqoh. Thank you for your cooperation and assistance in my experiments and daily life. I am thankful to Mrs. Tateno and Mrs. Hidaka for their great efforts and help since I came to Japan.

I wish to thank my parents and my friend for their support and understanding in my life. Without these, I would not have finished this thesis.

This work was conducted at International Center for Materials Nanoarchitectonics (MANA), National Institute for Materials Science and Graduate School of Pure and Applied Science of University of Tsukuba. I acknowledge the financial support from NIMS (Junior Research Assistantship).